Fall 2014

Image analysis using visual saliency with applications in hazmat sign detection and recognition

Bin Zhao
Purdue University

Graduate School ETD Form 9
(Revised 12/07)

PURDUE UNIVERSITY
GRADUATE SCHOOL
Thesis/Dissertation Acceptance

This is to certify that the thesis/dissertation prepared

By Bin Zhao

Entitled
Image Analysis Using Visual Saliency with Applications in Hazmat Sign Detection and Recognition

For the degree of Doctor of Philosophy

Is approved by the final examining committee:

EDWARD J. DELP
Chair

ARIF GHAFOOR

CHIH-CHUN WANG

JAN P. ALLEBACH

To the best of my knowledge and as understood by the student in the *Research Integrity and Copyright Disclaimer (Graduate School Form 20)*, this thesis/dissertation adheres to the provisions of Purdue University's "Policy on Integrity in Research" and the use of copyrighted material.

Approved by Major Professor(s): EDWARD J. DELP

Approved by: V. Balakrishnan 10-15-2014
Head of the Graduate Program Date

IMAGE ANALYSIS USING VISUAL SALIENCY WITH APPLICATIONS IN HAZMAT SIGN DETECTION AND RECOGNITION

A Dissertation

Submitted to the Faculty

of

Purdue University

by

Bin Zhao

In Partial Fulfillment of the

Requirements for the Degree

of

Doctor of Philosophy

December 2014

Purdue University

West Lafayette, Indiana

To my parents and my grandparents,
for their endless love, support, and encouragement

ACKNOWLEDGMENTS

I would not have been the person I am today without the support and guidance of my advisor, Professor Edward J. Delp. This dissertation would not have been possible without the encouragement and insights from my advisor. I especially thank him for teaching me how to learn, how to think, and how to collaborate. He has been my best mentor and what he has taught me all these years is the enduring treasure of my life.

I especially thank my advisory committee members: Professor Jan P. Allebach, Professor Arif Ghafoor, and Professor Chih-Chun Wang for their inspired teaching, support, and encouragement.

I want to thank Dr. Albert Parra, Joonsoo Kim, and He Li for their great collaboration and contribution to the Mobile Emergency Response GuidE (MERGE) project, for providing constructive feedback to my research and for always being willing to support my work.

I want to extend my thanks to all my former and current colleagues in the Video and Image Processing Laboratory (VIPER). I thank all my brilliant colleagues: Dr. Aravind Mikkilineni, Dr. Kevin Lorenz, Dr. Nitin Khanna, Dr. Satyam Srivastava, Dr. Ka Ki Ng, Dr. Fengqing Maggie Zhu, Dr. Marc Bosch Ruiz, Dr. Meilin Yang, Dr. Ye He, Dr. Chang Xu, Dr. Albert Parra, Ziad Ahmad, Jeehyun Choe, Neeraj Gadgil, Deen King-Smith, Joonsoo Kim, Soonam Lee, He Li, Khalid Tahboub, and Yu Wang. I also thank the visiting students in the VIPER lab: Blanca Delgado, Javi Ribera, Thitiporn Pramoun and Kharittha Thongkor. I thank all my friends in the VIPER lab for all the help they have given and all the joy they have brought.

I want to deeply appreciate my parents and my grandparents for their endless love, support, and encouragement. They have given me more than I could imagine in my life.

I gratefully thank the School of Electrical and Computer Engineering of Purdue University for accepting me into the Doctoral program and providing such a memorable environment to do research.

The hazardous material sign images shown in this thesis were partially obtained in cooperation with the officers in the U.S. Transportation Security Administration (TSA). I gratefully acknowledge their cooperation in the Mobile Emergency Response GuidE (MERGE) project.

This dissertation was supported by the Visual Analytics for Command, Control, and Interoperability Environments (VACCINE) Center of the U.S. Department of Homeland Security (DHS) under Award Number 2009-ST-061-CI000. I gratefully thank the VACCINE Center for the sponsorship of the MERGE research project in this dissertation.

TABLE OF CONTENTS

Page

Page

LIST OF TABLES

Table Page

LIST OF FIGURES

Figure Page

ABSTRACT

Zhao, Bin Ph.D., Purdue University, December 2014. Image Analysis Using Visual Saliency with Applications in Hazmat Sign Detection and Recognition. Major Professor: Edward J. Delp.

Visual saliency is the perceptual process that makes attractive objects “stand out” from their surroundings in the low-level human visual system. Visual saliency has been modeled as a preprocessing step of the human visual system for selecting the important visual information from a scene. We investigate bottom-up visual saliency using spectral analysis approaches. We present separate and composite model families that generalize existing frequency domain visual saliency models. We propose several frequency domain visual saliency models to generate saliency maps using new spectrum processing methods and an entropy-based saliency map selection approach. A group of saliency map candidates are then obtained by inverse transform. A final saliency map is selected among the candidates by minimizing the entropy of the saliency map candidates. The proposed models based on the separate and composite model families are also extended to various color spaces. We develop an evaluation tool for benchmarking visual saliency models. Experimental results show that the proposed models are more accurate and efficient than most state-of-the-art visual saliency models in predicting eye fixation.

We use the above visual saliency models to detect the location of hazardous material (hazmat) signs in complex scenes. We develop a hazmat sign location detection and content recognition system using visual saliency. Saliency maps are employed to extract salient regions that are likely to contain hazmat sign candidates and then use a Fourier descriptor based contour matching method to locate the border of hazmat signs in these regions. This visual saliency based approach is able to increase the accuracy of sign location detection, reduce the number of false positive objects, and speed up the overall image analysis process. We also propose a color recognition method to interpret the color inside the detected hazmat sign. Experimental results show that our proposed hazmat sign location detection method is capable of detecting and recognizing projective distorted, blurred, and shaded hazmat signs at various distances.

In other work we investigate error concealment for scalable video coding (SVC). When video compressed with SVC is transmitted over loss-prone networks, the decompressed video can suffer severe visual degradation across multiple frames. In order to enhance the visual quality, we propose an inter-layer error concealment method using motion vector averaging and slice interleaving to deal with burst packet losses and error propagation. Experimental results show that the proposed error concealment methods outperform two existing methods.

1. INTRODUCTION

1.1 Problem Statement

One of the objectives of public safety is to prevent and protect against events that can jeopardize the safety and well being of the community. Hazardous materials can cause harm to humans and the environment if there is exposure to the materials due to an accident or spill. In these cases first responders need procedures for handling hazardous materials and documenting evidence of hazardous materials accidents. The Emergency Response Guidebook (ERG), published by the U.S. Department of Transportation (DOT) [1], contains information as to what equipment, procedures and precautions should be used in handling hazardous materials. As one might expect, the guidebook is large and requires time to search an index to determine the best way to handle a particular hazardous material. The goal of this dissertation is to develop an mobile-based hazardous sign detection and recognition system using computer vision and image analysis methods, capable of providing accurate and useful guide information to the first responders in short time.

1.2 Visual Saliency

The human visual system (HVS) can rapidly process an enormous amount of visual information, such as color, orientation, and edge [2]. With the help of visual selection mechanisms in low-level HVS to reduce visual data, processing the large amount of visual data in real-time is a relatively easy task for human, but an extremely difficult task for computer. High-level cognitive and complex visual information processes, like scene understanding and object recognition, rely on the visual data that has been selected and transformed [3]. The notable Feature Integration Theory (FIT) describes visual attention as having two phases [4]. In the pre-attentive phase, the early vision system can rapidly process an enormous amount of low-level visual features in parallel, such as color, motion and edges [4]. Distinctive features (*e.g.*, luminous color, high velocity motion) will "stand out" automatically in the pre-attentive stage and then the salient regions draw more attention. In the next phase, the visual cortex performs more complex operations, such as object detection, tracking, recognition [5, 6].

There are close relations but also clear distinctions between visual attention and visual saliency. Visual attention has been a broad concept covering many topics, for instance, bottom-up/top-down, spatial/spatial-temporal, and overt/covert visual attention [7–10]. Visual saliency is generally referring to bottom-up processes in visual attention that select certain image regions more conspicuous, such as image regions having different features from their surroundings. Bottom-up attention has been mainly investigated in eye movement or fixation prediction on free-viewing of images or videos and in stimuli-driven search tasks, like finding an odd object popping out from their surroundings [9, 10]. Top-down attention deals with finding image regions more relevant to high-level cognitive factors, like demands, expectations, and current task. It has been studied in natural behaviors such as driving, shooting, and interactive game playing [9, 10]. Bottom-up visual attention is mainly based on the characteristics of visual stimuli, while top-down visual attention is determined by cognitive phenomena such as knowledge, demands, rewards, expectations, and goals [4]. Bottom-up visual attention is stimuli-driven, fast, and involuntary. Top-down visual attention is task-driven, slow, and voluntary. Therefore computational visual attention models often focus either on bottom-up or on top-down processes of visual attention [9, 10]. In general, bottom-up visual attention is defined as visual saliency and we use this definition in our work.

1.3 Hazmat Sign Detection and Recognition

A federal law in the U.S. requires vehicles transporting hazardous materials must carry a standard sign (i.e., hazmat sign) identifying the type of hazardous substance in the event of an emergency [11]. Typical hazmat signs are shown in Figure 1.1. Hazmat signs have identifying information described by the sign shape, color, symbols, and numbers. In the event of an emergency, first responders have to browse the Emergency Response Guidebook (ERG) to identify the material and determine what equipment, procedures and precautions should be used in handling hazardous materials. This process is slow and difficult for these who are not familiar with the guidebook.

There exist several mobile applications that provide access to this guidebook for first responders in the field. For example, the official ERG 2012 mobile application lets a user browse the ERG guidebook by United Nations (UN) identifier numbers, template images, and guide pages [1]. The WISER (Wireless Information System for Emergency Responders) mobile application lets a user browse the ERG guidebook by known substance types and hazard classifications [12]. However, these mobile applications only provide ways of manually searching the guidebook. We have developed a mobile-based system that makes use of image analysis methods to automatically detect and recognize the hazmat sign in an image and quickly provide guide information to users. We call this hazmat sign image analysis system MERGE (Mobile Emergency Response GuidE) [13]. The MERGE mobile application is capable of detecting hazmat signs from an image acquired using the mobile device and querying an internal database to provide accurate and useful information to first responders in real time [14, 15]. MERGE also provides a complete easily searchable version of the Emergency Response Guidebook (ERG) [1] by UN identifier numbers, template images, symbols, and classes.

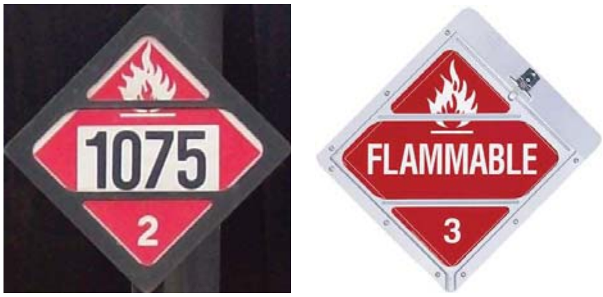

(a) An example of a hazmat sign used for a train tank car.

(b) An Example of a hazmat sign used for a truck trailer.

Fig. 1.1. Example of hazmat signs.

1.4 Error Concealment for Scalable Video Coding

With the rapid advancement of video coding, communication and networking technologies, video transfer over the Internet has been widely used for a broad range of social activities and applications. Users consume video via many types of terminals, for example, HDTVs, laptops and smart phones. Scalable video coding (SVC) [16] has been developed to deal with this heterogeneity in terminal types. An SVC encoder can generate scalable bitstreams in terms of spatial, temporal and quality scalability. The desired spatial resolution can then be extracted from the scalable bitstreams at an SVC decoder. SVC video is usually encoded in a base layer and one or more enhancement layers. Typically, the SVC decoder requires that the base layer frames be delivered almost error-free and uses them to decode the enhancement layer frames.

Due to the nature of dynamic and lossy channels used for video delivery (particularly wireless channels), video bitstreams transmitted over packet networks usually experience isolated and burst packet losses [17]. Moreover, once errors occur in video bitstreams, they are prone to propagate from one frame to another due to motion-compensated prediction used in SVC codec. These effects can result in severe visual quality degradation of the decoded frames. Error concealment (EC) is an effective scheme for error recovery. It reconstruct damaged regions can be ed from the correctly received neighboring regions. Due to the layered structure of SVC, one can exploit the spatial and temporal correlations of video frames between different layers to improve the performance of single layer error concealment [18].

1.5 Contributions of This Thesis

In this thesis we describe several visual saliency models in the frequency domain in Chapter 2, a hazmat sign image analysis system (MERGE) using visual saliency for location detection and content recognition in Chapter 3, and several error concealment methods for scalable video coding (SVC) in chapter 4.

For visual saliency models in the frequency domain, we develop separate and composite visual saliency model families for frequency domain visual saliency models. We propose six visual saliency models based on new spectrum processing methods and an entropy-based saliency map selection approach. We propose an entropy-based saliency map selection approach to select a “good” final saliency map among the set of map candidates. A group of extended saliency models that extends each proposed visual saliency models are also developed by incorporating both separate and composite model families and using variant color spaces. Experimental results show that the six best extended models are more accurate and efficient than most state-of-the-art models in predicting eye fixation on standard image datasets.

For hazmat sign image analysis system (MERGE), we develop hazmat sign location detection and content recognition methods based on visual saliency. We use the one of our proposed frequency domain models to extract salient regions that are likely to contain hazmat sign candidates and then use a Fourier descriptor based contour matching method to locate the border of hazmat signs in these regions. This visual saliency based approach is able to increase the accuracy of sign location detection, significantly reduce the number of false positives, and speed up the image analysis process. This approach improves the accuracy of existing methods presented in [14, 15]. We also propose a color recognition method to interpret the color inside the detected hazmat signs. Our three image datasets consists of images taken in the working field and outdoor field under variant lighting and weather conditions, distances, and perspectives.

For error concealment for scalable video coding (SVC), we develop two error concealment approaches robust to burst packet losses, i.e. inter-layer motion vector averaging and slice interleaving using optimum ordering. A two-layer spatial-temporal scalable video coding system are decribed to evaluate the existing and proposed error concealment methods. Experimental results confirmed that the proposed error concealment methods outperform two existing methods in reducing the impact of burst packet losses and error propagation.

The main contributions of visual saliency models in the frequency domain are:

- We investigate bottom-up visual saliency using spectral analysis approaches.
- We develop separate and composite visual saliency model families for frequency domain models.
- We propose six visual saliency models based on different spectrum processing.
- We propose an entropy-based saliency map selection approach.
- We develop an evaluation tool for benchmarking visual saliency models.

The main contributions of image analysis system for hazmat sign detection and recognition are:

- We develop a hazmat sign location detection and content recognition system using visual saliency.
- We used one of our proposed frequency domain models to extract salient regions.
- We developed a Fourier descriptor based contour matching method to locate the border of hazmat signs.

- We proposed a color recognition method to interpret the color inside the detected hazmat signs.
- We collected three hazmat sign image datasets.

The main contributions of error concealment methods for SVC are:

- We investigated the impact of burst packet loss and error propagation in base and enhancement layers.
- We explored inter-layer spatial and temporal correlations for error concealment against burst packet loss.
- We proposed two error concealment methods to enhance error recovery and visual quality:
- (1) Inter-layer motion vector averaging
- (2) Slice interleaving using optimum ordering
- We developed a two-layer spatial-temporal scalable video coding system for evaluation.

1.6 Publications Resulting from This Thesis

Conference Papers

1. **Bin Zhao** and Edward J. Delp, "Visual Saliency Models Based on Spectrum Processing," *Proceedings of the IEEE Winter Conference on Applications of Computer Vision*, Waikoloa Beach, HI, USA, January 2015. (Accepted)
2. **Bin Zhao**, Albert Parra, and Edward J. Delp, "Mobile-Based Hazmat Sign Detection and Recognition," *Proceedings of the IEEE Global Conference on Signal and Information Processing*, no. 6736996, pp. 735-738, Austin, TX, USA, December 2013. (Invited Paper)

3. **Bin Zhao** and Edward J. Delp, "Inter-layer Error Concealment for Scalable Video Coding," *Proceedings of the IEEE International Conference on Multimedia and Expo*, no. 6607539, pp. 1-6, San Jose, CA, USA, July 2013.

4. **Bin Zhao**, "Interleaving-Based Error Concealment for Scalable Video Coding System," *Proceedings of the IEEE Visual Communications and Image Processing Conference*, no. 6115965, pp. 1-4, Tainan City, Taiwan, November 2011.

5. Albert Parra, **Bin Zhao**, Joonsoo Kim, and Edward J. Delp, "Recognition, Segmentation and Retrieval of Gang Graffiti Images on a Mobile Device," *Proceedings of the IEEE International Conference on Technologies for Homeland Security*, no. 6698996, pp. 178-183, Waltham, MA, USA, November 2013.

6. Albert Parra, **Bin Zhao**, Andrew Haddad, Mireille Boutin, and Edward J. Delp, "Hazardous Material Sign Detection and Recognition," *Proceedings of the IEEE International Conference on Image Processing*, no. 6738544, pp. 2640-2644, Melbourne, Australia, September 2013.

Journal Papers

1. **Bin Zhao** and Edward J. Delp, "Biologically-Inspired Visual Saliency Models Using Spectrum Processing," in preparation.

2. **Bin Zhao**, Albert Parra, and Edward J. Delp, "Hazmat Sign Detection and Recognition Using Visual Saliency," in preparation.

2. VISUAL SALIENCY MODELS IN THE FREQUENCY DOMAIN

2.1 Visual Saliency

Visual saliency is the perceptual process that makes attractive objects “stand out” from their surroundings in the low-level human visual system. Visual saliency has been modeled as a preprocessing step of the human visual system for selecting the important visual information from a scene [3]. It is often referred to as bottom-up, low-level, stimulus-driven visual information processing. A master map of the “salient objects” [4] or a saliency map [3] is generated by the early vision system to indicate the locations of salient regions in a scene. High-level, cognitive and more complex visual information interpretation are mostly focused on the selected salient regions [3]. Visual saliency has been investigated in multiple fields including cognitive psychology, neuroscience, computer vision, and image/video processing [7–10]. We limit ourselves to focus on computational visual saliency models that are capable of computing saliency maps from input image or video. Visual saliency models are used in many applications including image and video compression [19, 20], content-aware image resizing [21], object extraction [22], object recognition [23], and traffic sign analysis [24].

Many visual saliency models have been proposed to emulate how the human visual system perceives and processes visual information [7–10]. For example, a notable Saliency-Based Visual Attention (SBVA) model is proposed in [25] using intensity, color and orientation features with a subsampled Gaussian pyramid. In [26] a Graph-Based Visual Saliency (GBVS) method forms the activation map from each feature map based on graph theory. A model of Attention based on Information Maximization (AIM) is presented in [27] using Independent Component Analysis (ICA) based feature extraction, joint likelihood, and self-information. A Dynamic Visual Attention (DVA) model based on the rarity of features is proposed in [28], which employs Incremental Coding Length (ICL) to measure the perspective entropy gain of each feature. A Frequency-Tuned Saliency Detection (FTSD) approach is introduced by [29] using low-level features of color and luminance. Two similar saliency models are developed using the Phase spectrum of the Fourier Transform (PFT) [30] and the Quaternion Fourier Transform (PQFT) [31] respectively to predict salient regions in the spatio-temporal domain. Two biologically plausible visual saliency approaches, frequency domain divisive normalization (FDN) and piecewise FDN (PFDN) methods, are proposed in [32], where PFDN has better performance and provides better biological plausibility. In [33] an Discrete Cosine Transform (DCT) based Image Signature (IS) method generates a saliency map using the inverse DCT of the signs in the cosine spectrum for image figure-ground separation. A quaternion DCT (QDCT) based image signature approach is developed by [34] using signum function and the inverse QDCT to compute a visual saliency map. A saliency detector based on the Scale-Space Analysis (SSA) of hypercomplex Fourier transform spectrum is presented in [35] using the convolution of the image amplitude spectrum with low-pass Gaussian kernels.

The focus of this chapter is to investigate low-complexity bottom-up visual saliency models in the frequency domain. The phase and amplitude spectrums of an image has been utilized for frequency domain saliency models. Most existing models keep the original phase spectrum and only modify the amplitude spectrum to generate saliency maps. We propose six visual saliency models based on new spectrum processing methods and an entropy-based saliency map selection approach. Six frequency domain saliency models are proposed using six new frequency spectrum processing methods, *i.e.* Gamma Corrected Spectrum (GCS) model, Gamma Corrected Log Spectrum (GCLS) model, Low-Pass Filtered Spectrum (LPFS) model, Low-Pass Filtered Log Spectrum (LPFLS) model, Gaussian Filtered Spectrum (GFS) model, and Gaussian Filtered Log Spectrum (GFLS) model. A set of saliency map candidates are generated by inverse transform using a set of modified amplitude spectrums and the original phase spectrum. An entropy-based approach is proposed to select a "good" final saliency map by minimizing the entropy among the set of saliency map candidates. A group of extended saliency models that extends each proposed visual saliency models are also developed by incorporating both separate and composite model families and using variant color spaces. The state-of-the-art frequency domain saliency models are capable of providing accurate prediction of human eye fixation/tracking data on the eye fixation image datasets. We did a comprehensive evaluation of the six best extended saliency models (GCS-FT-Lab, GCLS-FT-Lab, LPFS-FT-Lab, LPFLS-HFT-IRGBY, GFS-FT-Lab, and GFLS-HFT-IRGBY) by comparing with 10 state-of-the-art saliency models using two standard image datasets. Based on our analysis on the comparison results and the eye fixation distribution of the datasets, we are able to explain why the performance of some visual saliency models vary over different standard image datasets.

2.2 Visual Saliency Model Families

We investigate bottom-up visual saliency using spectral analysis approaches and generalize existing visual saliency models in the frequency domain shown in Figure 2.1. The existing visual saliency models in the frequency domain described above fall into two categories: (1) Some frequency domain models generate the final saliency map using separate color channel images. They use the spectrum of each color channel image individually and then fuse the individual saliency maps into the final map (*e.g.* [30,33]). (2) The other frequency domain models determine salient regions using a composite image representation. They usually merge color channel images into a quaternion image and then use the Hypercomplex Fourier Transform (HFT) [36, 37] to obtain the quaternion spectrum (*e.g.* [31, 35]). Note that the ideas of separate and composite processes have been alternatively presented in existing frequency domain models and they are generalized and considered as different spatial domain and frequency domain operations in Figure 2.1. We then develop both separate and composite visual saliency model families to differentiate frequency domain models in Figure 2.2.

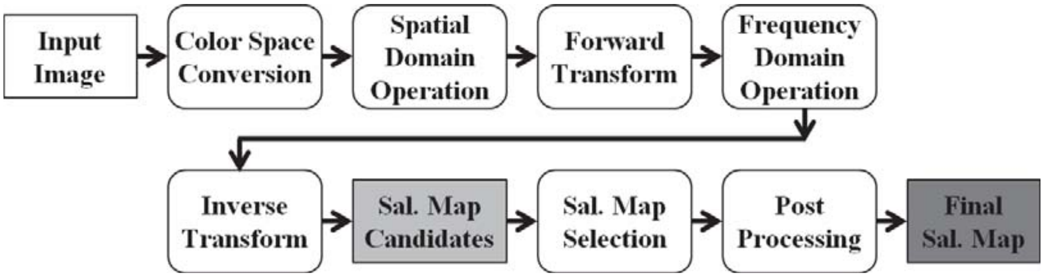

Fig. 2.1. The generalization of visual saliency models in the frequency domain.

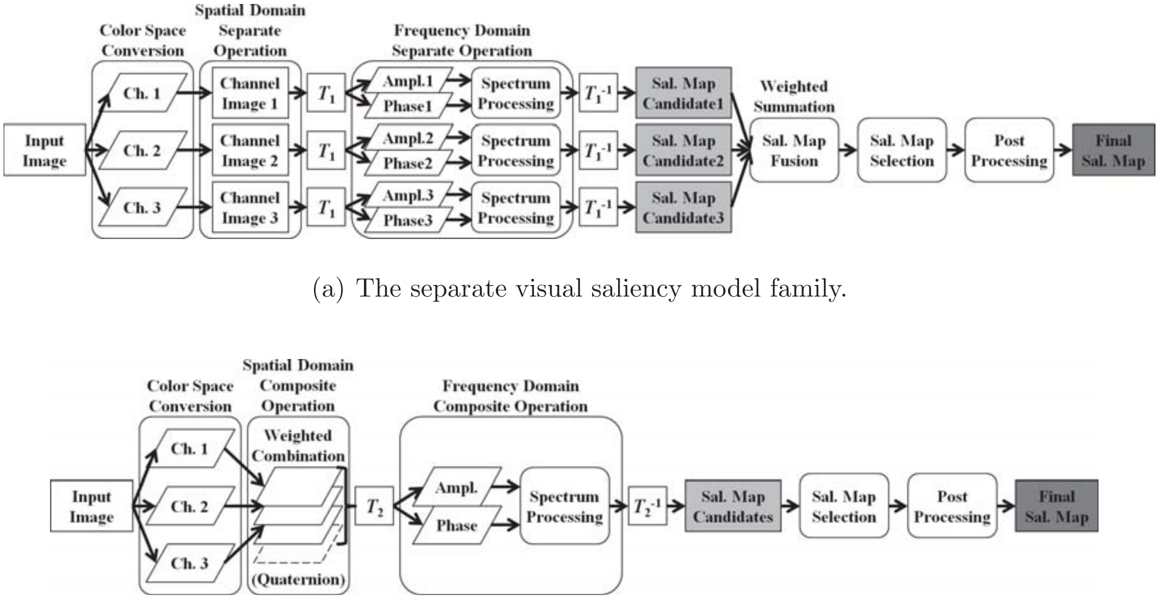

(a) The separate visual saliency model family.

(b) The composite visual saliency model family.

Fig. 2.2. Two visual saliency model families in the frequency domain.

2.2.1 Separate Visual Saliency Model Family

An image is first mapped into a specific color space and then each color channel image is separately transformed by T_1 into the frequency domain. The amplitude and phase spectrums of each color channel are independently processed. The modified amplitude and phase spectrums are separately inverse transformed by T_1^{-1} to generate a color channel saliency map. A fusion process is used to normalize and combine the color channel saliency maps into an intermediate saliency map. A weighted summation approach is often used (*e.g.,* average is used in [33]). $S(x, y) = \sum_{k=1}^{3} w_k S(x, y, k)$, where w_k is the weight for each channel saliency map $S(x, y, k)$. The final saliency map is generated after saliecy map selection and post-processing, such as border cut [38], blurring/smoothing [33], and center-bias setting [26]. Note that T_1 is a low-complexity transform, *e.g.* the Fourier Transform (FT) is used in [30] and the Discrete Cosine Transform (DCT) used in [33].

2.2.2 Composite Visual Saliency Model Family

An image is first mapped into a specific color space and then the color channel images are composed into a quaternion image. This is transformed by T_2 into the frequency domain, usually the Hypercomplex Fourier Transform (HFT) [36, 37] is utilized. The quaternion amplitude and phase spectrums in a hypercomplex axis are also independently processed. The modified quaternion amplitude and phase spectrums are inverse transformed by T_2^{-1} to form an intermediate saliency map. Similarly, the final saliency map is generated after saliency map selection and post-processing. Some existing saliency models are based on this composite model family as described in [31, 35, 39].

2.2.3 Connections Between Visual Saliency Model Families and Early Human Visual System

The two proposed visual saliency model families belong to "biologically plausible" models. The basic idea of biologically plausible models is to develop bottom-up visual saliency models by modeling some key components of the low-level human visual system. The three well-studied key components in the primary visual pathway of the human visual system are the Retina in the eye, the Lateral Geniculate Nucleus (LGN) and the Primary Visual Cortex (V1) [7]. The retina can be considered as a feature collector in the eyes. Visual signals collected by the retina are received by the LGN and transmitted to the V1 cortex. The V1 cortex is the first visual information processing module at low level for facilitating high level analysis. V1 creates a general, pre-attentive saliency map [40], with the receptive field location of the most active V1 neuron responding to a region of scene most likely to be selected [41]. Figure 2.3(a) and Figure 2.3(b) illustrate the primary visual pathway of the human visual system and the three key components.

Because the retina, LGN, and V1 cortex are the key components in the primary visual pathway, we focus on them to present an analogy between the visual saliency model families and the early human visual system. Cones and rods are two types of photoreceptors (specialized retinal neurons capable of phototransduction) turning the light into signals in the retina. Cones are located in the central part of the retina, called fovea, and rods are in the surrounding area of the fovea [42]. Cones are responsible for color vision at high light levels and high spatial acuteness. Rods are used for achromatic vision at very low light levels and low spatial acuteness. There are three types of cones in the retina related to perception of colors. They are conventionally labeled according to the wavelengths of the peaks of their spectral sensitivities: short-wavelength cone (S-cone), middle-wavelength cone (M-cone), and long-wavelength cone (L-cone) [43]. Based on the related work [44, 45], a pioneering work [46, 47] first introduce a combination of the Fourier (amplitude) transform and then log polar mapping for modeling the primary visual information processing in the V1 cortex area. It has been demonstrated that the primary visual information from the retina and the LGN is processed and analyzed in the V1 cortex by orientation and frequency bands in the Fourier plane [48].

The color space conversions in the proposed model families correspond to modeling the three types of cones' color functionalities in the retina. LGN is considered as an component that transmits visual signals from the retina to the V1 cortex. The spatial domain operations in the proposed model families correspond to modeling the rearrangement and transmission three-channel visual signals in LGN. It needs further research on the LGN for such spatial domain operations to determine if it use the separate or composite representation. The transform and spectrum processing in the frequency domain of the proposed model families correspond to modeling the primary visual information processing in the V1 cortex. Biologically plausible choices of the building blocks of the two model families still await further investigation and evidence. Inspired by the facts that a logarithm (log) conversion of contrast data is used in [44] and the log polar mapping is presented in [46, 49, 50], we will develop our visual saliency models using both original spectrum and log spectrum in the two model families.

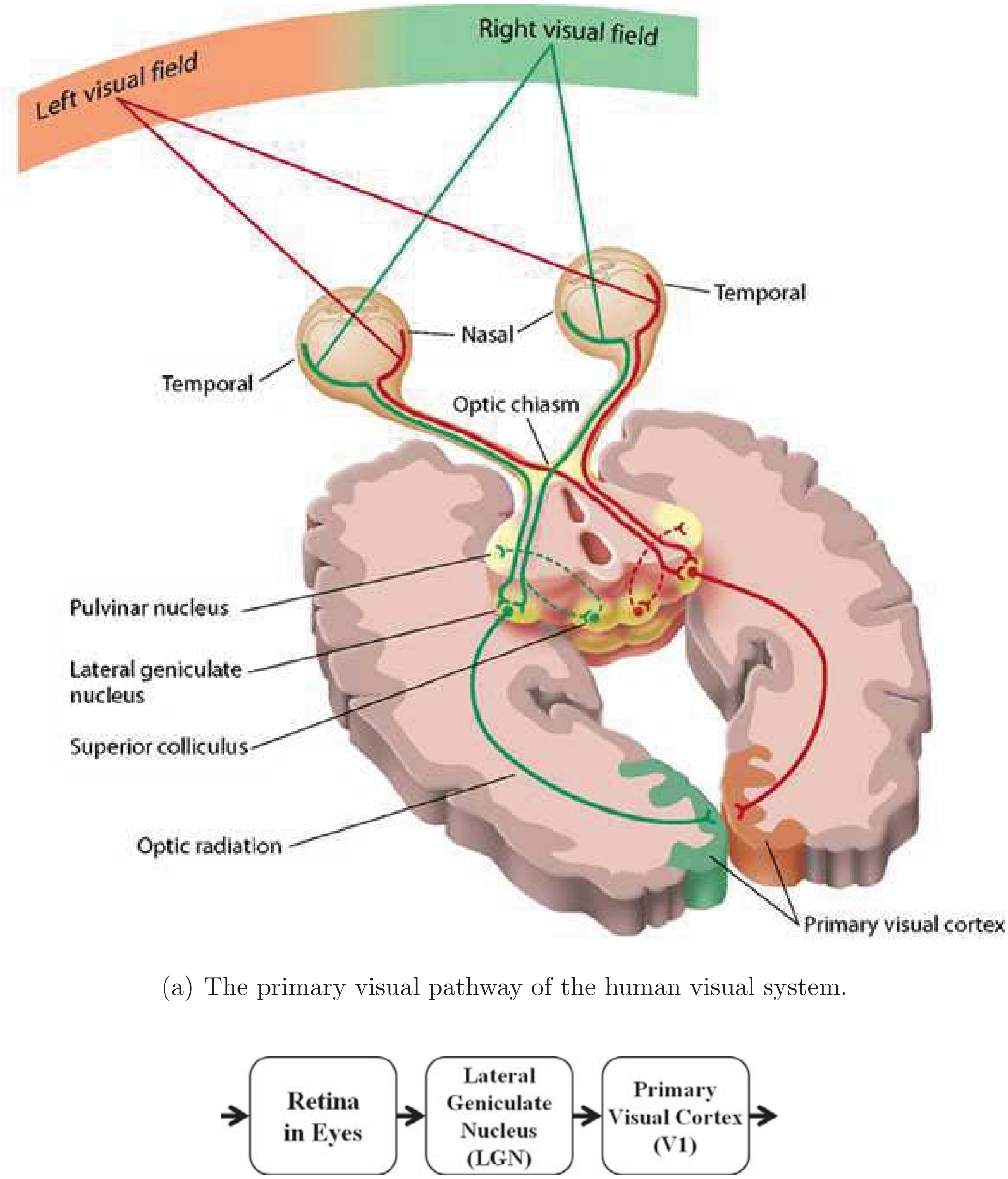

(a) The primary visual pathway of the human visual system.

(b) The Retina in the eye, the Lateral Geniculate Nucleus (LGN) and the Primary Visual Cortex (V1).

Fig. 2.3. The primary visual pathway of the human visual system and the three key components.

2.2.4 Color Spaces

Most visual saliency models are based on particular color spaces. A color space is a geometric representation of colors in a space, usually of three dimensions that refers to three color channels [51, 52]. The color space is spanned by a set of basis functions that are known as color matching functions. A color space is composed of all 3-channel representations of possible colors in the space.

The **RGB** color space is an additive color space based on three color primaries, *i.e.* red, green, and blue. Most people are familiar with the RGB color space. Computer monitors, digital cameras and scanners use RGB primaries. Many variants of the RGB color space have been proposed with some of them being adopted by international standard organizations [53]. These RGB color spaces are often used for image/video capture, representation, and display.

The **Lab** ($CIE\ L^*a^*b^*$) color space is used because it respectably represents human perceptual uniformity for color difference measurements [52]. The Lab color space is used for model chromatic adaptation, model response compression, and useful color difference measurement. CIE stands for the International Commission on Illumination or in French, the Commission Internationale de l'Eclairage (CIE). The L^* component reflects human perception of lightness while the a^* and b^* components approximate the human chromatic opponent system.

$$L^* = 116f(\frac{Y}{Y_n}) - 16, \tag{2.1}$$

$$a^* = 500[f(\frac{X}{X_n}) - f(\frac{Y}{Y_n})], \tag{2.2}$$

$$b^* = 200[f(\frac{Y}{Y_n}) - f(\frac{Z}{Z_n})]. \tag{2.3}$$

$$f(t) = \begin{cases} t^{\frac{1}{3}}, & \text{if } t > (\frac{6}{29})^3, \\ \frac{1}{3}(\frac{29}{6})^2 t + \frac{4}{29}, & \text{if } t \leq (\frac{6}{29})^3, \end{cases} \tag{2.4}$$

$$f(t) = \begin{cases} t^{\frac{1}{3}}, & \text{if } t > (\frac{6}{29})^3, \\ \frac{1}{3}(\frac{29}{6})^2 t + \frac{4}{29}, & \text{if } t \leq (\frac{6}{29})^3, \end{cases} \tag{2.5}$$

where X_n, Y_n and Z_n are the tristimulus values of $CIE\ XYZ$ color space with a specific reference white point (the subscript n means normalized values). The $CIE\ XYZ$ color space includes almost all color sensations that an average person can experience and it serves as a standard reference defining many other color spaces [52].

The **IRGBY** opponent color space is also employed because there exists a color double-opponent system in human visual cortex for the red/green, green/red, blue/yellow, and yellow/blue color pairs [54]. The IRGBY opponent color space is defined as follows. Let r, g, and b denote the red, green, and blue color primaries, four color features are first generated as follows (negative values are set to zero).

$$\begin{aligned} Red : R &= r - \frac{g+b}{2}, && (2.6) \\ Green : G &= g - \frac{r+b}{2}, && (2.7) \\ Blue : B &= b - \frac{r+g}{2}, && (2.8) \\ Yellow : Y &= \frac{r+g}{2} - \frac{|r-g|}{2} - b. && (2.9) \end{aligned}$$

The intensity channel $\mathcal{I}$ is the average of the red, green, and blue color components in Equation (2.10), Red-Green channel $\mathcal{RG}$ are used to simultaneously account for red/green and green/red double opponency in Equation (2.11) and Blue-Yellow channel $\mathcal{BY}$ for blue/yellow and yellow/blue for double opponency in Equation (2.12).

$$\begin{aligned} \mathcal{I} &= \frac{r+g+b}{3}, && (2.10) \\ \mathcal{RG} &= R - G, && (2.11) \\ \mathcal{BY} &= B - Y. && (2.12) \end{aligned}$$

2.2.5 Quaternion Representation

Quaternion Definitions

Developed by William R. Hamilton [55], the quaternion represents a four-dimensional (4D) algebra $\mathbf{Q}$ over the real numbers $\mathbf{R}$ and are an extension of the two-dimensional (2D) complex numbers $\mathbf{C}$. A quaternion q is defined as $q = a + bi + cj + dk \in \mathbf{Q}$, where $a, b, c, d \in \mathbf{R}$, 1, i, j, and k denote the four basis, and $i^2 = j^2 = k^2 = ijk = -1$ $(ij = -ji = k, jk = -kj = i, ki = -ik = j)$. The addition (sum) of two quaternions q_1 and q_2 $(q_1, q_2 \in \mathbf{Q})$ is defined as follows:

$$\begin{aligned} q_1 + q_2 &= (a_1 + b_1 i + c_1 j + d_1 k) + (a_2 + b_2 i + c_2 j + d_2 k) \qquad (2.13) \\ &= (a_1 + a_2) + (b_1 + b_2)i + (c_1 + c_2)j + (d_1 + d_2)k. \qquad (2.14) \end{aligned}$$

The multiplication (product) of two quaternions q_1 and q_2 $(q_1, q_2 \in \mathbf{Q})$ is defined as follows:

$$\begin{aligned} q_1 q_2 &= (a_1 + b_1 i + c_1 j + d_1 k)(a_2 + b_2 i + c_2 j + d_2 k) \qquad (2.15) \\ &= a_1 a_2 - b_1 b_2 - c_1 c_2 - d_1 d_2 \\ &\quad +(a_1 b_2 + b_1 a_2 + c_1 d_2 - d_1 c_2)i \\ &\quad +(a_1 c_2 - b_1 d_2 + c_1 a_2 + d_1 b_2)j \\ &\quad +(a_1 d_2 + b_1 c_2 - c_1 b_2 + d_1 a_2)k. \qquad (2.16) \end{aligned}$$

Under addition and multiplication, quaternions have all the properties of a field, except multiplication (product) is not commutative. For example, by definition $ij = k$ while $ji = -k$. Therefore, we have to distinguish between left-sided and right-sided multiplications in the following (marked by L and R, respectively). A quaternion q is known as real if $q = a + 0i + 0j + 0k$ and pure imaginary if $q = 0 + bi + cj + dk$. We can define the operators $Re(q) = a$ and $Im(q) = bi + cj + dk$ that extract the real part and the imaginary part from a quaternion $q = a + bi + cj + dk$. As for complex numbers, we can define a conjugate quaternion $q^* = a - bi - cj - dk$ as well as the norm $|q| = \sqrt{qq^*}$.

Quaternion Image

Every image $\mathbf{f}(m,n,c) \in \mathbf{R}^{M \times N \times C}$ with at most four channels, *i.e.* $C \leq 4$, can be represented using a $M \times N$ quaternion matrix $f_{\mathrm{Q}}(m,n)$ in the conventional and symplectic forms [37].

$$\begin{aligned} f_{\mathrm{Q}}(m,n) &= f_4(m,n) + f_1(m,n)i + f_2(m,n)j + f_3(m,n)k & (2.17) \\ &= f_4(m,n) + f_1(m,n)i + (f_2(m,n)j + f_3(m,n)i)j, & (2.18) \end{aligned}$$

where $f_c(m,n)$ denotes the $M \times N$ matrix of the c-th image channel. It is common to represent the (potential) 4-th image channel as the scalar part $f_4(m,n)$, because when using this definition it is capable of working with pure quaternions ($f_4(m,n) = 0$) for the most common color spaces such as, *e.g.*, RGB and Lab.

Weighted Quaternion Image

The quaternion definition was extended to include weights of importance for feature channels [56] et The relative importance of the feature channels for the visual saliency can be modeled by introducing a weight vector of quaternion components $w = [w_1\ w_2\ w_3\ w_4]^T$ into Equation (2.17) and (2.18).

$$\begin{aligned} f_{\mathrm{Q}}(m,n) &= w_4 f_4(m,n) + w_1 f_1(m,n)i + w_2 f_2(m,n)j + w_3 f_3(m,n)k & (2.19) \\ &= w_4 f_4(m,n) + w_1 f_1(m,n)i + (w_2 f_2(m,n)j + w_3 f_3(m,n)i)j. & (2.20) \end{aligned}$$

When using unit weights for equal contribution of each feature channel, Equation (2.17) and (2.18) are special cases of Equation (2.19) and (2.20).

Hypercomplex Fourier Transform (HFT)

Following the definition of the Hypercomplex Fourier Transform (HFT) [36, 37], equivalently Quaternion Discrete Fourier Transform (QDFT), we can transform an

$M \times N$ quaternion spatial matrix $f_{\mathrm{Q}}(m,n)$ into a quaternion spectral matrix, either $F^{\mathrm{L}}_{\mathrm{Q}}(u,v)$ or $F^{\mathrm{R}}_{\mathrm{Q}}(u,v)$, due to the non-commutative multiplication rule of quaternions in Section 2.2.5. There exist two forms of **Forward Hypercomplex Fourier Transform (FHFT)** or **Forward Quaternion Discrete Fourier Transform (FQDFT)** using either left-sided multiplication or right-sided multiplication:

$$F^{\mathrm{L}}_{\mathrm{Q}}(u,v) = \frac{1}{\sqrt{MN}} \sum_{m=0}^{M-1} \sum_{n=0}^{N-1} exp\left(-\widehat{q}2\pi(\frac{mv}{M} + \frac{nu}{N})\right) f^{\mathrm{L}}_{\mathrm{Q}}(m,n), \tag{2.21}$$

$$F^{\mathrm{R}}_{\mathrm{Q}}(u,v) = \frac{1}{\sqrt{MN}} \sum_{m=0}^{M-1} \sum_{n=0}^{N-1} f^{\mathrm{R}}_{\mathrm{Q}}(m,n) exp\left(-\widehat{q}2\pi(\frac{mv}{M} + \frac{nu}{N})\right). \tag{2.22}$$

The corresponding **Inverse Hypercomplex Fourier Transform (IHFT)** or **Inverse Quaternion Discrete Fourier Transform (IQDFT)** is defined as follows:

$$f^{\mathrm{L}}_{\mathrm{Q}}(m,n) = \frac{1}{\sqrt{MN}} \sum_{u=0}^{N-1} \sum_{v=0}^{M-1} exp\left(\widehat{q}2\pi(\frac{mv}{M} + \frac{nu}{N})\right) F^{\mathrm{L}}_{\mathrm{Q}}(u,v), \tag{2.23}$$

$$f^{\mathrm{R}}_{\mathrm{Q}}(m,n) = \frac{1}{\sqrt{MN}} \sum_{u=0}^{N-1} \sum_{v=0}^{M-1} F^{\mathrm{R}}_{\mathrm{Q}}(u,v) exp\left(\widehat{q}2\pi(\frac{mv}{M} + \frac{nu}{N})\right). \tag{2.24}$$

Here, $\widehat{q}$ is a unit pure quaternion that serves as an axis of the transform space and determines a direction in a color space for color images [37]. The choice of $\widehat{q}$ is arbitrary, but it consequently can influence the results of quaternion-based transform. An obvious axis choice for color images is the direction corresponding to the luminance axis. For example, a good axis candidate would be the "gray line" in RGB color space and thus $\widehat{q} = (i + j + k)/\sqrt{3}$. In fact, this would decompose a color image into luminance and chrominance color components [57].

Quaternion Discrete Cosine Transform (QDCT)

Following the definition of the Quaternion Discrete Cosine Transform (QDCT) [34, 58], we can transform an $M \times N$ quaternion spatial matrix $f_{\mathrm{Q}}(m,n)$ into a quaternion spectral matrix, either $F_{\mathrm{Q}}^{\mathrm{L}}(u,v)$ or $F_{\mathrm{Q}}^{\mathrm{R}}(u,v)$, due to the non-commutative multiplication rule of quaternions in Section 2.2.5. There exist two forms of **Forward Quaternion Discrete Cosine Transform (FQDCT)** using either left-sided multiplication or right-sided multiplication:

$$F_{\mathrm{Q}}^{\mathrm{L}}(u,v) = \alpha_u^M \alpha_v^N \sum_{m=0}^{M-1}\sum_{n=0}^{N-1} \widehat{q} f_{\mathrm{Q}}(m,n) \cos\left(\frac{\pi(2m+1)u}{2M}\right)\cos\left(\frac{\pi(2n+1)v}{2N}\right), \quad (2.25)$$

$$F_{\mathrm{Q}}^{\mathrm{R}}(u,v) = \alpha_u^M \alpha_v^N \sum_{m=0}^{M-1}\sum_{n=0}^{N-1} f_{\mathrm{Q}}(m,n)\widehat{q} \cos\left(\frac{\pi(2m+1)u}{2M}\right)\cos\left(\frac{\pi(2n+1)v}{2N}\right), \quad (2.26)$$

$$\alpha_u^M = \begin{cases} \sqrt{\frac{1}{M}}, & \text{if } u = 0, \\ \sqrt{\frac{2}{M}}, & \text{if } u \neq 0, \end{cases} \quad (2.27)$$

$$\alpha_v^N = \begin{cases} \sqrt{\frac{1}{N}}, & \text{if } v = 0, \\ \sqrt{\frac{2}{N}}, & \text{if } v \neq 0. \end{cases} \quad (2.28)$$

According to FQDCT, there are also two forms of **Inverse Quaternion Discrete Cosine Transform (IQDCT)** as follows.

$$f_{\mathrm{Q}}^{\mathrm{L}}(m,n) = \sum_{u=0}^{M-1}\sum_{v=0}^{N-1} \alpha_u^M \alpha_v^N \widehat{q} F_{\mathrm{Q}}^{\mathrm{L}}(u,v) \cos\left(\frac{\pi(2v+1)u}{2M}\right)\cos\left(\frac{\pi(2n+1)m}{2N}\right), \quad (2.29)$$

$$f_{\mathrm{Q}}^{\mathrm{R}}(m,n) = \sum_{u=0}^{M-1}\sum_{v=0}^{N-1} \alpha_u^M \alpha_v^N F_{\mathrm{Q}}^{\mathrm{R}}(u,v)\widehat{q} \cos\left(\frac{\pi(2v+1)u}{2M}\right)\cos\left(\frac{\pi(2n+1)m}{2N}\right). \quad (2.30)$$

When comparing the QDCT and HFT (equivalently QDFT), the transform basis $\widehat{q}\cos\left(\frac{\pi(2m+1)u}{2M}\right)\cos\left(\frac{\pi(2n+1)v}{2N}\right)$ of QDCT is distinct from the one $exp\left(-\widehat{q}2\pi(\frac{mv}{M}+\frac{nu}{N})\right)$ of HFT because QDCT's basis is real-valued instead of HFT's is hypercomplex-valued. The factors α_u^M and α_v^N of QDCT are also different from the factor $\frac{1}{\sqrt{MN}}$ of HFT. However, both definitions share the concept of a unit pure quaternion $\widehat{q}$ that serves as a transformation axis [57].

2.3 Proposed Visual Saliency Models

2.3.1 Spectral Analysis Approaches

We investigate bottom-up visual saliency and develop new visual saliency models using spectral analysis approaches. Theoretically, the spatial variations of visual information in an image can be broken down to frequency components, each being characterized by an amplitude and a phase. The amplitude spectrum describes how much energy of each sinusoidal component is present in an image and the phase spectrum specifies where each of the sinusoidal components resides in the image [59]. Based on A. V. Oppenheim's early discovery [60, 61], the phase spectrum specifies important visual saliency information that indicates where the "proto-objects" or salient regions are located in the spatial domain [30,33]. Figure 2.4 demonstrates that phase spectrum contains important visual saliency information. A primary saliency map is obtained only by phase spectrum from frequency domain reconstruction. When the waveform is a positive or negative pulse function, this map contains the largest sharp spikes at the jump edges of the input pulse function. This is because a variety of sinusoidal components contribute the phase changes at the jump edges. In contrast, when the input is a periodic sinusoidal function of a fixed frequency, there is no significant spike in the middle of the map. Compared with the entire waveform, more distinct or less repeated segment contains more visual saliency information at the same location.

The amplitude spectrum also contains both saliency (distinct patterns) and non-saliency (repeated patterns) information. The sharp peaks or spikes in the amplitude spectrum correspond to non-saliency which should be suppressed for saliency detection [35]. Figure 2.5 demonstrates an example of amplitude spectrum contains both saliency and non-saliency information. The input signal (1st row) is a periodic sinusoidal function of a fixed frequency, but there is a short segment where another sinusoidal function of different frequency signal is replaced. The short segment is quite distinct from the entire signal, so a good saliency model should be able to de-

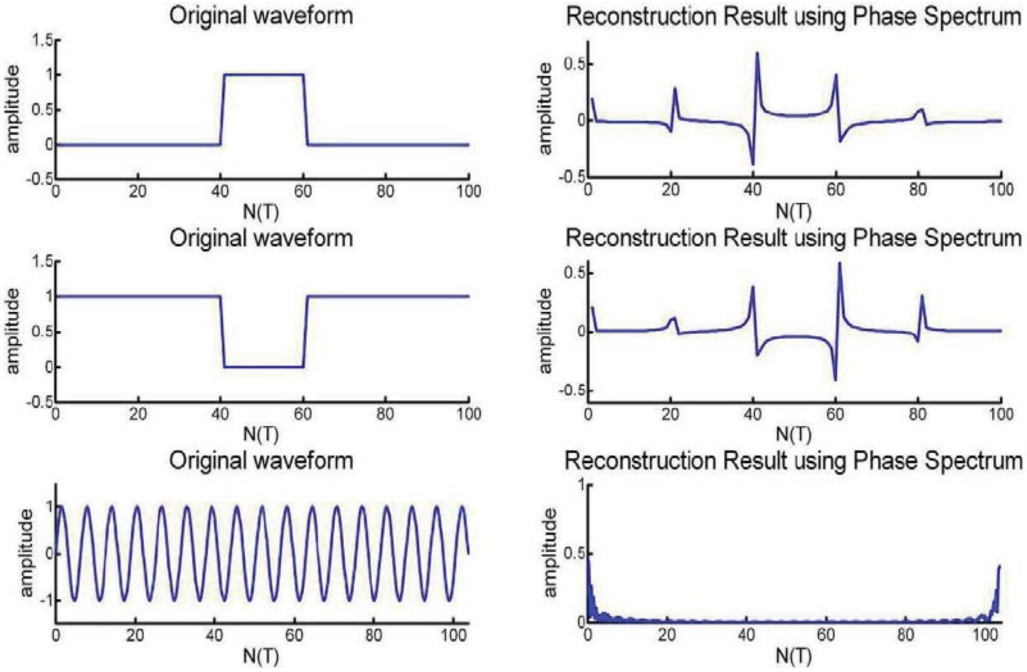

Fig. 2.4. Examples of phase spectrum contains important visual saliency information. Reproduced from [30]

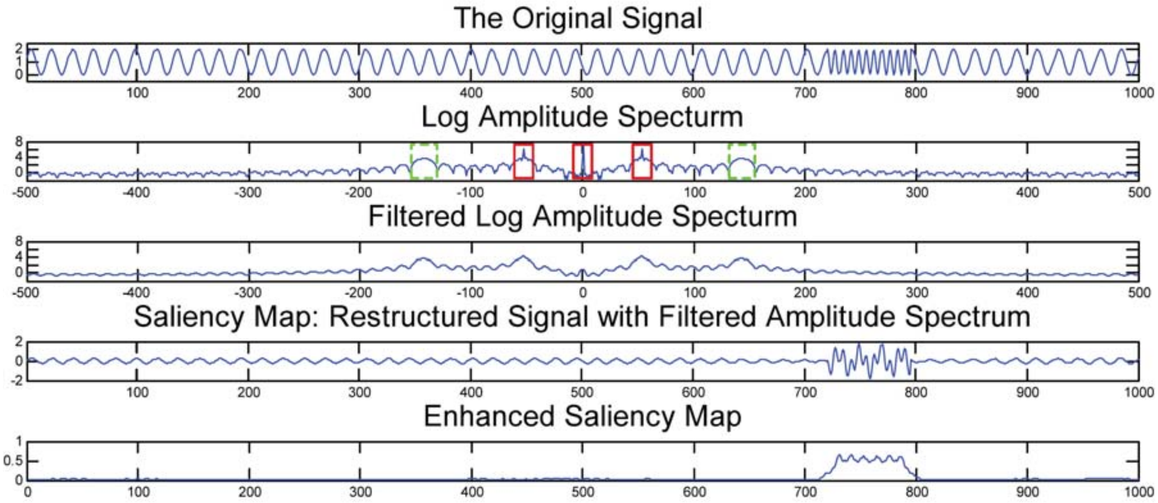

Fig. 2.5. An example of amplitude spectrum contains both saliency and non-saliency information. Reproduced from [35]

tect it. The amplitude spectrum of the above mixed sinusoidal signal is shown in the 2nd row. There are three very sharp spikes (labeled by solid boxes), one of which corresponds to the constant component (Direct Current (DC) component) at zero frequency and the other two spikes correspond to the repeated component (periodic component). In addition, there are two rounded maxima (labeled by dashed boxes) corresponding to the salient segment. The amplitude spectrum is then filtered by a Gaussian kernel (3rd row) and a primary saliency map of the mixed sinusoidal signal is generated by the filtered amplitude and original phase spectrum (4th row). Both the constant and the repeated components are largely suppressed while the salient segment is well preserved. The primary saliency map enhanced by post-processing is shown in the 5th row.

Therefore, most frequency domain visual saliency models perform certain processing on the amplitude spectrum but keep the phase spectrum unchanged to generate saliency maps. Given an image $f(x,y)$, it is transformed into the frequency domain to obtain its frequency spectrum $\mathcal{F}(u,v) = T[f(x,y)]$. The amplitude spectrum $\mathcal{A}(u,v) = |\mathcal{F}(u,v)|$ and the phase spectrum $\mathcal{P}(u,v) = angle(\mathcal{F}(u,v))$ are obtained, and if necessary the log amplitude spectrum is obtained: $\mathcal{L}(u,v) = log_e(\mathcal{A}(u,v)) = log_e(|\mathcal{F}(u,v)|)$. In our proposed models, the Fourier Transform (FT) [62] is used for the separate model family and the Hypercomplex Fourier Transform (HFT) [36,37] is employed for the composite model family. The inverse transform can be written as follows:

$$
\begin{aligned}
f(x,y) &= T^{-1}[\mathcal{F}(u,v)], && (2.31)\\
\Leftrightarrow f(x,y) &= T^{-1}[\mathcal{A}(u,v) \cdot exp(i \cdot \mathcal{P}(u,v))], && (2.32)\\
\Leftrightarrow f(x,y) &= T^{-1}[exp(\mathcal{L}(u,v) + i \cdot \mathcal{P}(u,v))]. && (2.33)
\end{aligned}
$$

2.3.2 Entropy-Based Saliency Map Selection

Entropy is a statistical measure of randomness. Entropy $\mathcal{H}_f$ is based on the distribution of the values of f. Let L be the number of gray levels of a grayscale image $f(x, y)$ of size $M \times N$. The priori probability $P_{f,g}$ is defined by the total number of occurrences $C_{f,g}$ (pixel counts in histogram) of the gray level g divided by the total number of pixels $M \times N$ of the grayscale image $f(x, y)$. When the histogram of the grayscale image $f(x, y)$ is given, the entropy $\mathcal{H}_f$ is determined as follows.

$$\mathcal{H}_f = -\sum_{g=1}^{L} P_{f,g} log_2(P_{f,g}), \tag{2.34}$$

$$P_{f,g} = \frac{C_{f,g}}{M \times N}. \tag{2.35}$$

The saliency map can be considered as a probability map whose values range from 0 to 1. In a typical saliency map, the higher salient regions would be assigned larger values and the rest of non-salient regions would be very small values. We observed that the closer values would be clustered in closer locations in a saliency map. In general, a saliency map is generated with low grades of fragment and randomness. According to the definition of entropy, we can use the entropy of generated saliency maps to select a “good” saliency map of the lowest fragment and randomness. The entropy of this saliency map would be relatively smaller than the one of other saliency maps, which could correspond to high efficient perceptive coding and low energy cost [63, 64].

Based on above analysis, we propose an entropy-based saliency map selection approach. An output saliency map $S'(x, y, k')$ is selected by minimizing the entropy $\mathcal{H}(S(x, y, k))$ among the group of saliency map candidates.

$$k' = \arg\min_{k}\{\mathcal{H}(S(x, y, k))\}, \tag{2.36}$$

$$\mathcal{H}(S) = -\sum_{g=1}^{L} P_{S,g} log_2(P_{S,g}), \tag{2.37}$$

$$P_{S,g} = \frac{C_{S,g}}{M \times N}, \tag{2.38}$$

where $\mathcal{H}(S(x, y, k))$ is the entropy of each saliency map candidate $S(x, y, k)$.

2.3.3 Post-Processing

To achieve a better visual illustration, the final saliency map is generated after some post-processing [10]. As introduced in [65], usually each element in the saliency map is squared individually and then the saliency map is saliency map is convoluted with a Gaussian burring kernel $b_{opt}(x, y)$ with an optimal sigma σ_{opt} determined by experiments.

$$S''(x, y, k') = b_{opt}(x, y) \star \|S'(x, y, k')\|^2, \tag{2.39}$$

where $b_{opt}(x, y)$ is a Gaussian burring kernel with optimal sigma σ_{opt}, $\star$ denotes the convolution operation and $\| \cdot \|^2$ denotes the square of each element individually.

$$b_{opt}(x, y) = \frac{1}{2\pi\sigma_{opt}^2} exp\left(\frac{-(x^2 + y^2)}{2\sigma_{opt}^2}\right). \tag{2.40}$$

We generate the kernel $b_{opt}(x, y)$ with the same size of the output saliency map by sampling continuous Gaussian distributed values into discrete Gaussian distributed values at the points of each pixel. The Gaussian values of this kernel are normalized again by dividing each element by the sum of all elements in the kernel. In order to further improve the output saliency map, other post-processing steps may be used, *e.g.* border cut [38] and center-bias setting [26].

2.3.4 Visual Saliency Model Using Gamma Corrected Spectrum (GCS)

Gamma correction is a nonlinear operation used to modify the luminance or tristimulus values in an image display system [66]. It is defined by two reversible power functions as follows.

$$
\begin{aligned}
V_{out} &= (V_{in})^{\gamma}, && (2.41)\\
V_{in} &= (V_{out})^{\frac{1}{\gamma}}, && (2.42)
\end{aligned}
$$

where V_{out} and V_{in} are the input and output values. Under common illumination conditions, the human visual systems follows an approximate power function, namely the psychophysical power law, developed by Stanley S. Stevens [67]. Gamma correction is used to compensate for the human visual system, in order to maximize the use of the bits or bandwidth according to how humans perceive light or color [66].

We propose a visual saliency model using Gamma Corrected Spectrum (GCS). A set of gamma corrections with different gamma values γ_k are utilized to modify the amplitude spectrum while keeping the phase spectrum unchanged. Saliency map candidates $S(x, y, k)$ can be constructed by the inverse transform of the gamma corrected amplitude spectrums $\mathcal{A}_{GCS}(u, v, k)$ with the original phase spectrum $\mathcal{P}(u, v)$.

$$
\begin{aligned}
\mathcal{A}_{GCS}(u, v, k) = (\mathcal{A}(u, v))^{\gamma_k}, && (2.43)\\
S(x, y, k) = T^{-1}[(\mathcal{A}(u, v))^{\gamma_k} \cdot exp(i \cdot \mathcal{P}(u, v))], && (2.44)\\
S(x, y, k) = T^{-1}[exp(\mathcal{L}(u, v) \cdot \gamma_k + i \cdot \mathcal{P}(u, v))], && (2.45)
\end{aligned}
$$

where k is an index $k = \{0, \ldots, K\}$ and $\gamma_k = \frac{k}{16}$. K is determined by the largest dimension of the size of the saliency map, $K = \lfloor log_4(max(H, W)) \rfloor + 1$, where W and H are the width and height of the saliency map. For example, if the size of the saliency map is 64×48, $K = 4$, $k = \{0, 1, 2, 3, 4\}$, and $\gamma_k = \{0, \frac{1}{16}, \frac{1}{8}, \frac{1}{4}, \frac{1}{2}\}$. An output saliency map $S'(x, y, k')$ is selected by minimizing the entropy $\mathcal{H}(S(x, y, k))$ among the set of candidates using the same Equation (2.36) and (2.37). The final GCS saliency map is generated by Equation (2.39).

2.3.5 Visual Saliency Model Using Gamma Corrected Log Spectrum (GCLS)

Following our Gamma Corrected Spectrum (GCS) model, we also develop a visual saliency model using the Gamma Corrected Log Spectrum (GCLS). A set of gamma corrections with different gamma values γ_k are used to modify the log amplitude spectrum while keeping the phase spectrum unchanged. For convenience, we only describe the main steps in the following equations.

$$\mathcal{L}_{GCLS}(u, v, k) = (\mathcal{L}(u, v))^{\gamma_k}, \tag{2.46}$$

$$S(x, y, k) = T^{-1}[exp((\mathcal{L}(u, v))^{\gamma_k} + i \cdot \mathcal{P}(u, v))], \tag{2.47}$$

We use the same parameter settings as the GCS model and an output saliency map $S'(x, y, k')$ is generated by the same selection approach as Equation (2.36). The final GCLS saliency map is obtained by Equation (2.39).

2.3.6 Visual Saliency Model Using Low-Pass Filtered Spectrum (LPFS)

The amplitude spectrum contains some information related to non-salient and salient regions. ¿From our spectral analysis, the sharp peaks or spikes in the amplitude spectrum are strongly related to repeated patterns (non-salient regions) while the other entities correspond to distinct patterns (salient regions). In order to discard non-salient regions and maintain the salient regions, a low-pass filter (LPF) can be used to suppress sharp peaks or spikes to generate saliency map. We design a low-pass filter $LPF(u, v, k)$ in the frequency domain based on the k-th root of a two-dimensional (2D) cosine function.

$$LPF(u, v, k) = \left(\frac{1}{4}(1 + cos(u))(1 + cos(v))\right)^{\frac{1}{k}}, \tag{2.48}$$

$$lpf(x, y, k) = \left(\frac{1}{16}(\delta(x-1) + 2\delta(x) + \delta(x+1))(\delta(y-1) + 2\delta(y) + \delta(y+1))\right)^{\frac{1}{k}} \tag{2.49}$$

where $(u, v) \in [-\pi, +\pi]$ and $\frac{1}{k}$ denotes the k-th root of the 2D cosine function. This low-pass filter with frequency response $LPF(e^{j0}, e^{j0}) = 1$, $LPF(e^{ju}, e^{\pm j\pi}) = 0$ and $LPF(e^{\pm j\pi}, e^{jv}) = 0$ in the frequency domain. Note that when $k = 1$, this LPF in the frequency domain corresponds to a 2D Finite Impulse Response (FIR) filter $lpf(x, y, 1)$ in the spatial domain.

$$LPF(u, v, 1) = \frac{1}{4}(1 + cos(u))(1 + cos(v)), \tag{2.50}$$

$$lpf(x, y, 1) = \frac{1}{16}\begin{bmatrix} 1 & 2 & 1 \\ 2 & \boxed{4} & 2 \\ 1 & 2 & 1 \end{bmatrix}. \tag{2.51}$$

This continuous low-pass filter in the frequency domain is sampled to generate a discrete low-pass filter for each sampled frequency element. We remove the square border elements within four lines on each side whose values equal or very close to zero and then obtain a discrete low-pass filter $LPF(u, v, k)$ with the same size of the amplitude spectrum. The values of the sampled frequency elements are normalized again by dividing each element by the sum of all elements in the $LPF(u, v, k)$.

We propose a visual saliency model using Low-Pass Filtered Spectrum (LPFS). A set of low-pass filters $LPF(u, v, k)$ of various k-th roots of the 2D cosine function are used to filter the amplitude spectrum while keeping the phase spectrum unchanged. Saliency map candidates $S(x, y, k)$ can be constructed by the inverse transform of the Gaussian filtered amplitude spectrums $\mathcal{A}_{LPFS}(u, v, k)$ with the original phase spectrum $\mathcal{P}(u, v)$.

$$\mathcal{A}_{LPFS}(u, v, k) = \mathcal{A}(u, v) \star LPF(u, v, k), \tag{2.52}$$

$$S(x, y, k) = T^{-1}[\mathcal{A}(u, v) \star LPF(u, v, k) \cdot exp(i \cdot \mathcal{P}(u, v))], \tag{2.53}$$

where $\frac{1}{k}$ denotes the k-th root in the low-pass filter $LPF(u, v, k)$ and $k = 4^{n-1}, n = \{1, \dots, N\}$. N is determined by the largest dimension of the size of the saliency map, $N = \lfloor log_4(max(H, W)) \rfloor + 2$, where W and H are the width and height of the saliency map. For example, if the size of the saliency map is 64 × 48, $N = 5$, $n = \{1, 2, 3, 4, 5\}$, and $k = \{1, 4, 16, 64, 256\}$. An output saliency map $S'(x, y, k')$ is selected by minimizing the entropy $\mathcal{H}(S(x, y, k))$ among the set of candidates using the same Equation (2.36) and (2.37). The final LPFS saliency map is generated by Equation (2.39).

2.3.7 Visual Saliency Model Using Low-Pass Filtered Log Spectrum (LPFLS)

Following our Low-Pass Filtered Spectrum (LPFS) model, we also develop a visual saliency model using the Low-Pass Filtered Log Spectrum (LPFLS). A set of low-pass filters $LPF(u, v, k)$ of various k-th roots of a 2D cosine function are employed to filter the log amplitude spectrum while keeping the phase spectrum unchanged. For convenience, we only describe the main steps in the following equations.

$$\mathcal{L}_{LPFLS}(u, v, k) = \mathcal{L}(u, v) \star LPF(u, v, k), \tag{2.54}$$

$$S(x, y, k) = T^{-1}[exp(\mathcal{L}(u, v) \star LPF(u, v, k) + i \cdot \mathcal{P}(u, v))]. \tag{2.55}$$

We use the same parameter settings as the LPFS model and an output saliency map $S'(x, y, k')$ is generated by the same selection approach as Equation (2.36). The final LPFLS saliency map is obtained by Equation (2.39).

2.3.8 Visual Saliency Model Using Gaussian Filtered Spectrum (GFS)

Inspired by the related work [35], we propose another visual saliency model using a Gaussian Filtered Spectrum (GFS). A set of Gaussian filters $GF(u, v, k)$ with various standard deviations σ_k are used to filter the amplitude spectrum while keeping the phase spectrum unchanged. Saliency map candidates $S(x, y, k)$ can be constructed by the inverse transform of the Gaussian filtered amplitude spectrums $\mathcal{A}_{GFS}(u, v, k)$ with the original phase spectrum $\mathcal{P}(u, v)$.

$$\mathcal{A}_{GFS}(u, v, k) = \mathcal{A}(u, v) \star GF(u, v, k), \tag{2.56}$$

$$S(x, y, k) = T^{-1}[\mathcal{A}(u, v) \star GF(u, v, k) \cdot exp(i \cdot \mathcal{P}(u, v))], \tag{2.57}$$

where k is an index $k = \{1, \ldots, K\}$ and $\sigma_k = 4^{k-1}$. K is determined by the largest dimension of the size of the saliency map, $K = \lfloor log_4(max(H, W)) \rfloor + 2$, where W and H are the width and height of the saliency map. For example, if the size of the saliency map is 64×48, $K = 5$, $k = \{1, 2, 3, 4, 5\}$, and $\sigma_k = \{1, 4, 16, 64, 256\}$. An output saliency map $S'(x, y, k')$ is selected by minimizing the entropy $\mathcal{H}(S(x, y, k))$ among the set of candidates using the same Equation (2.36) and (2.37). The final GFS saliency map is generated by Equation (2.39).

2.3.9 Visual Saliency Model Using Gaussian Filtered Log Spectrum (GFLS)

Following our Gaussian Filtered Spectrum (GFS) model, we also develop a visual saliency model using the Gaussian Filtered Log Spectrum (GFLS). A set of Gaussian filters $GF(u, v, k)$ with various standard deviations σ_k are used to filter the log amplitude spectrum while keeping the phase spectrum unchanged. For convenience, we only describe the main steps in the following equations.

$$\mathcal{L}_{GFLS}(u, v, k) = \mathcal{L}(u, v) \star GF(u, v, k), \tag{2.58}$$

$$S(x, y, k) = T^{-1}[exp(\mathcal{L}(u, v) \star GF(u, v, k) + i \cdot \mathcal{P}(u, v))]. \tag{2.59}$$

We use the same parameter settings as the GFS model and an output saliency map $S'(x, y, k')$ is generated by the same selection approach as Equation (2.36). The final GFLS saliency map is obtained by Equation (2.39).

2.3.10 Naming Convention of the Extended Models

We also develop several extended models by extending our proposed models to fit both separate and composite model families and variant color spaces. The **naming**

convention of extended models is defined as "**A-B-C**", where **A** represents a proposed model's abbreviation (*i.e.* GCS, GCLS, LPFS, LPFLS, GFS, and GFLS) or an existing model's abbreviation (*i.e.* IS and SSA); **B** represents a specific transform used for an extended model (FT and DCT used for **separate model family** while HFT used for **composite model family**); **C** represents a particular color space used for an extended model, including Lab, IRGBY, and RGB color spaces.

2.3.11 Visual Saliency Model Evaluation

Popular evaluation measures for visual saliency model comparison are briefly reviewed. We discuss some challenges and open issues in model comparison and then explained some ways to resolve them. Experimental results of comprehensive model evaluations are shown next in Section 2.4.

The motivation for evaluating models with more than one measure is to ensure that the main conclusions are independent of the choice of qualitative measures. A ground-truth saliency map is denoted by G, which is based on the eye fixation array of an image built by inserting 1s at fixation locations and 0s at the other locations. The ground-truth saliency map G is usually computed by convoluting the eye fixation array with a certain Gaussian kernel for smoothing. An estimated saliency map is denoted by S, which is generated by a visual saliency model.

Normalized Scanpath Saliency (NSS)

Normalized scanpath saliency is the average of the response values at human eye positions (x_h, y_h) in a model's saliency map S [68]. Its values are normalized to have zero mean and unit standard deviation.

$$\mathrm{NSS}(G,S) = \frac{1}{\sigma_S}(S(x_h,y_h) - \mu_S), \tag{2.60}$$

where μ_S and σ_S are the mean and the standard deviation of the values in the saliency map S. NSS is computed once for each saccade and subsequently the mean and standard error are computed across the set of NSS scores. When NSS $= 1$, the subjects's eye positions fall in a region whose predicted saliency is one standard deviation above average. NSS ≥ 1 indicates that the saliency map exhibits significantly higher saliency values at human fixated locations compared to other locations. NSS ≤ 0 means that the model performs no better than picking a random position and hence is at chance in predicting human gaze.

Kullback-Leibler (KL) Divergence

The KL divergence is usually used to measure distance between two probability distributions. Using similar concept, it is used to measure the distance between distributions of saliency values at human versus random eye positions [69, 70]. The saliency magnitude at each sampled location is first normalized in the range $[0, 1]$. The histogram of these magnitudes in l bins in the range $[0, 1]$ across all eye movements is calculated. H_k and R_k are the fraction of points in the bin k for salient and random points respectively. The symmetric KL divergence (relative entropy) using the difference between these histograms is defined as follows.

$$\mathrm{KL} = \frac{1}{2}\sum_{k=1}^{l}\left(H_k log_2\left(\frac{H_k}{R_k}\right) + R_k log_2\left(\frac{R_k}{H_k}\right)\right). \tag{2.61}$$

Linear Correlation Coefficient (CC)

The linear correlation coefficient measures the strength of a linear relationship between two saliency maps [71].

$$\mathrm{CC}(G, S) = \frac{\sum_{x,y}(G(x,y) - \mu_G)\cdot(S(x,y) - \mu_S)}{\sqrt{\sigma_G^2 \cdot \sigma_S^2}}, \tag{2.62}$$

where μ_G and μ_S are the means while σ_G^2 and σ_S^2 are the variances of the G and S saliency maps, respectively. When CC is close to +1 or 1 there is almost a perfectly linear relationship between the two saliency maps.

Area Under The Curve (AUC)

AUC is the area under the Receiver Operating Characteristics (ROC) [72]. In the context of saliency map evaluation, eye fixation points are considered as the positive set and some points from the image are sampled to form the negative set [73]. The saliency map S is then treated as a binary classifier to separate the positive samples from the negative samples. By thresholding the saliency map at variant threshold levels and plotting True Positive Rate (TPR) against False Positive Rate (FPR), an ROC is obtained for each image.

$$TPR = \frac{TP}{TP+FN}, \tag{2.63}$$

$$FPR = \frac{FP}{FP+TN}, \tag{2.64}$$

where TP is the number of true positives, FP is the number of false positives, TN is the number of true negatives, and FN is the number of false negatives. Figure 2.6 demonstrates the classification of true positive, false positive, true negative, and false negative. The area underneath of each ROC is calculated for an image and the the final AUC score is averaged over all images. Perfect prediction corresponds to a score of 1 while a score of 0.5 indicates chance level.

Shuffled Area Under The Curve (sAUC)

As [10,38,73] pointed out, human eye fixations are often biased toward the center of an image and this strong center-bias do significantly affect the performance evaluation of visual saliency models using above evaluation measures. Based on [38,73], a shuffled Area Under The Curve (sAUC) is proposed to resolve this issue. In order to remove

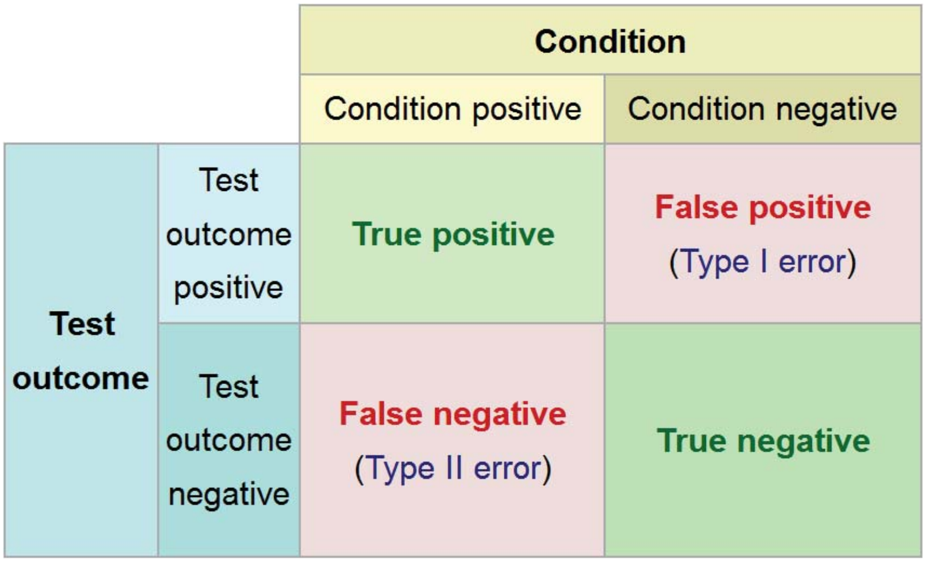

		Condition	
		Condition positive	Condition negative
Test outcome	Test outcome positive	True positive	False positive (Type I error)
	Test outcome negative	False negative (Type II error)	True negative

Fig. 2.6. The classification of true positive, false positive, true negative, and false negative.

this center-bias effect, no pixel point from the image is used as a valid sample in this case and only eye fixation points are considered as either positive samples or negative samples. The positive sample set is composed of the eye fixation points of all subjects on that image. The negative sample set contains the union of all eye fixation points across all images from the same image dataset, but excludes those points in the positive sample set. Figure 2.7 illustrates an example of some prerequisites for computing sAUC score. Note that the positive and a negative sample sets in (C) and (D) are both Gaussian blurred and represented as heat maps for clear display, but the sAUC calculation is based on the actual eye fixation points. Each saliency map is first thresholded into a binarized map, which is employed as a binary classifier to separate the positive samples from negative samples. At a particular threshold level, the True Positive Rate (TPR) is the proportion of the positive samples that fall in the positive (white) region of the binarized map among all positive samples. Similarly, the False Positive Rate (FPR) is the proportion of the negative samples that fall in the positive (white) region of the binarized map among all negative samples. We calculate a pair of TPR and FPR to obtain a point on the Receiver Operating Characteristics (ROC) [72] (TPR versus FPR) based on a binarized map from a certain threshold.

$$TPR = \frac{TP}{TP+FN}, \tag{2.65}$$

$$FPR = \frac{FP}{FP+TN}, \tag{2.66}$$

where TP is the number of true positives, FP is the number of false positives, TN is the number of true negatives, and FN is the number of false negatives.

Thresholding the saliency map at many threshold levels obtains a group of points on the ROC and connecting these points yields a shuffled ROC. The area under this curve is called the shuffled Area Under Curve (sAUC). The sAUC scores $< \ 0.5$ indicate a negative correlation while the sAUC scores $> \ 0.5$ indicate a positive correlation. Perfect prediction leads to a sAUC score of 1.0 and chance level yields 0.5. Figure 2.8 demonstrates an example of the shuffled ROC used for computing the sAUC score. The blue curve shows the shuffled ROC of the generated saliency map for this image while the red reference line indicating the shuffled ROC of chance level. The sAUC score of the black curve is 0.6329 and the one of the red reference line is 0.5.

All of above evaluation measures (except the sAUC) are significantly affected by the center-bias and sAUC is more robust to center-bias and border effect [10]. The sAUC score provides a good evaluation measure of the saliency map to accurately predict where eye fixations occurred on an image. In order to fairly evaluate the consistency between a saliency map and a set of fixations of an image dataset, we employ **shuffled Area Under Curve (sAUC)** score as the evaluation measure in our experiments.

2.3.12 Parameter Issues

Another issue regarding fair model comparison is how to adjust the parameters of saliency models for different image datasets. It has been shown that blur-

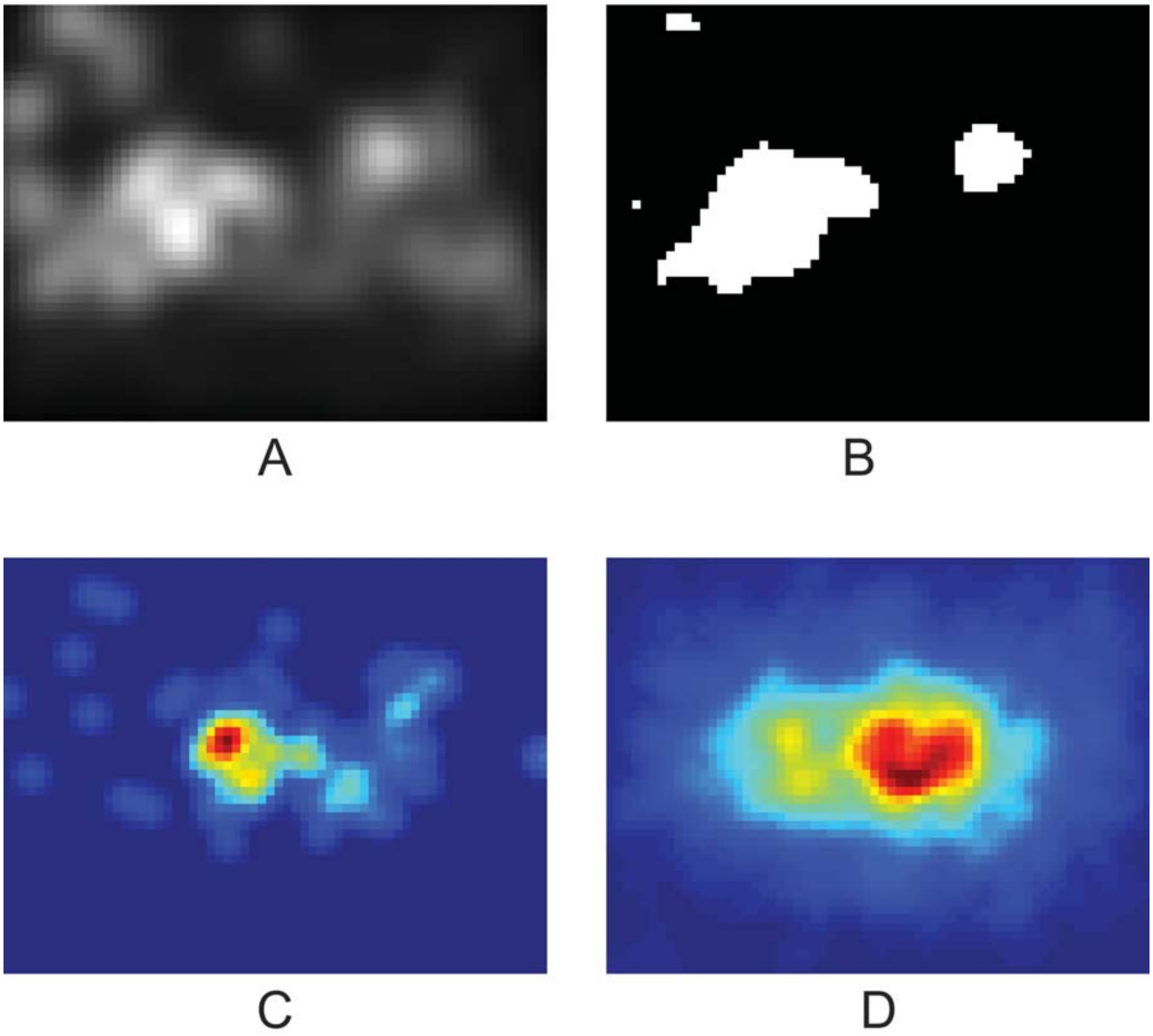

Fig. 2.7. An example of some prerequisites for computing sAUC score. (A) The generated saliency map on a certain image, (B) The binarized saliency map thresholded at 0.5, (C) The positive sample set of eye fixation points only on this image (Gaussian blurred heat map representation), (D) The negative sample set of eye fixation points containing all fixation points across the entire image dataset but excluding those points in the positive sample set (Gaussian blurred heat map representation). Reproduced from [33]

ring/smoothing the resulting saliency maps has a significant influence on the sAUC score of visual saliency models [33]. Some models provided the best settings of parameters for one image dataset, but sometime it's not a good settings for other

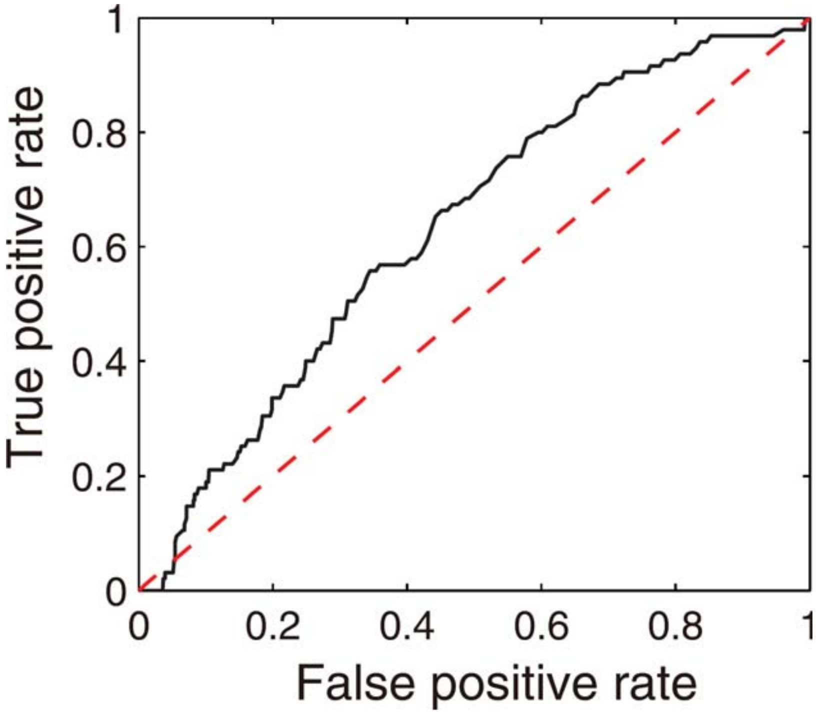

Fig. 2.8. An example of the shuffled ROC used for computing the sAUC score (true positive rate (TPR) versus false positive rate (FPR)). Reproduced from [33]

image datasets. We need to tune each model to achieve its best performance for a certain image dataset by searching and selecting the optimal scale of Gaussian blurring/smoothing. Ultimately, the model parameter issue will be better resolved through an online challenge, where researchers can tune their own models to achieve the best performance for different image datasets and share the resulting saliency maps.

2.4 Experimental Results

Previous studies have shown that top-ranked visual saliency models are capable of providing significantly accurate prediction of human eye fixation on natural images in free viewing [7–10]. To evaluate the performance of our visual saliency models, we did experiments to compare the proposed visual saliency models with some state-of-the-art models. Our experiment is to use the proposed and existing visual saliency models to predict human eye fixation on two standard image datasets. It should be noted we did not do any actual eye fixation studies but used standard datasets. We implemented all the extended models in MATLAB and set the saliency map's resolution to 64 × 48 pixels in all the experiments. We used the original MATLAB implementation of models with the default settings and the recommended saliency map's resolution. The experiments were executed on a backend server with four quad-core 3.2GHz CPU and 32GB RAM.

2.4.1 Predicting Eye Fixation

Eye Fixation Image Datasets

We adopted the shuffled AUC (sAUC) score [38, 73] as the evaluation measure and developed an evaluation tool for benchmarking visual saliency models based on a standard benchmark [33]. We did several experiments in predicting eye fixation using two standard image datasets. (1) The Bruce and Tsotsos (BT) dataset [27] is the most widely used dataset for comparing visual saliency models. It contains 120 color images with resolution of 681x511 pixels from indoor and outdoor scenes and the eye fixation data is based on 20 subjects. (2) The Li *et al.*'s (Li) dataset [35] is a new dataset containing 235 color images with resolution of 640x480 pixels in six categories. 50 images with large salient regions, 80 with intermediate salient regions, 60 with small salient regions, 15 with cluttered backgrounds, 15 with repeating distractors, and 15 with both large and small salient regions. Because blurring/smoothing the resulting saliency maps is an important factor for fair comparison [33], we tune up each model to achieve its best performance for above image datasets by searching and selecting the optimal parameter of Gaussian blurring/smoothing. We blurred the saliency map of each model by convoluting them with a series of Gaussian kernels with different standard deviations σ (from 0.005 to 0.1 in steps of 0.005) in terms of the largest dimension of an image. In our experiments, we kept all post-processing settings of each model as original except the blurring/smoothing parameter.

Comparison of Extended Models

We made a systematic comparison of the six groups of 36 extended saliency models that extends the proposed six visual saliency models by incorporating both separate and composite model families and using variant color spaces. Note that naming convention of extended models based on the six proposed models is provided in Section 2.3.10. 18 FT-based extended models using the separate visual saliency model family are compared with the baseline model SBVA(Itti) [25]. 18 HFT-based extended models using the composite visual saliency model family are also compared with the baseline model SBVA(Itti) [25]. Based on the two standard image datasets, Figure 2.9 and Figure 2.11 demonstrate the sAUC score of the FT-based extended models while Figure 2.10 and Figure 2.12 illustrate the sAUC score of the HFT-based extended models. Given the six groups of extended saliency models, the rank of the extended models, the maximum sAUC score, and the optimal Gaussian standard deviations σ_{opt} associated are shown in from Table 2.1 to Table 2.6. The results indicate that the Lab and IRGBY color spaces work better with the FT-based models in the separate model family and that the IRGBY color space works better with the HFT-based models in the composite model family. Regarding the three color spaces, Lab-based and IRGBY-based extended models are generally better than RGB-based extended models in predicting human eye fixation. For the six groups of extended saliency models, Table 2.7 shows the summary of the best extended models in the same model group. We select the best extended model in each group for next experiments, *i.e.* GCS-FT-Lab, GCLS-FT-Lab, LPFS-FT-Lab, LPFLS-HFT-IRGBY, GFS-FT-Lab, and GFLS-HFT-IRGBY.

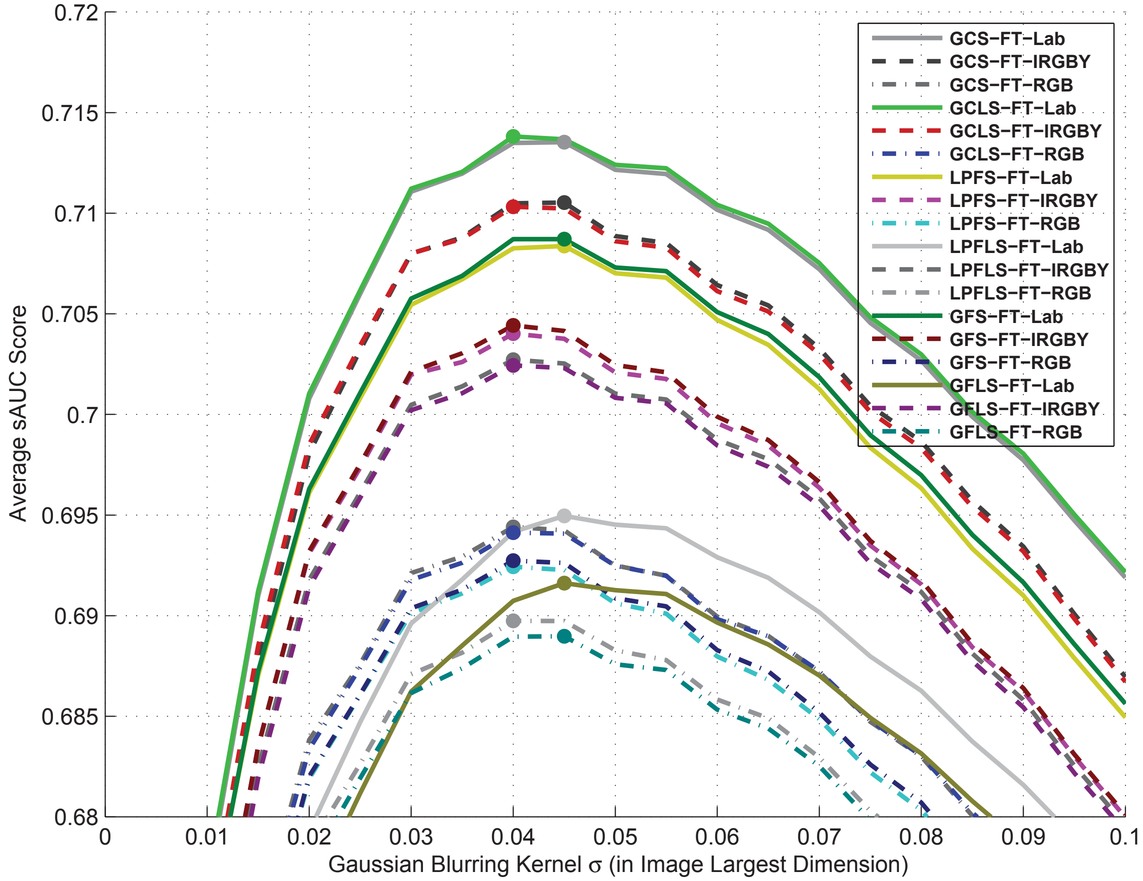

Fig. 2.9. The sAUC score of each FT-based model in the separate model family (BT dataset).

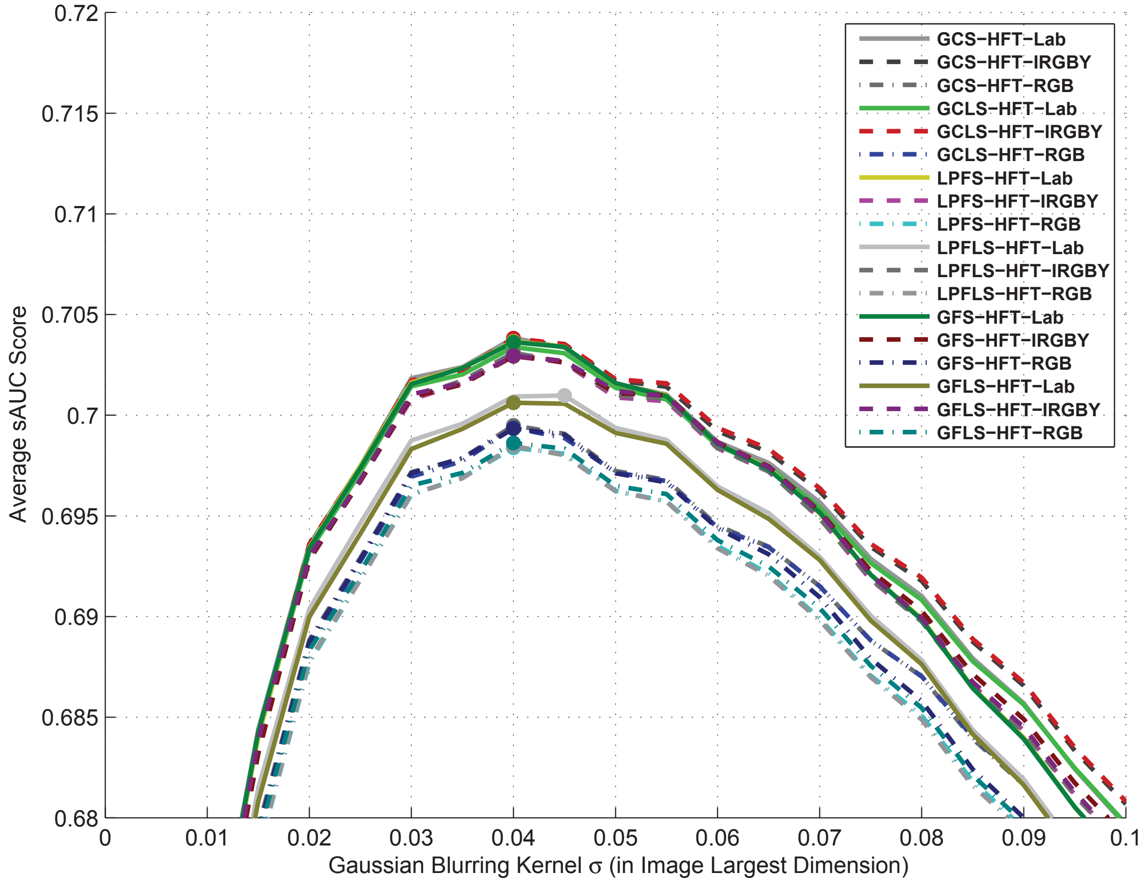

Fig. 2.10. The sAUC score of each HFT-based model in the composite model family (BT dataset).

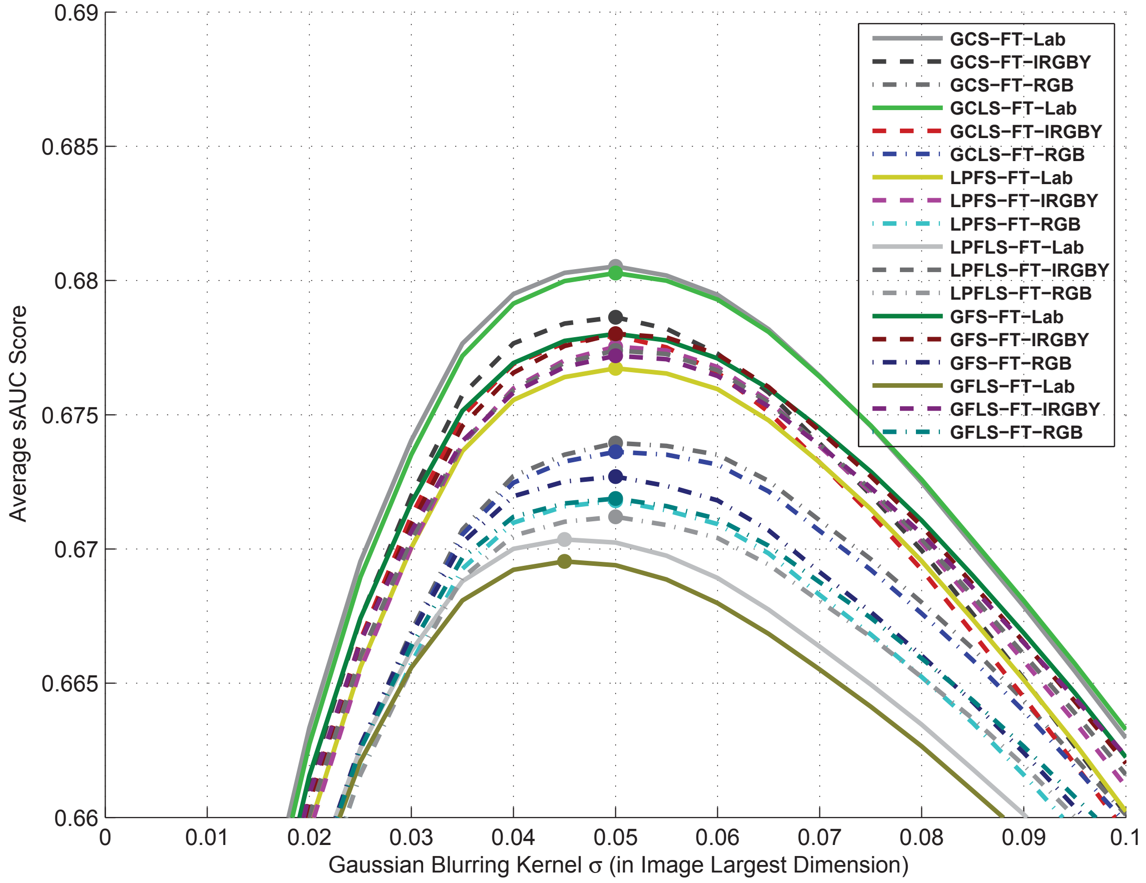

Fig. 2.11. The sAUC score of each FT-based model in the separate model family (Li dataset).

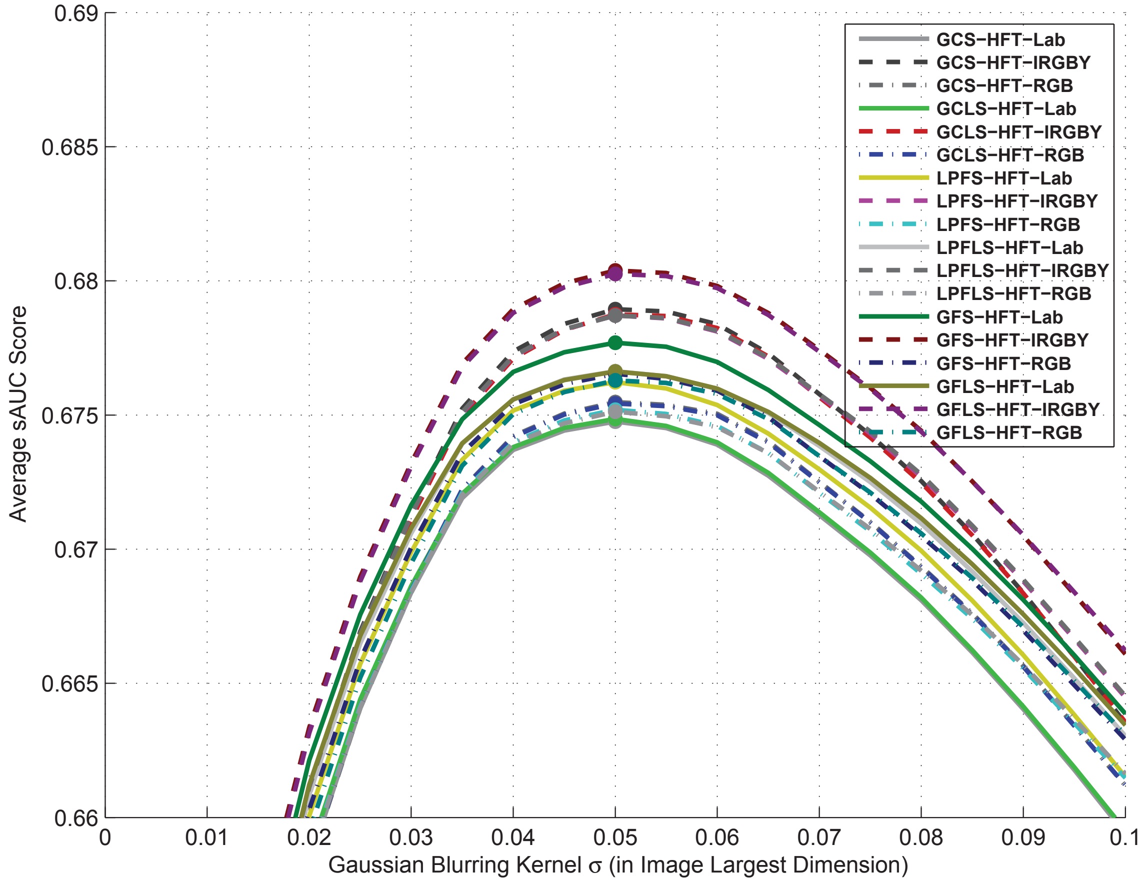

Fig. 2.12. The sAUC score of each HFT-based model in the composite model family (Li dataset).

Table 2.1
The rank of extended GCS models, the maximum sAUC score, and the associated Gaussian σ_{opt} (in image largest dimension).

Image	GCS-FT	GCS-HFT	GCS-FT	GCS-HFT	GCS-FT	GCS-HFT
Dataset	-Lab	-Lab	-IRGBY	-IRGBY	-RGB	-RGB
BT [27] Rank	**1**	3	2	4	6	5
Max sAUC	**0.7135**	0.7038	0.7105	0.7037	0.6944	0.6995
σ_{opt}	**0.045**	0.040	0.045	0.040	0.040	0.040
Li [35] Rank	**1**	5	3	2	6	4
Max sAUC	**0.6805**	0.6748	0.6786	0.6789	0.6739	0.6755
σ_{opt}	**0.050**	0.050	0.050	0.050	0.050	0.050

Table 2.2
The rank of extended GCLS models, the maximum sAUC score, and the associated Gaussian σ_{opt} (in image largest dimension).

Image	GCLS-FT	GCLS-HFT	GCLS-FT	GCLS-HFT	GCLS-FT	GCLS-HFT
Dataset	-Lab	-Lab	-IRGBY	-IRGBY	-RGB	-RGB
BT [27] Rank	**1**	4	2	3	6	5
Max sAUC	**0.7138**	0.7034	0.7103	0.7038	0.6941	0.6994
σ_{opt}	**0.040**	0.040	0.040	0.040	0.040	0.040
Li [35] Rank	**1**	5	3	2	6	4
Max sAUC	**0.6803**	0.6749	0.6779	0.6788	0.6736	0.6754
σ_{opt}	**0.050**	0.050	0.050	0.050	0.050	0.050

Table 2.3
The rank of extended LPFS models, the maximum sAUC score, and the associated Gaussian σ_{opt} (in image largest dimension).

Image	LPFS-FT	LPFS-HFT	LPFS-FT	LPFS-HFT	LPFS-FT	LPFS-HFT
Dataset	-Lab	-Lab	-IRGBY	-IRGBY	-RGB	-RGB
BT [27] Rank	**1**	3	2	4	6	5
Max sAUC	**0.7084**	0.7037	0.7040	0.7030	0.6924	0.6984
σ_{opt}	**0.045**	0.040	0.040	0.040	0.040	0.040
Li [35] Rank	**2**	4	3	1	6	5
Max sAUC	**0.6767**	0.6762	0.6775	0.6787	0.6718	0.6752
σ_{opt}	**0.050**	0.050	0.050	0.050	0.050	0.050

Table 2.4
The rank of extended LPFLS models, the maximum sAUC score, and the associated Gaussian σ_{opt} (in image largest dimension).

Image	LPFLS-FT	LPFLS-HFT	LPFLS-FT	LPFLS-HFT	LPFLS-FT	LPFLS-HFT
Dataset	-Lab	-Lab	-IRGBY	-IRGBY	-RGB	-RGB
BT [27] Rank	5	3	2	**1**	6	4
Max sAUC	0.6950	0.7010	0.7027	**0.7031**	0.6897	0.6985
σ_{opt}	0.045	0.045	0.040	**0.040**	0.040	0.040
Li [35] Rank	6	3	2	**1**	5	4
Max sAUC	0.6704	0.6766	0.6774	**0.6787**	0.6712	0.6751
σ_{opt}	0.045	0.050	0.050	**0.050**	0.050	0.050

Table 2.5
The rank of extended GFS models, the maximum sAUC score, and the associated Gaussian σ_{opt} (in image largest dimension).

Image Dataset	GFS-FT -Lab	GFS-HFT -Lab	GFS-FT -IRGBY	GFS-HFT -IRGBY	GFS-FT -RGB	GFS-HFT -RGB
BT [27] Rank	**1**	3	2	4	6	5
Max sAUC	**0.7087**	0.7036	0.7044	0.7029	0.6927	0.6993
σ_{opt}	**0.045**	0.040	0.040	0.040	0.040	0.040
Li [35] Rank	**2**	4	2	1	6	5
Max sAUC	**0.6780**	0.6777	0.6780	0.6804	0.6727	0.6765
σ_{opt}	**0.050**	0.050	0.050	0.050	0.050	0.050

Table 2.6
The rank of extended GFLS models, the maximum sAUC score, and the associated Gaussian σ_{opt} (in image largest dimension).

Image Dataset	GFLS-FT -Lab	GFLS-HFT -Lab	GFLS-FT -IRGBY	GFLS-HFT -IRGBY	GFLS-FT -RGB	GFLS-HFT -RGB
BT [27] Rank	5	3	2	**1**	6	4
Max sAUC	0.6916	0.7006	0.7024	**0.7030**	0.6890	0.6986
σ_{opt}	0.045	0.040	0.040	**0.040**	0.045	0.040
Li [35] Rank	6	3	2	**1**	5	4
Max sAUC	0.6695	0.6766	0.6772	**0.6803**	0.6719	0.6763
σ_{opt}	0.045	0.050	0.050	**0.050**	0.050	0.050

Table 2.7

The summary of the best extended models: The rank in the same model group, the maximum sAUC score, and the associated Gaussian σ_{opt} (in image largest dimension).

Image Dataset	GCS-FT -Lab	GCLS-FT -Lab	LPFS-FT -Lab	LPFLS-HFT -IRGBY	GFS-FT -Lab	GFLS-HFT -IRGBY
BT [27] Rank	**1**	**1**	**1**	**1**	**1**	**1**
Max sAUC	**0.7135**	**0.7138**	**0.7084**	**0.7031**	**0.7087**	**0.7030**
σ_{opt}	**0.045**	**0.040**	**0.045**	**0.040**	**0.045**	**0.040**
Li [35] Rank	**1**	**1**	**2**	**1**	**2**	**1**
Max sAUC	**0.6805**	**0.6803**	**0.6767**	**0.6787**	**0.6780**	**0.6803**
σ_{opt}	**0.050**	**0.050**	**0.050**	**0.050**	**0.050**	**0.050**

Comparison with Other Models

We did a comprehensive evaluation of the six best extended saliency models (GCS-FT-Lab, GCLS-FT-Lab, LPFS-FT-Lab, LPFLS-HFT-IRGBY, GFS-FT-Lab, and GFLS-HFT-IRGBY) by comparing with 10 saliency models from the literature using two standard image datasets. The 10 models compared in this experiment are: SBVA(Itti) [25], AIM [27], FTSD [29], PFDN [32], SR [65], PFT [30], PQFT [31], QDCT [34], IS-DCT-Lab [33], SSA-HFT-IRGBY [35] The SBVA(Itti) and AIM are spatial domain models while the FTSD, PFDN, SR, PFT, PQFT, IS-DCT-Lab, SSA-HFT-IRGBY and the six best extended models are all frequency domain models. Figure 2.13 and Figure 2.15 demonstrate the sAUC score of each model based on the two standard image datasets. Figure 2.14 and Figure 2.16 illustrate the average execution time per image of each model. Note that the time axis lower than 0.3 second uses a linear scale but it higher than 0.3 second is defined in a non-linear scale based on the largest value of the average execution time per image. Figure 2.13 and Figure 2.15 demonstrate the sAUC score of each model based on the two standard image datasets. Figure 2.14 and Figure 2.16 illustrate the average execution time per image of each model. Figure 2.17, Figure 2.18, and Figure 2.19 illustrate examples of saliency maps from different visual saliency models for the same images in the BT dataset. Figure 2.20, Figure 2.21, and Figure 2.22 illustrate examples of saliency maps from different visual saliency models for the same images in the Li dataset. Note that the table in the middle indicates the locations of the saliency maps corresponding to which visual saliency models.

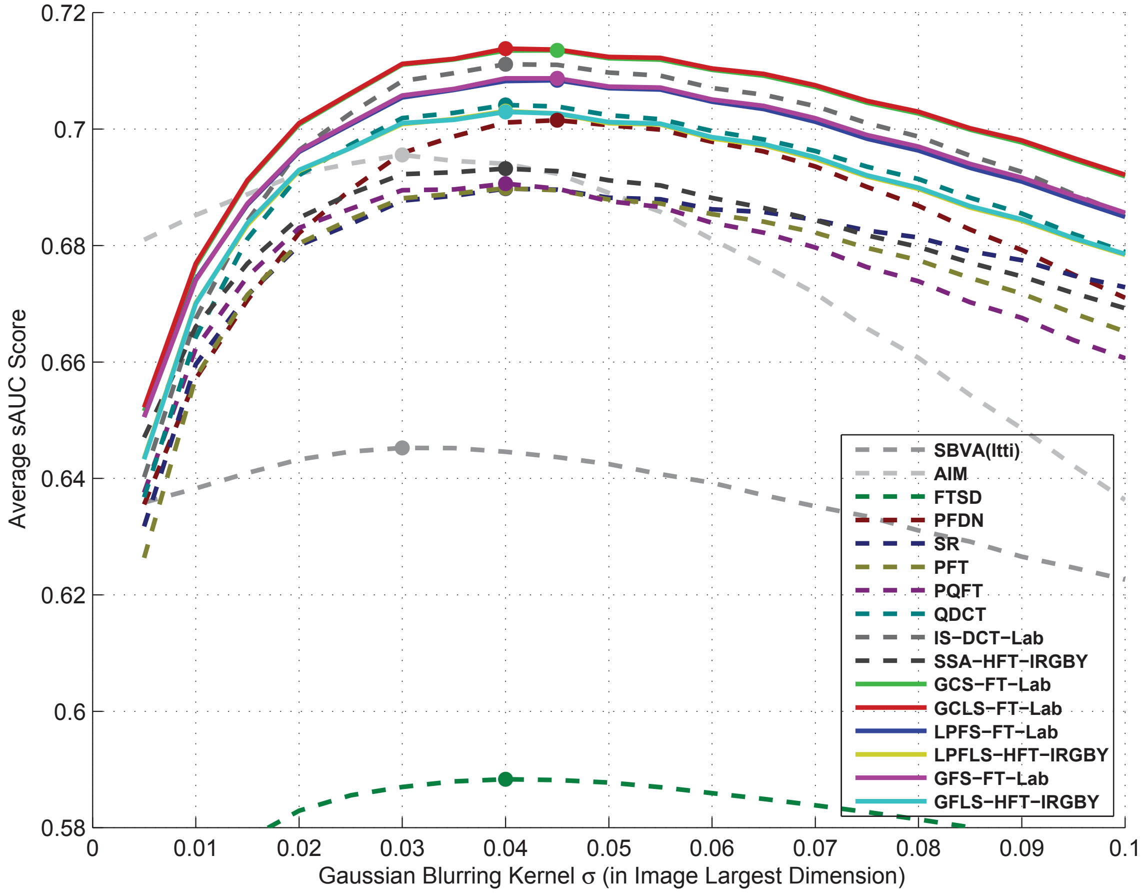

Fig. 2.13. The sAUC score of each model (BT dataset).

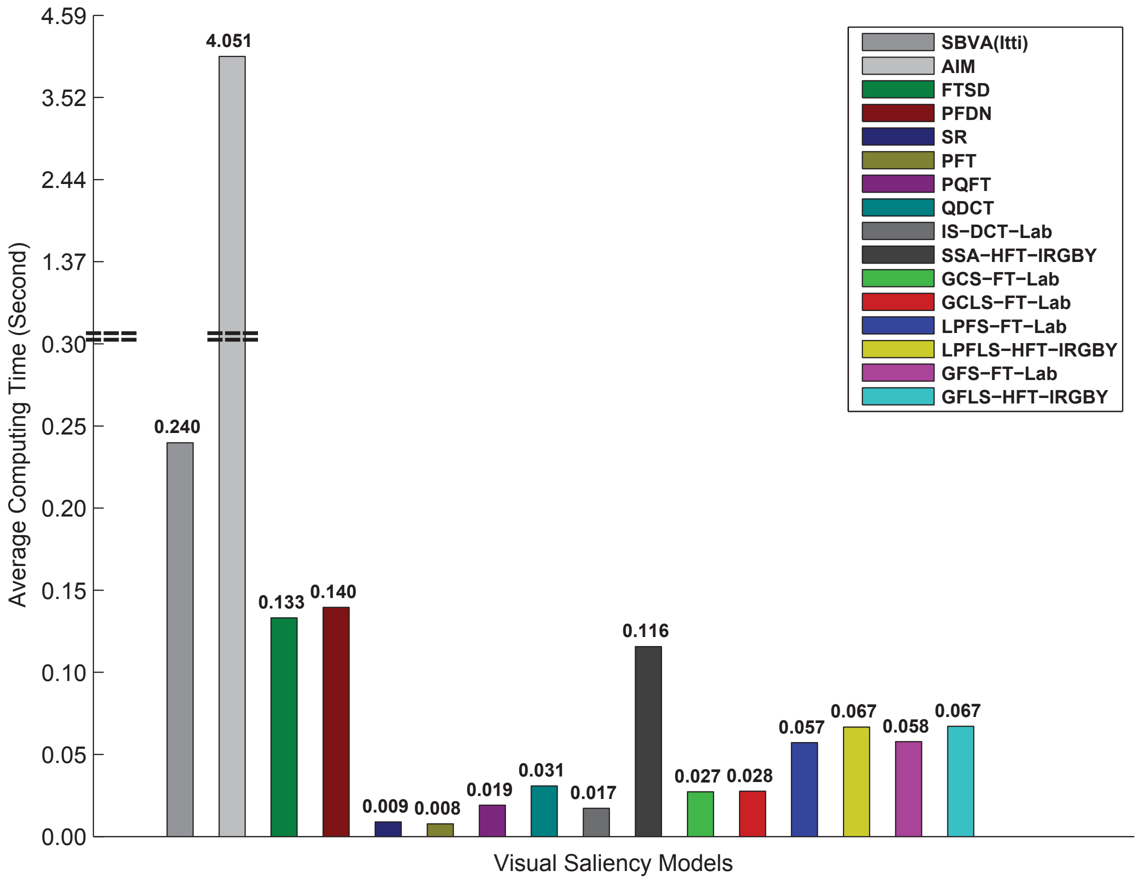

Fig. 2.14. The average execution time of each model (BT dataset).

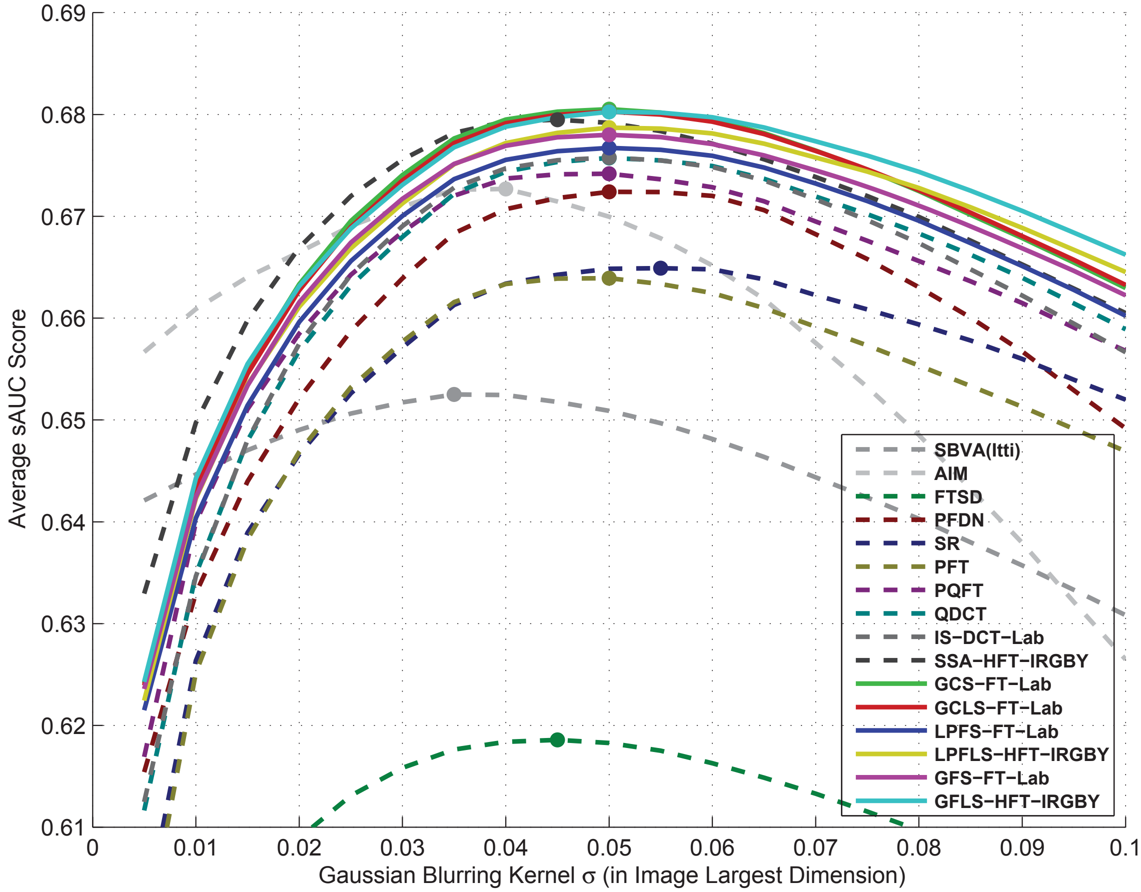

Fig. 2.15. The sAUC score of each model (Li dataset).

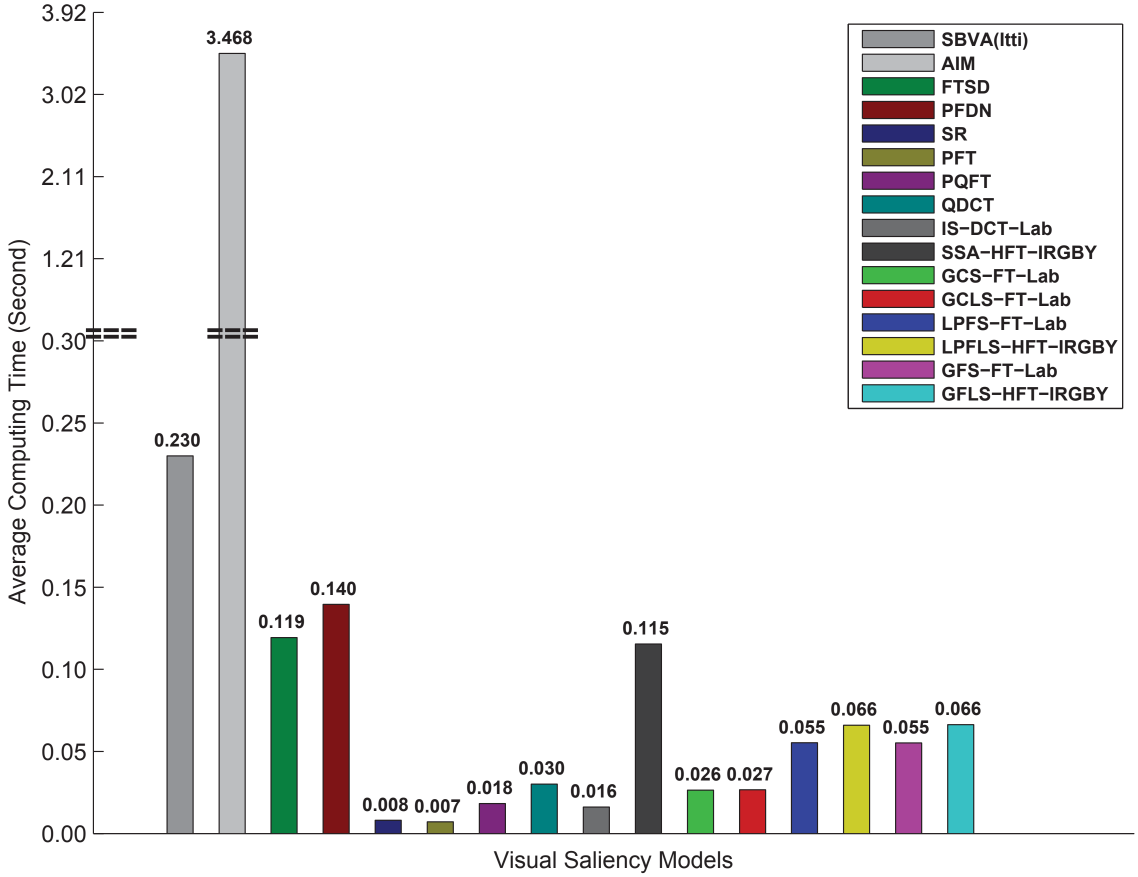

Fig. 2.16. The average execution time of each model (Li dataset).

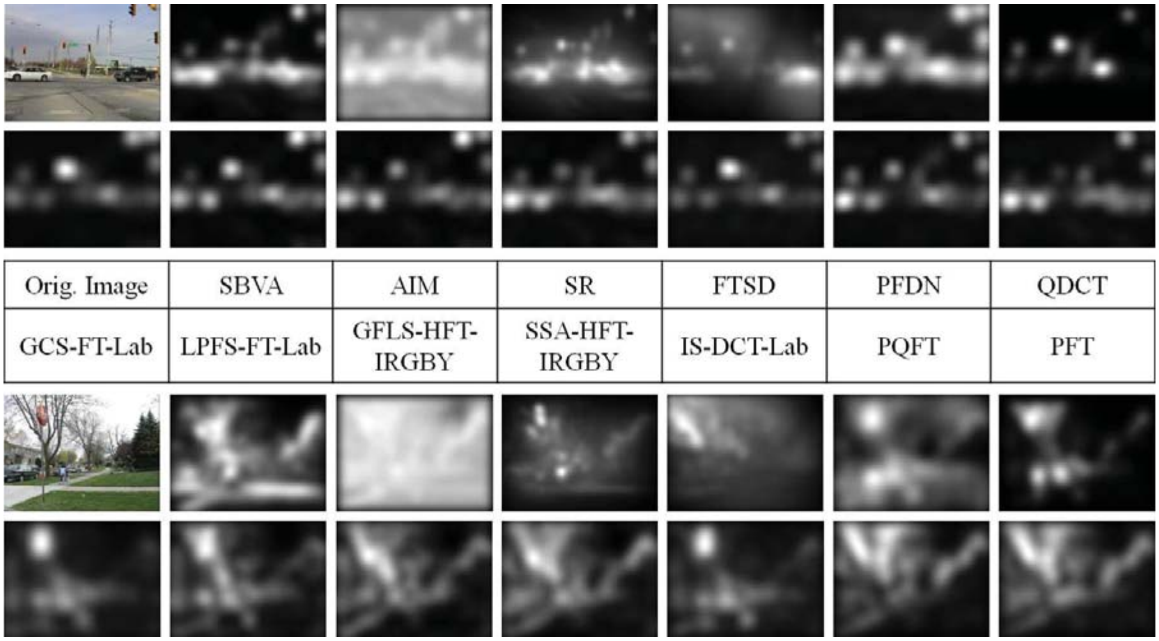

Orig. Image	SBVA	AIM	SR	FTSD	PFDN	QDCT
GCS-FT-Lab	LPFS-FT-Lab	GFLS-HFT-IRGBY	SSA-HFT-IRGBY	IS-DCT-Lab	PQFT	PFT

Fig. 2.17. Examples of saliency maps from different models for two images (BT dataset).

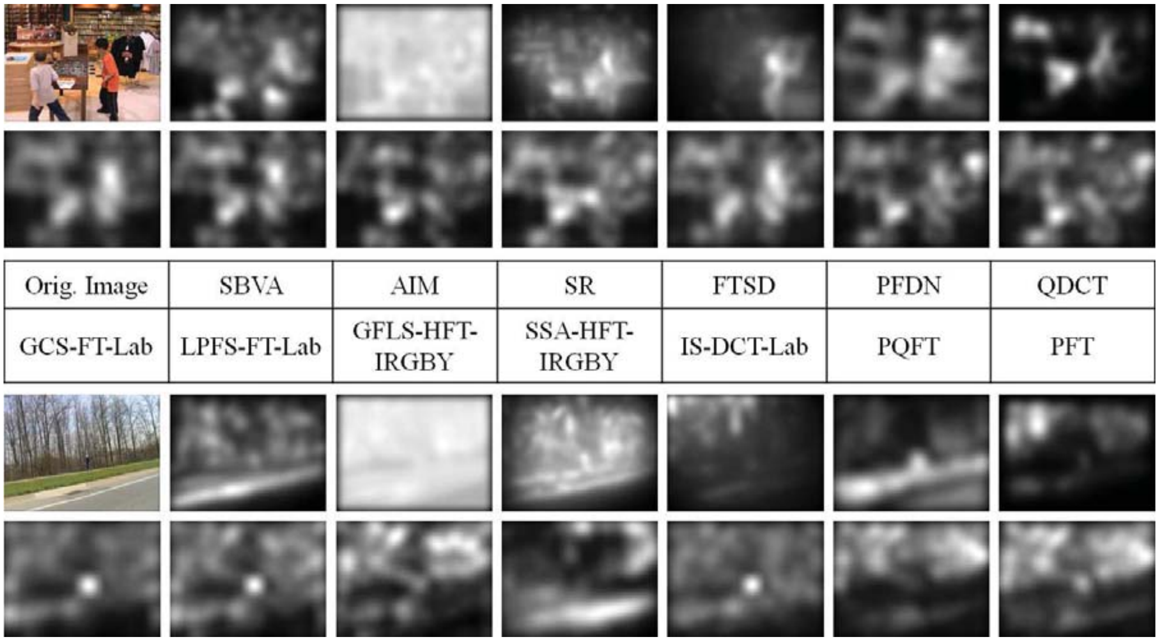

Orig. Image	SBVA	AIM	SR	FTSD	PFDN	QDCT
GCS-FT-Lab	LPFS-FT-Lab	GFLS-HFT-IRGBY	SSA-HFT-IRGBY	IS-DCT-Lab	PQFT	PFT

Fig. 2.18. Examples of saliency maps from different models for two images (BT dataset).

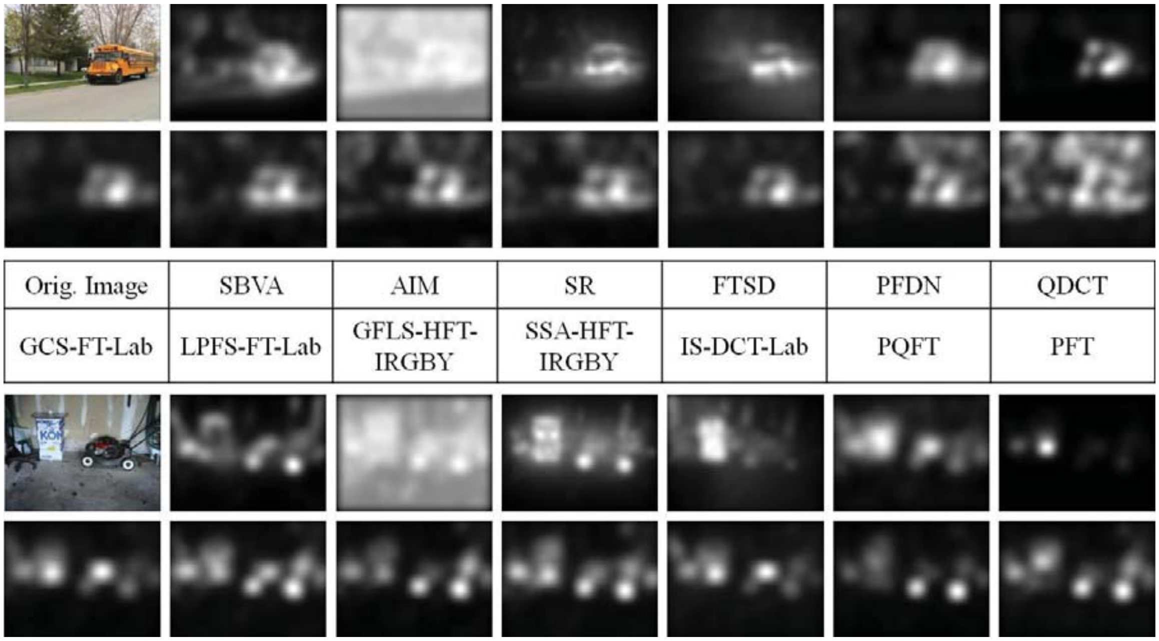

Orig. Image	SBVA	AIM	SR	FTSD	PFDN	QDCT
GCS-FT-Lab	LPFS-FT-Lab	GFLS-HFT-IRGBY	SSA-HFT-IRGBY	IS-DCT-Lab	PQFT	PFT

Fig. 2.19. Examples of saliency maps from different models for two images (BT dataset).

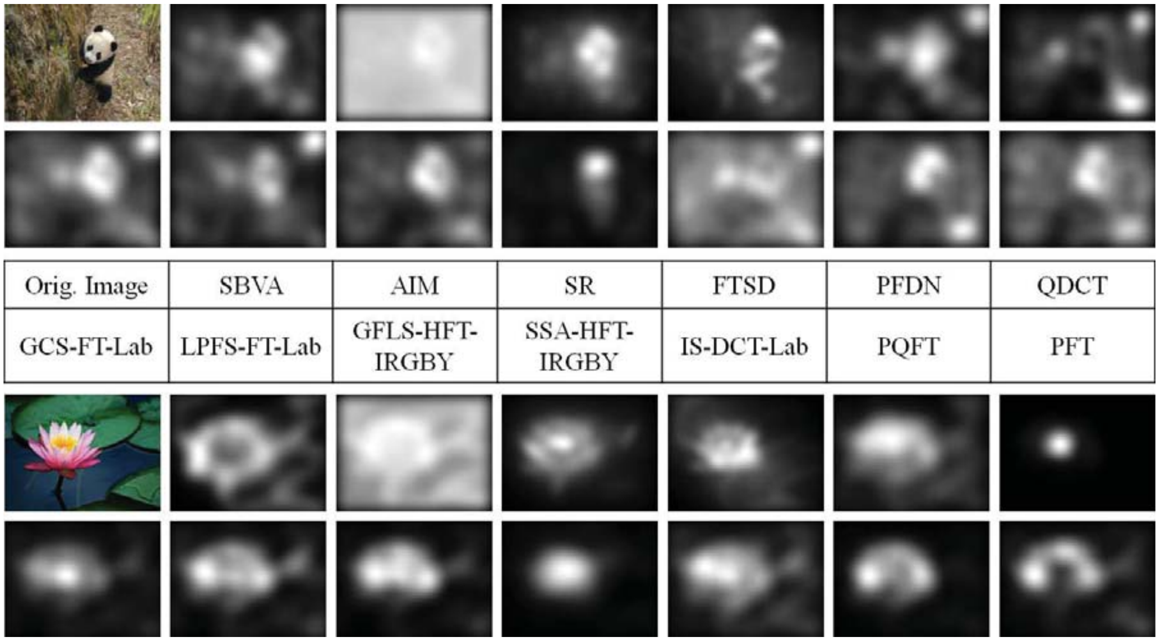

Orig. Image	SBVA	AIM	SR	FTSD	PFDN	QDCT
GCS-FT-Lab	LPFS-FT-Lab	GFLS-HFT-IRGBY	SSA-HFT-IRGBY	IS-DCT-Lab	PQFT	PFT

Fig. 2.20. Examples of saliency maps from different models for two images (Li dataset).

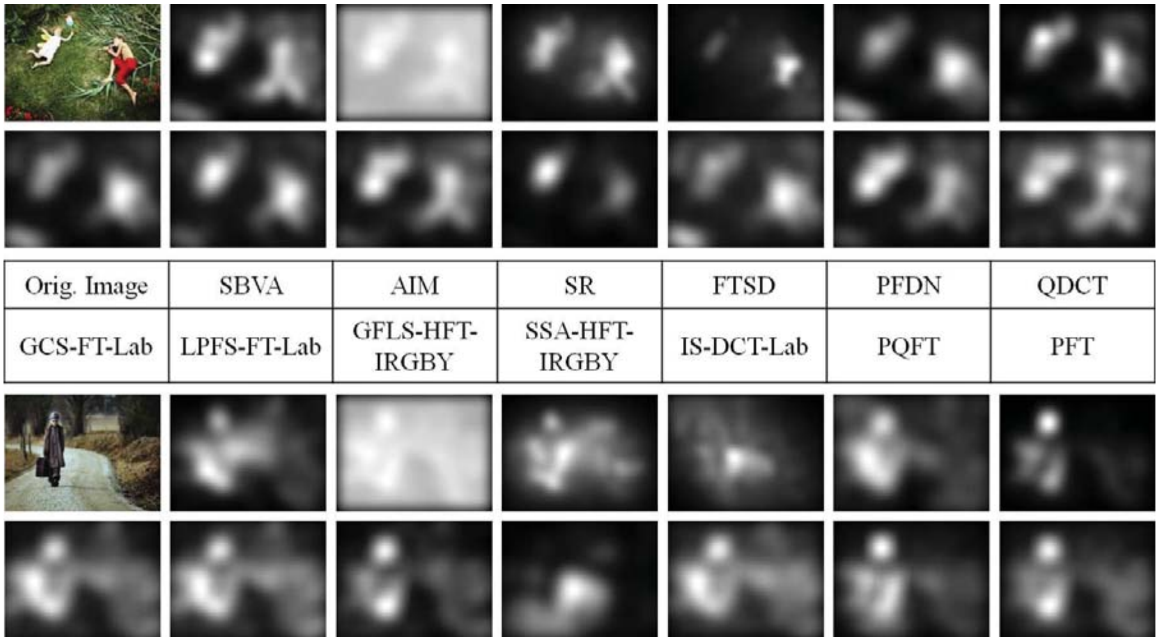

Orig. Image	SBVA	AIM	SR	FTSD	PFDN	QDCT
GCS-FT-Lab	LPFS-FT-Lab	GFLS-HFT-IRGBY	SSA-HFT-IRGBY	IS-DCT-Lab	PQFT	PFT

Fig. 2.21. Examples of saliency maps from different models for two images (Li dataset).

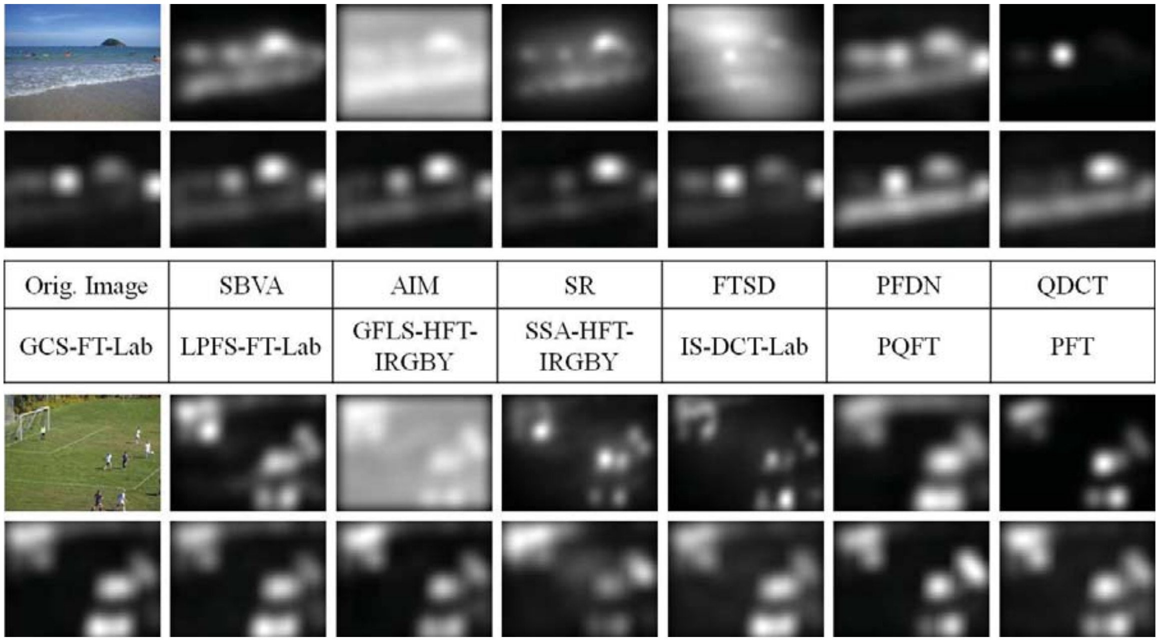

Fig. 2.22. Examples of saliency maps from different models for two images (Li dataset).

Table 2.8 shows the rank of each saliency model, the maximum sAUC score, and the optimal Gaussian standard deviations σ_{opt} associated. The results show that the six best extended models are generally better than most state-of-the-art models because they are ranked in the top 8 out of all the 16 models for the BT dataset and the top 7 out of all the 16 models for the Li dataset. Among the existing models, IS-DCT-Lab [33], SSA-HFT-IRGBY [35], and QDCT [34] models performed better than the rest while SBVA(Itti) [25], FTSD [29], SR [65], PFT [30] models are ranked at the bottom. The proposed GCS-FT-Lab model has the highest sAUC score for the Li dataset and is ranked the 2nd place among all models for the BT dataset. The proposed GCLS-FT-Lab model has the highest sAUC score for the BT dataset and is ranked the 2nd place among all models for the Li dataset. The QDCT model has higher sAUC scores for the two datasets and it is ranked the 6th place for the BT dataset and the 9th place for the Li dataset. The two spatial domain models, SBVA(Itti) and AIM, have relatively low sAUC scores for the two datasets and they are the two slowest models in terms of average computing time per image in Figure 2.14 and Figure 2.16. For the BT dataset, SBVA(Itti) is about 8.9x slower and AIM is about 150.0x than the proposed GCS-FT-Lab model. For the Li dataset, SBVA(Itti) is about 8.8x slower and AIM is about 133.4x than the proposed GCS-FT-Lab model. Moreover, the GCS-FT-Lab and GCLS-FT-Lab models are the two most accurate ones in predicting eye fixation. Since the GCS-FT-Lab model has lower complexity and is more efficient than GCLS-FT-Lab model, we select **GCS-FT-Lab model** as the best one of all the 16 models.

Table 2.8
The rank of each saliency model, the maximum sAUC score, and the associated Gaussian σ_{opt} (in image largest dimension).

Image Dataset	SBVA [25]	AIM [27]	FTSD [29]	PFDN [32]	SR [65]	PFT [30]	PQFT [31]	QDCT [34]	IS-DCT -Lab [33]	SSA-HFT -IRGBY [35]	GCS-FT -Lab	GCLS-FT -Lab	LPFS-FT -Lab	LPFLS-HFT -IRGBY	GFS-FT -Lab	GFLS-HFT -IRGBY
BT [27] Rank	15	10	16	9	13	13	12	6	**3**	11	**2**	**1**	5	7	**4**	8
Max sAUC	0.6453	0.6956	0.5883	0.7015	0.6898	0.6898	0.6906	0.7041	0.7111	0.6932	0.7135	0.7138	0.7084	0.7031	0.7087	0.7030
σ_{opt}	0.030	0.030	0.040	0.045	0.040	0.040	0.040	0.040	0.040	0.040	0.045	0.040	0.045	0.040	0.045	0.040
Li [35] Rank	15	11	16	12	13	14	10	9	8	**4**	**1**	**2**	7	5	6	**2**
Max sAUC	0.6525	0.6727	0.6186	0.6724	0.6649	0.6639	0.6742	0.6757	0.6758	0.6795	0.6805	0.6803	0.6767	0.6787	0.6780	0.6803
σ_{opt}	0.035	0.040	0.045	0.050	0.055	0.050	0.050	0.050	0.050	0.045	0.050	0.050	0.050	0.050	0.050	0.050

Discussion

Our proposed GCS-FT-Lab and GCLS-FT-Lab models both achieve the top performance for the two standard image datasets. Their performance is nearly consistent over the two datasets but the performance of some visual saliency models vary over different image datasets. The IS-DCT-Lab model [33] is among the top 3 models for the BT dataset but results in average capability for the Li dataset. The SSA-HFT-IRGBY model [35] is among the top 3 models for the Li dataset but performs in the lower middle for the BT dataset. A reason could be that the two standard image datasets have different distributions of eye fixation due to the characteristics of the image datasets in terms of image/feature statistics, object/scene varieties, and eye tracking biases. Figure 2.23 and Figure 2.24 illustrate the distribution and the Gaussian blurred heat map representation of eye fixation of all the images in the two datasets. The eye fixation of the BT dataset are less center-biased than the ones of the Li dataset. We observed that the BT dataset images contain more sparse and small salient objects while the Li dataset images include more dense and large salient objects. This indicates that the IS-DCT-Lab model is good at detecting sparse and small salient objects, the SSA-HFT-IRGBY model works better in capturing dense and large salient objects, and the proposed GCS-FT-Lab model and GCLS-FT-Lab models are good at both tasks.

Note that our GFLS-HFT-IRGBY model is similar to the SSA-HFT-IRGBY model [35] using the same transform and color space. But it is different from the SSA-HFT-IRGBY model in the way that the output saliency map is selected by minimizing entropy directly. When the spectrum scale-space is constructed to select an optimal scale for SSA-HFT-IRGBY model, an additional Gaussian kernel is used to filter each saliency map candidate and then minimizing entropy is employed [35]. However, our experimental results indicate that the additional Gaussian filtering provides a limited benefit in predicting dense eye fixation but has a significant disadvantage in predicting sparse eye fixation.

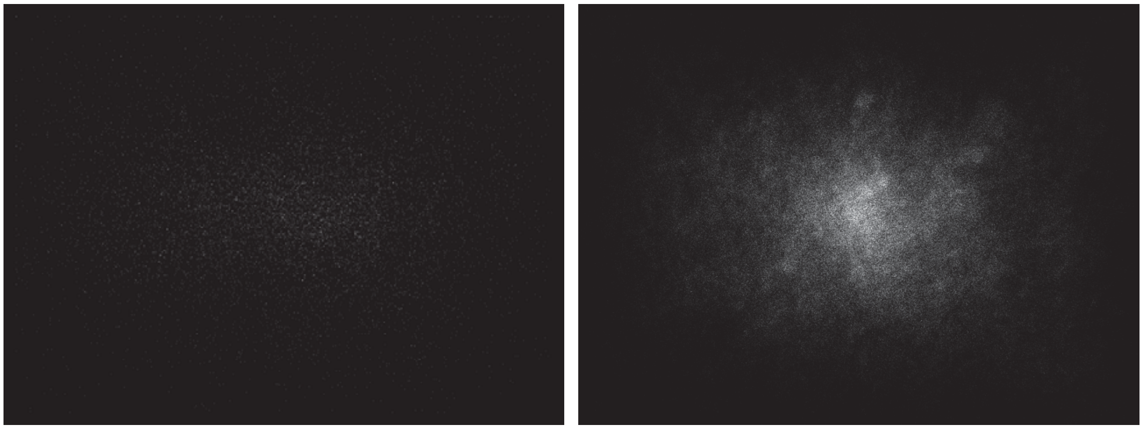

Fig. 2.23. The distribution of eye fixation of all the images in BT dataset (left) and Li dataset (right).

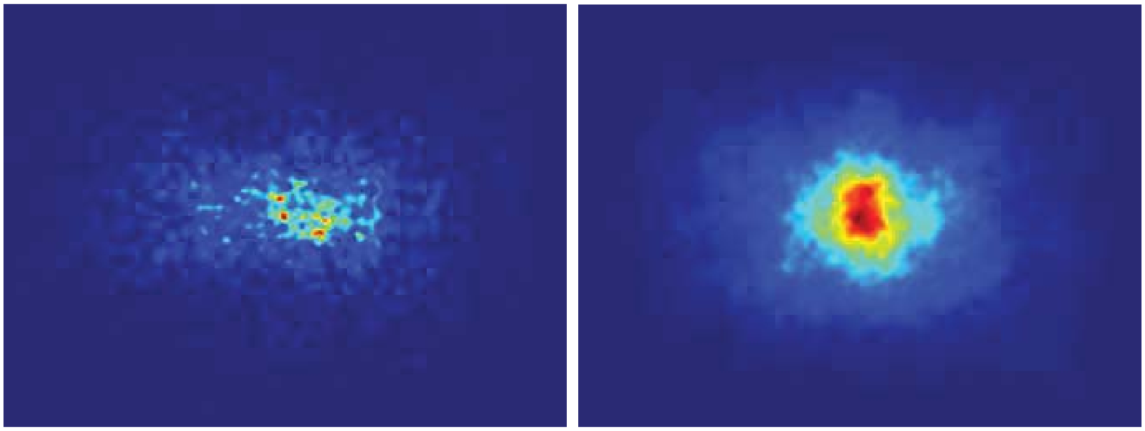

Fig. 2.24. The Gaussian blurred heat map representation of eye fixation of all the images in BT dataset (left) and Li dataset (right), where the Gaussian $\sigma = 0.005$ (in image largest dimension).

3. HAZMAT SIGN DETECTION AND RECOGNITION USING VISUAL SALIENCY

Two typical hazmat signs used for a train tank car and a truck trailer are shown in Figure 3.1. Hazmat signs have identifying visual information that can be distinguished from their surroundings by specific colors, shapes, symbols, and numbers. However, there exist challenges for successful detection and recognition of hazmat signs in complex scenes. Hazmat signs are usually divided into three separate parts by placard holders with two horizontal strips. Various lighting and weather conditions can deteriorate their color and shape over time. Additionally image distortions may occur, such as blur and change in contrast.

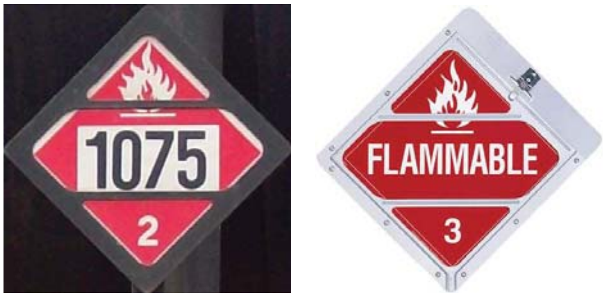

(a) An example of hazmat sign used for a train tank car.

(b) An example of a hazmat sign used for a truck trailer.

Fig. 3.1. Examples of two hazmat signs divided into three separate parts.

In this chapter we describe a hazmat sign location detection and content recognition system using visual saliency. In [14, 15] we reported some preliminary results on this topic. We use saliency maps to denote regions likely containing hazmat signs in complex scenes and use a convex quadrilateral shape detector to find hazmat sign candidates in these regions. Based on our previous work [14, 15], we propose a new approach to hazmat sign location detection using a new visual saliency model proposed in Chapter 2 and a Fourier descriptor based contour matching method [74]. We use the best of our proposed frequency domain models to extract salient regions that are likely to contain hazmat sign candidates and then use a Fourier descriptor based contour matching method to locate the border of hazmat signs in these regions. This visual saliency based approach is able to significantly increase the accuracy of sign location detection, reduce the number of false positive objects, and speed up the overall image analysis process. It uses contour-based shape representation and correlation matching based on the magnitude and phase of the Fourier descriptor of extracted contours. Closed contours are extracted from color channel images using adaptive thresholding, image binarization, morphological operation and connected component analysis. Experimental results show that our proposed hazmat sign location detection method is capable of detecting and recognizing projective distorted, blurred, and shaded hazmat signs in complex scenes.

3.1 Review of Existing Sign Detection and Recognition Methods

3.1.1 Sign Location Detection

Sign location detection approaches can be divided into three categories: color-based methods [75], shape-based methods [76] and vision-based methods [24]. Color-based methods take advantage of the fact that signs often have highly visible contrasting colors. These specific colors are used for sign location detection. For example, a color histogram backprojection method is used in [77] to detect interesting regions possibly containing hazmat signs. In [78] sign location detection is performed using a color-based segmentation method as a preprocessing step for shape detection. The luminance homogeneity of blocks is used in [79] to identify homogenous regions as the first step towards detection of information signs containing text. In [80] several color components are used to segment traffic signs in various weather conditions. However, color-based methods are not robust to lighting conditions and illumination changes.

Shape-based approaches first generate an edge map and then use shape characteristics to find signs. For example, in [81] triangular, square and octagonal road signs are detected by exploiting the properties of symmetry and edge orientations exhibited by equiangular polygons. A shape classification method of a road-sign detection system in [82] is based on linear and Gaussian-kernel support vector machines (SVM). In [83] the authors present a system for detection and recognition of road signs with red boundaries and black symbols inside. Pictograms are extracted from the black regions and then matched against templates in a database. They propose a fuzzy shape detector and a recognition approach that uses template matching to recognize rotated and affine transformed road signs. In [84] the authors propose a system for automatic detection and recognition of traffic signs based on maximally stable extremal regions (MSERs) and a cascade of SVM classifiers trained using histogram of oriented gradient (HOG) features. The system works on images taken from vehicles, operates under a range of weather conditions, runs at an average speed of 20 frames per second, and recognizes all classes of ideogram-based (nontext) traffic symbols from an online road sign database. In most cases shape-based methods are invariant to translation, rotation, and scaling, while in some situations to partial occlusions. Because color-based or shape-based sign location detection methods have both strengths and disadvantages, most color-based approaches take shape into account after using color features while some shape-based detectors also integrate some color aspects.

Vision-based approaches approaches utilize selective visual attention models, which imitate human early visual processing in order to overcome the above problems in complex scenes. Many vision-based traffic sign location detection and analysis methods are using visual saliency models to generate saliency maps that denote areas where signs are likely to be found [24]. For example, in [85] a saliency map of road traffic signs is constructed by a weighted sum of color and edge feature maps. A traffic sign recognition system in [86] uses a visual attention system to denote regions with possible candidates. In our previous work [14, 15] we proposed several image analysis methods using visual saliency for hazmat sign location detection and context recognition. This extended work makes use of our proposed visual saliency models to construct a saliency map as a part of hazmat sign location detection method.

3.1.2 Sign Recognition

Sign recognition methods can be classified into: geometric constraint methods, boosted cascades of features, and statistical moments [24, 79, 87].

Methods based on geometric constraints include the use of Hough-like methods [88, 89], contour fitting [90, 91], or radial symmetry detectors [92, 93]. These approaches apply constraints on the object to be detected, such as little or no affine transformations, uniform contours, or uniform lightning conditions. Although these conditions are usually met, they cannot be generalized. For example, [89] presents an analysis of Hough-like methods and confirms that the detection of signs under real-world conditions is still unstable. A novel Hough-like technique for detecting circular and triangular shapes is also proposed, in order to overcome some of the limitations exposed.

Methods based on the boosted cascades of features commonly use the Viola-Jones framework [94–96]. These approaches often use object detectors with Haar-like wavelets of different shapes, and produce better results when the feature set is large. For example, in [95] a system for detection, tracking, and classification of U.S. speed signs is presented. A classifier similar to the Viola-Jones detector is used to discard objects other than speed signs in a dataset of more than 100,000 images. In [96] the detection is based on a boosted detectors cascade, trained with a version of Adaboost, which allows the use of large feature spaces. The system is robust to noise, affine deformation, partial occlusions, and reduced illumination.

Methods based on statistical moments [97–99] use the central moments of the projections of the object to be detected. They can be used to check the orientation of the object, or to distinguish between different shapes such as circles, squares, triangles, or octagons. These methods are not robust to projective distortions or non-uniform lightning conditions. For example, in [99] a mobile-based sign interpretation system uses detection of shapes with an approximate rotational symmetry, such as squares or equilateral triangles. It is based on comparing the magnitude of the coefficients of the Fourier series of the centralized moments of the Radon transform of the image after segmentation. The experimental results show that the method is not robust to projective distortions.

3.1.3 Shape Descriptors

Shape is an important low level object and image feature [76, 100–102]. Shape can be described using "shape descriptor," which can be generally classified into two methods: contour-based methods and region-based methods [103]. Contour-based methods only exploit the boundary information while region-based methods exploit all the pixels within a region. Contour-based methods are widely used in many applications because of their computational efficiency but they may fail when objects have low resolution. The Fourier descriptors (FD) is a classic and still popular method for contour description [104, 105]. The key idea is to use the Fourier transform of the periodic representation of the contour, which results in a shape descriptor in the frequency domain. The low-frequency components of the descriptor contain information about the general shape of the contour while the finer details are described in the high-frequency components [74]. Although shape descriptors obtained from contour-based methods are not generally robust to noise [106], the Fourier descriptor overcomes noise sensitivity by usually using only the first few low frequency coefficients to describe the shape [74, 103, 107]. The FD is also compact and easy to normalize. In addition, it has been shown that the FD outperforms many other shape descriptors [106, 108].

Existing work on Fourier descriptor (FD) includes methods for generating descriptors invariant to geometric transformations and matching methods for shape similarity and matching. For example, a new Fourier descriptor for image retrieval is proposed in [109] by exploiting the benefits of both the wavelet and Fourier transforms. A complex wavelet transform is first used on the shape boundary and then the Fourier transform of the wavelet coefficients at multiple scales is employed. Since FD is used at multiple scales, the shape retrieval accuracy improves with respect to using ordinary FD. FD feature vectors are analyzed for pedestrian shape representation and recognition [110]. The results show that only ten descriptors of both low and high frequency components of pedestrian and vehicle shapes are enough for accurate shape recognition. The fast FD of some shapes are presented in [111] based on chain codes and the Fourier transform for shape recognition. It is shown that the first ten terms of Fourier coefficients are enough to approximate the shapes. In [74] a method using the Fourier transform of local regions is developed to describe the contours in these regions. A correlation-based contour matching method is also proposed in [74] using both magnitude and phase information of Fourier descriptors for recognizing road signs.

3.2 Review of Existing Hazmat Sign Detection and Recognition Systems

Although there exist several mobile-based applications that provide easy access to the Emergency Response Guidebook (ERG) guidebook [1, 12], they only provide manually browsing functionality. There are a few methods in the literature dealing with sign detection and recognition, but we are only aware of two other published papers with application to hazmat signs [77, 112].

3.2.1 Hazmat Sign Detection Based on SURF and HBP

In [77] the hazmat sign detection is done using color histogram back-projection (HBP) and Speeded Up Robust Feature (SURF) [113] matching. The method was implemented and tested on an autonomous mobile robot for the 2008 RoboCup World Championship. Histogram back-projection is used to detect regions of interest in the image and remove the background of the scene. A background image without a sign,

$h(x, y)$, is used as a ground-truth to isolate the hazmat sign when it appears on the scene and an image of it is captured, $f(x, y)$. This is done by determining the euclidean distance of the color coordinates of each pixel within $h(x, y)$ and the corresponding pixel within $f(x, y)$. A threshold K is used to create a binary mask of the hazmat sign by the use of an indicator function $\delta(x, y) = \{(x, y)\ s.t.\ |f(x, y) - h(x, y)| > K\}$. Several color histograms are then estimated for the U and V channels on the YUV color space, and summed up to create a single histogram $H_o(U, V)$ for every sign on the image. A threshold $\theta(H_o, \epsilon)$ is used for $H_o(U, V)$, resulting in a binary indicator function $\pi_o(U, V)$, which specifies which pixels form part of a sign. The value of ϵ is manually set to 0.05. Finally, morphological filters are used to segment the masked regions from the background and create one or more regions of interest to be used as inputs to the matching process using SURF features.

SURF matching is used to find interest points and retrieve images from a database. After the region of interest is determined from the image containing a hazmat signs, multiple interest points are found using SURF. Interest points surrounding regions that overlap the region of interest are discarded, since the do not provide enough information about the sign. For the remaining interest points, their corresponding feature vectors are matched against all features of all images in a database corresponding to the colors found on the first step.

The experiments were done using a stereo camera system consisting of two cameras with a resolution of 1024 × 768 pixels. The tests consisted of detecting five different hazmat signs in 240 images. The images were taken at 1, 1.5 and 2 meters, with a maximum distortion of 30°. The results show a detection accuracy of 92% from 1 meter, 52% from 1.5 meters, and less than 20% from 2 meters. The running time ranges from 1 to 1.6 second on a 2.7GHz Intel CPU.

3.2.2 Hazmat Sign Detection Based on HOG

In [112] hazmat sign detection using sliding windows and Histogram of Oriented Gradients (HOG) [114] is described. The method was implemented and tested on a wheeled USAR robot for the 2010 RoboCup World Championship.

The authors use the sliding window approach to exhaustively scan every pixel over a range of positions and scales, with steps of 8 pixels and relative scale factors of 1.05. For each position and scale a discriminative Support Vector Machine (SVM) classifier is used to make binary decisions about the presence or absence of an object. In order to describe the contents of the image at each particular location a HOG descriptor is used along with color histograms in the Lab color space to distinguish between multiple hazmat signs. For each hazmat sign hypothesis of the HOG based detector, the color histogram is used to do the final classification by applying a k-nearest neighbor approach in combination with χ^2-distance.

The experimental results show a recognition rate of 37.5% using histograms based on entire sliding windows and a recognition rate of 58.3% using sub-region based histograms. Region-based histograms provide better representation of the image since they are capable of capturing the spatial distribution of colors within the detection window.

3.2.3 Comparison to MERGE

We proposed a hazmat sign location detection and content recognition system, known as MERGE (Mobile Emergency Response GuidE) [13]. Although all methods above are deployed on mobile environments, MERGE is intended for real-time use by first responders, while [77] and [112] were intended for use in a very specific context. The sign detection method proposed in [77] uses a ground-truth image of the background to aid in detection when the hazmat sign appears. This is not a feasible assumption in MERGE, since the first responders are expected to take images of hazmat signs in a large variety of scenarios. In [112] a dataset of 1480 daylight images is used for both people and hazmat sign recognition. However, the authors do not specify how many images contain hazmat signs, or at what distances the signs are located. They do not provide information about the resolution of the images or the cameras used for acquisition. In MERGE no assumptions on the background are made in order to detect the sign. Instead, color information is used to detect candidate regions using a saliency map model.

Once the hazmat sign is detected [77] uses image matching based on SURF features, and [112] uses HOG and color histogram descriptors, both being very time consuming task. This step is not done in MERGE. Currently, the color of the hazmat sign is considered to be uniform, and the detection is made at different color channels. The recognition of non-uniformly-colored placards is presented as part of the future work.

The goal of MERGE is to be able to detect hazmat signs at long distances. Our experimental results show successfully detecting hazmat signs in some cases at more than 100 feet. However, the experiments in [77] can only be considered successful at 1.5 meters, and the accuracy reported by [112] is very low. Finally, the execution time of the overall process of our hazmat sign image analysis system MERGE is several seconds, comparable with the hazmat sign image analysis system in [77]. No execution time is reported in [112].

3.3 Proposed Hazmat Sign Detection and Recognition System

3.3.1 MERGE System Overview[1]

Figure 3.2 shows the overview of our proposed hazmat sign location detection and content recognition system, known as MERGE (Mobile Emergency Response GuidE) [13]. It consists of an application running on an Android/iOS mobile device[2] and a backend server where many image analysis operations are done [14, 15]. There are two basic operational modes of our MERGE system: analysis of hazmat sign images and searching internal database. The first mode includes capturing or selecting an hazmat sign image from the mobile device and performing image analysis on the backend server. Hazmat sign detection and recognition are done on the backend server and the results are sent back to the mobile device [14, 15]. The second mode includes searching the internal database to obtain guide information about a specific hazmat sign. We designed an internal database based on the contents of the 2012 ERG guidebook. As shown in Figure 3.3, hazmat signs can be manually searched by UN identifier numbers, template images, symbols, and classes.

Figure 3.4 shows the operational workflow and user interface at each step. The image analysis results are used for matching related guide pages and querying internal database to retrieve guide information. We display guide information about potential hazards, public safety and emergency response. All the information is from the internal database on the mobile application. A suggested evacuation region is also displayed on a map based on the chemical found, the size of the chemical spill, the time of the day, and a weather-aware chemical spreading webservice.

[1] The work in this section was developed by the author jointly with my colleagues Albert Parra and Joonsoo Kim.

[2] The Android application was developed by my colleague Albert Parra and the iOS application was developed by my colleague Joonsoo Kim.

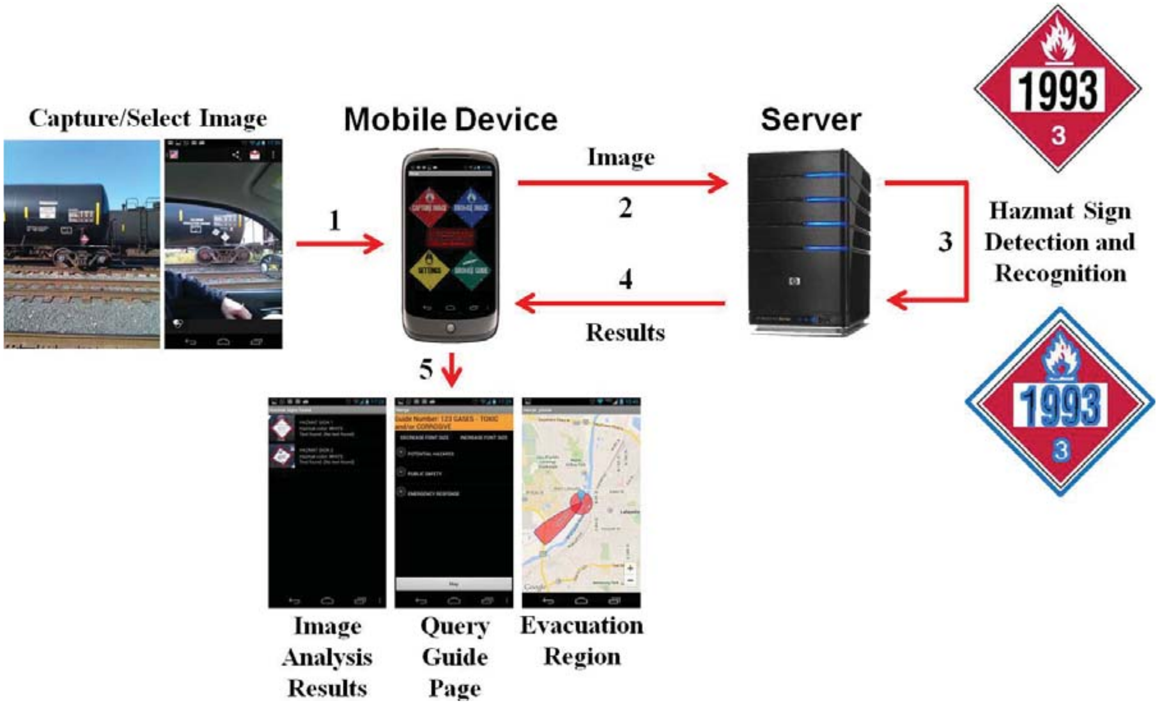

Fig. 3.2. Hazmat sign location detection and content recognition system.

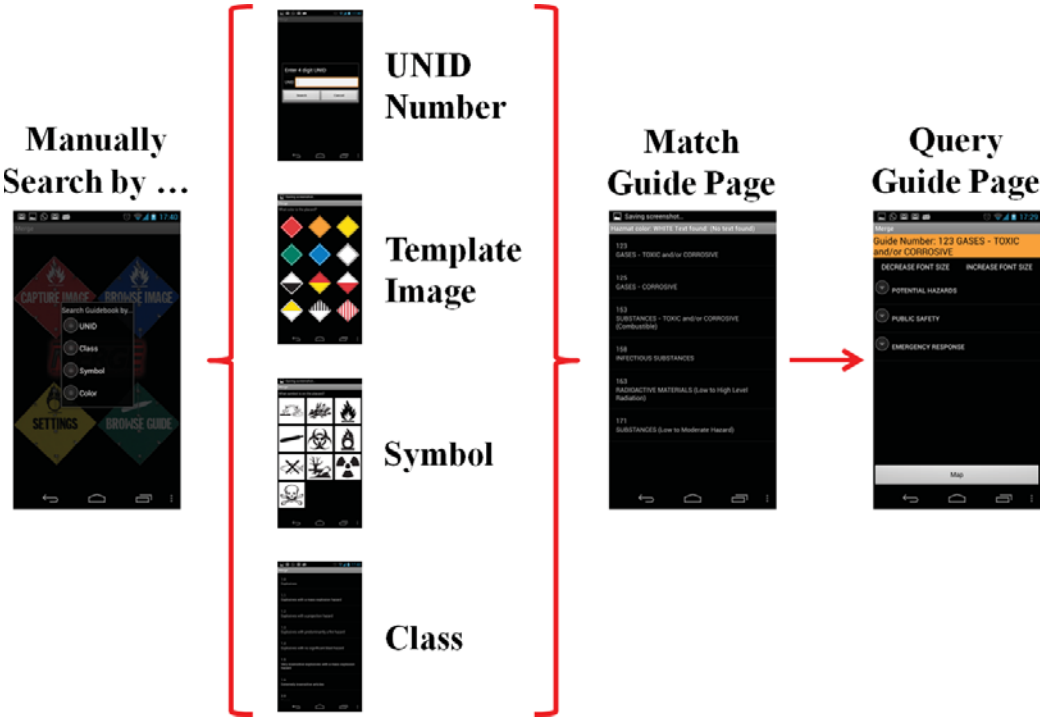

Fig. 3.3. Manually search hazmat signs by UN identifier numbers, template images, symbols, and classes.

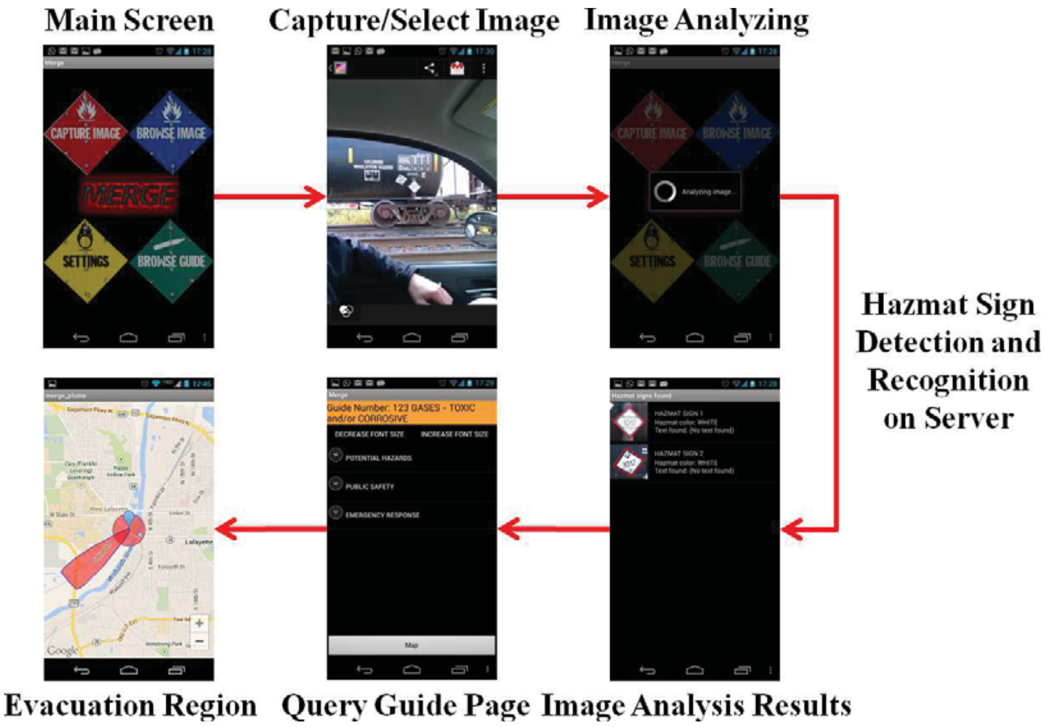

Guide Number: 123 GASES - TOXIC and/or CORROSIVE

HAZMAT SIGN 1
Hazmat color: WHITE
Text found: (No text found)

HAZMAT SIGN 2
Hazmat color: WHITE
Text found: (No text found)

Fig. 3.4. Mobile application user interface at each step.

3.4 Hazmat Sign Detection and Recognition Method 1

We use visual saliency based methods and generate saliency maps using color spaces. Spatial domain visual saliency models usually have high computational cost and variant parameters for multiple feature maps, which make them impractical to meet our needs. Frequency domain visual saliency models with fast computation with high prediction accuracy could be suitable for our application. Our proposed hazmat sign detection and recognition method is based on visual saliency. We use two existing visual saliency models to generate saliency maps denoting salient regions likely containing hazmat signs in complex scenes and develop a convex quadrilateral shape detection method to extract the border of hazmat signs in these regions. The block diagram in Figure 3.5 shows the building blocks of the proposed hazmat sign detection and recognition method 1.

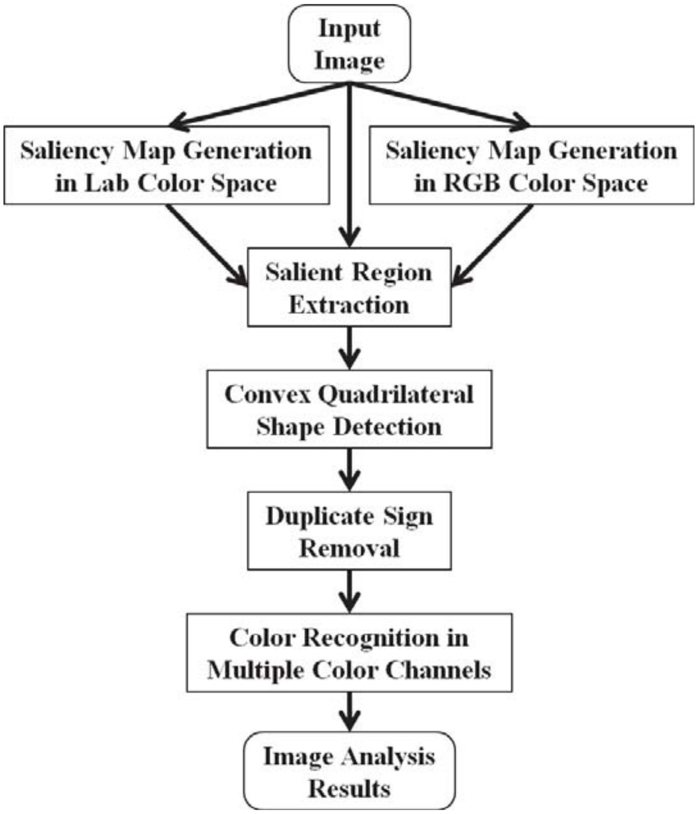
Input Image
Saliency Map Generation in Lab Color Space
Saliency Map Generation in RGB Color Space
Salient Region Extraction
Convex Quadrilateral Shape Detection
Duplicate Sign Removal
Color Recognition in Multiple Color Channels
Image Analysis Results

Fig. 3.5. Proposed hazmat sign detection and recognition method 1.

3.4.1 Saliency Map Generation

We use two existing visual saliency models to generate saliency maps from images represented in both Lab and RGB color spaces, because we observed that color signs have strong visual responses in Lab color space while white signs have strong visual responses in RGB color space from our experiments. In each color space, two saliency maps are generated separately using two visual saliency models, *i.e.* IS model [33] and SSA model [35] respectively. The saliency maps assign higher saliency value (ranging from lowest 0 to highest 1) to more visually attractive regions that are likely containing hazmat signs in complex scenes. Note that the original SSA method uses the IRGBY color space [35]. We modified this method to use Lab and RGB color components with different weights ($[\frac{1}{2}, \frac{1}{4}, \frac{1}{4}]$ for Lab and $[\frac{1}{3}, \frac{1}{3}, \frac{1}{3}]$ for RGB). The proposed hazmat sign detection method using the four saliency maps (two from Lab and two from RGB), denoted as the combined method IS+SSA(Lab+RGB), has good performance in the experiments. (see Section 3.6)

3.4.2 Salient Region Extraction

We threshold each saliency map to create a binary mask to extract the salient regions from the original image. The threshold T_1 is determined as k times the average saliency value of a given saliency map.

$$T_1 = \frac{k}{W \times H} \sum_{x=1}^{W} \sum_{y=1}^{H} S(x, y), \tag{3.1}$$

where W and H are the width and height of the saliency map, $S(x, y)$ is the saliency value at position (x, y) and k is empirically determined for the combined detection method IS+SSA(Lab+RGB), *i.e.* $k = 4.5$ for IS models and $k = 3.5$ for SSA models, which provides a good trade-off between hazmat sign coverage and computational cost of extracted salient regions in the experiments. (see Section 3.6) The following processing can take advantages of local distinctive features in the extracted salient regions instead of the entire input image.

3.4.3 Convex Quadrilateral Shape Detection[3]

For each salient region found, we detect hazmat sign candidates in specific color channels. We used black and white information from grayscale image, and red, green and blue channels from RGB color space. Note that the possible colors for hazmat signs also include yellow and orange, but these can be obtained by transforming the image from RGB to a hue-based color space and then segment the hue channel. The grayscale image and the color channels are thresholded to account for highly chromatic areas using an empirically determined threshold T_2 (85 for black, 170 for white, and 127 for color). Each binarized region is morphologically opened to remove small objects and morphologically dilated to merge areas that may belong to the same object. We then retrieve contours from the resulting binary image using the border following technique proposed in [115]. For each contour, we use the Hough Transform [116] to find straight lines that approximate the contour as a polygon. The intersections of these lines are the corners of the polygon which can be used to discard non-quadrilateral shapes. If the contour is approximated by four vertices, we find its convex hull [117]. If the convex hull still has four vertices, we check the angles formed by the intersection of its points. If each of these angles is in the range $90° \pm 1.5°$, and the ratio of the sides formed by the convex hull is in the range 1 ± 0.5, we assume that the convex quadrilateral is a hazmat sign candidate.

3.4.4 Duplicate Sign Removal

To remove duplicate sign candidates from different color channel images, we first check all candidates passed the contour matching and estimate their minimal bounding boxes. Any disqualified candidate with the aspect ratio of its bounding box

[3] The work in this section was developed by the author jointly with my colleague Albert Parra.

greater than 1.3 will be discarded. We then remove the duplicate sign candidates that correspond to the same sign. This can be done by first dividing all candidates that are overlapped more than 50% into multiple groups and then finding the optimal diamond-shaped box for each group, whose four nodes are closest to the centroid of its group. Each optimal diamond-shaped box is considered to be the location of a detected hazmat sign.

3.4.5 Color Recognition[4]

Because signs are detected in specific color channels, the color is recognized directly from the color channel where the sign was identified (black or white for grayscale and red, green or blue for RGB). The recognized color is used for queuing the mobile database for sign category identification and providing the general guide information based on the 2012 ERG guidebook. Figure 3.6(a) illustrates a successful detection of two signs using the previous Method 1, one of which is affected by projective and rotational distortion. Figure 3.6(b) illustrates a true positive and a false positive from the previous Method 1.

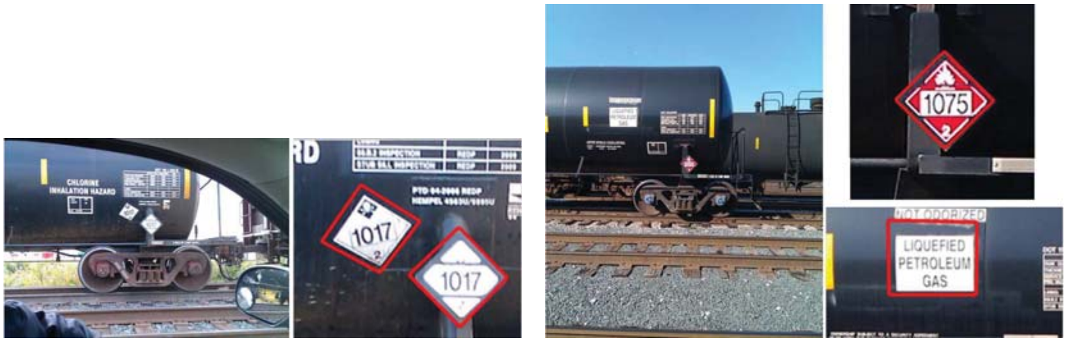

(a) Two true positives.

(b) One true positive and one false positive.

Fig. 3.6. Examples of image analysis.

[4] The work in this section was developed by the author jointly with my colleague Albert Parra.

3.5 Hazmat Sign Detection and Recognition Method 2

We use our proposed frequency domain models in Chapter 2 to extract salient regions that are likely to contain hazmat sign candidates and develop a Fourier descriptor based contour matching method to extract the border of hazmat signs in these regions. Based on our previous work [14], we propose a new approach to hazmat sign location detection using a Fourier descriptor based contour matching method [74]. It uses contour-based shape representation and correlation matching based on the magnitude and phase of the Fourier descriptor of extracted contours. The existing method used to detect road signs in [74] cannot be directly used for hazmat sign location detection. Hazmat signs mounted on vehicles are usually enclosed in a placard holders with two horizontal strips that divide a hazmat sign into three separate parts as shown in Figure 3.1. In our case we need to use morphological operations to merge separate parts that belong to a whole hazmat sign and then employ connected component analysis to determine the boundary of the whole hazmat sign. Closed contours are extracted from color channel images using adaptive thresholding, image binarization, morphological operation and connected component analysis.

Fourier Descriptor (FD) is used to describe the shape of the extracted contours through the Fourier transform [104, 105]. It has been proven to be a state-of-the-art contour-based sign detection methods in terms of accuracy and tolerance of rotated, scaled, and noisy signs [74, 105, 110]. In order to determine if an extracted contour correspond to a hazmat sign, we need to compare its FD against the FD of the contour of a shape template or a predefined shape contour. In our case, the shape template of hazmat signs is represented by a diamond shaped binary image as shown in Figure 3.7.

Contour matching can be done in the spatial or frequency domain. We use matching in the frequency domain for two reasons. First, matching in the frequency domain is scale independent, as opposed to spatial domain matching. Second, matching in the spatial domain involves scanning an image multiple times modifying the scale

Fig. 3.7. A diamond shaped binary image represents the shape template of a hazmat sign.

and rotation of the shape template. Frequency domain matching methods have been shown to be more computationally efficient when working with images of high resolution [118, 119]. FD-based matching is usually done by using only the magnitude and ignoring the phase information. By discarding the phase information, rotation and starting point invariance can be achieved [120]. However, because variant shapes can have similar magnitude but different phase information, this makes FD-based magnitude-only matching less accurate [74]. A correlation-based contour matching method is proposed in [74] using both magnitude and phase information of Fourier descriptors for recognizing road signs. It is shown that the normalized FDs are invariant to scaling and the correlation-based contour matching using both magnitude and phase information is invariant to rotation and starting point. We use this frequency domain contour matching method [74] to detect the location of hazmat signs based on a diamond shaped template. The block diagram in Figure 3.8 shows the building blocks of the proposed hazmat sign detection and recognition method 2.

3.5.1 Saliency Map Generation

We use our proposed frequency domain models to generate saliency maps from input images represented in both Lab and RGB color spaces, because we observed that color signs have strong visual responses in Lab color space while white signs have strong visual responses in RGB color space from our experiments. In each color

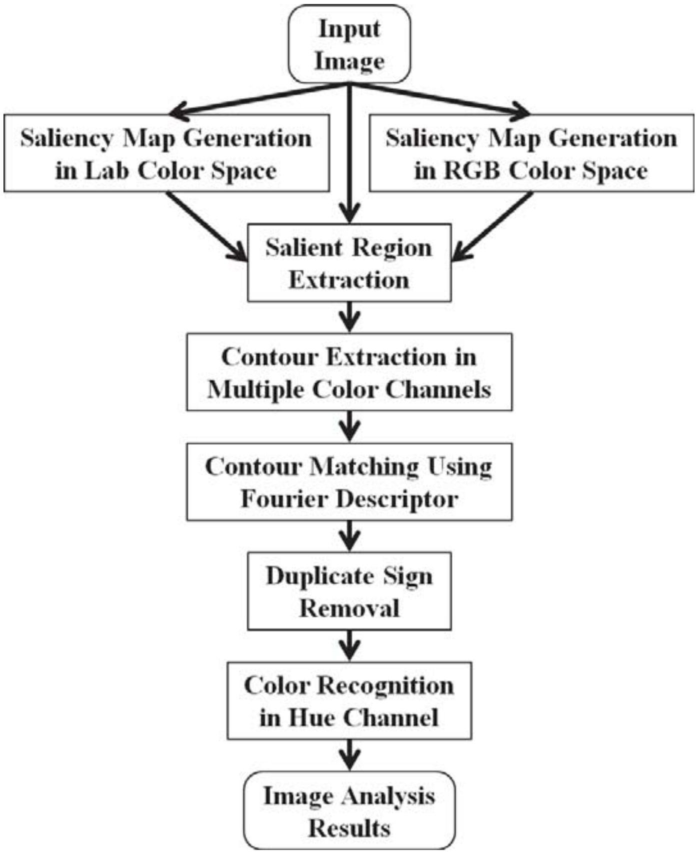
Input Image
Saliency Map Generation in Lab Color Space
Saliency Map Generation in RGB Color Space
Salient Region Extraction
Contour Extraction in Multiple Color Channels
Contour Matching Using Fourier Descriptor
Duplicate Sign Removal
Color Recognition in Hue Channel
Image Analysis Results

Fig. 3.8. Proposed hazmat sign detection and recognition method 2.

space, a saliency map is generated separately using the proposed Gamma Corrected Spectrum (GCS) visual saliency model, *i.e.* either GCS-FT-Lab model or GCS-FT-RGB model. (see Section 2.3.4) Two saliency maps, one from Lab color space and the other from RGB color space, assign higher saliency value (ranging from lowest 0 to highest 1) to more visually attractive regions that are likely containing hazmat signs in complex scenes. The proposed hazmat sign detection method using the two saliency maps, denoted as the combined method GCS(Lab+RGB), has the best performance in our experiments. (see Section 3.6)

3.5.2 Salient Region Extraction

We threshold each saliency map to create a binary mask to extract the salient regions from the original image. The threshold T_1 is determined as k times the average saliency value of a given saliency map.

$$T_1 = \frac{k}{W \times H} \sum_{x=1}^{W} \sum_{y=1}^{H} S(x, y), \tag{3.2}$$

where W and H are the width and height of the saliency map, $S(x, y)$ is the saliency value at position (x, y) and k is empirically determined for the combined detection method GCS(Lab+RGB), *i.e.* $k = 2.0$ for GCS-FT-Lab model and $k = 2.0$ for GCS-FT-RGB model, which provides a good trade-off between hazmat sign coverage and computational cost in extracted salient regions in our experiments. (see Section 3.6) The following processing can take advantages of local distinctive features in the extracted salient regions instead of the entire input image.

3.5.3 Contour Extraction

The hazmat signs in our dataset contain either one or two of the following colors: white, red, green, blue, and yellow. In order to obtain strong visual responses of certain colors of hazmat signs, we transform an extracted salient region of the input image into several channel images in different color spaces. The white signs can be detected in the grayscale channel image. The red, green and blue signs can be detected in R, G, B channel images from the RGB color space. The yellow signs can be detected in the Y channel image from the CMYK color space. We process each channel image of the extracted salient region separately in the following.

In order to binarize each channel image of the salient region A_k^{SR}, we propose a new adaptive thresholding method that is a modification of Otsu's thresholding method [121]. Since images containing hazmat signs are likely acquired with various lighting conditions, directly using Otsu's thresholding method on the channel image does not produce accurate results when images contain variable illumination [122]. For each channel image, I_i, $i \in [1, 5]$, we first use a histogram of 256 bins for the [0,255] grayscale values to characterize pixel distribution and then obtain the median of the pixel counts of all bins N_i^{MED}. Second, we find the starting location of two significant peaks T_i^L and T_i^H at the low and high ends of the histogram by checking the change of pixel counts between two adjoining bins. The two index thresholds T_i^L and T_i^H are selected to clip the histogram.

$$\begin{aligned} N_i^{MED} &= median\left(\mathcal{N}(B_i^j)\right), && (3.3)\\ T_i^L &= argmin_j\left(|\mathcal{N}(B_i^j) - \mathcal{N}(B_i^j - 1)| > F_B \cdot N_i^{MED}\right), j \in [3, 128], && (3.4)\\ T_i^H &= argmax_j\left(|\mathcal{N}(B_i^j) - \mathcal{N}(B_i^j + 1)| > F_B \cdot N_i^{MED}\right), j \in [129, 254], && (3.5) \end{aligned}$$

where $\mathcal{N}(B_i^j)$ is the pixel count of the j-th bin in the histogram of the i-th channel image, $F_B = 0.05$ is a factor to determine index thresholds T_i^L and T_i^H with respect to N_i^{MED} (empirically obtained by searching good values in our experiments), T_i^L is the starting location of the low-end significant peak (the index threshold of a low-end bin), and T_i^H is the starting location of the high-end significant peak (the index threshold of a high-end bin). For each color channel image, we modify its histogram by clipping the pixel counts $\mathcal{N}(B_i^j)$ of the low-end and high-end bins into 0s based on the two index thresholds T_i^L and T_i^H.

$$\mathcal{N}'(B_i^j) = \begin{cases} 0 & B_i^j \le T_i^L \text{ or } B_i^j \ge T_i^H \\ \mathcal{N}(B_i^j) & \text{otherwise} \end{cases} \tag{3.6}$$

The modified histogram with new pixel counts $\mathcal{N}'(B_i^j)$ for all 256 bins is used with the original Otsu's method [121] to generate an adaptive threshold T_i^{BW}. Finally, each original channel image I_i is then binarized using T_i^{BW}. Figure 3.9 illustrates an example of image binarization using the proposed adaptive thresholding method comparing with using Ostu's method for a red channel image of an extracted salient region. Note that our proposed adaptive thresholding method is capable of adapting to local histogram and intensity features in the extracted salient regions instead of the entire image. The original Otsu's method fails to find a good threshold because of a large number of pixels in other regions also having high intensity values in the red channel of the entire image.

As we mentioned before, morphological operations are used to extract the whole area of the hazmat sign from the binarized channel images. First, we use a flood-fill operation to fill holes [123] in the binarized channel images of an extracted salient region A_k^{SR}. A hole is a set of background pixels surrounded by foreground pixels. We use this operation to fill up missing pixels of UN identifier numbers and symbols that are removed due to different colors. Next, we use morphological dilation with a SE_D-pixel diamond shaped structuring element to enlarge the boundaries of foreground areas [123, 124], where SE_D is the size of the diamond shaped structuring element (pixel distance from the origin to the vertex). The shape of the structuring element we used is same diamond as hazmat sign. We use this dilation to merge three separate parts of a whole hazmat sign that divided by the placard holders with two horizontal strips.

$$SE_D = min\left(7, F_{SE} \cdot \mathcal{N}(A_k^{SR})\right), \tag{3.7}$$

where $\mathcal{N}(A_k^{SR})$ is the total number of pixels in the salient region A_k^{SR} and $F_{SE} = 0.0025\%$ is a factor to determine the size of the diamond shaped structuring element SE_D with respect to the percentage of the total number of pixels in A_k^{SR}, which is empirically determined by searching good values in our experiments.

We use connected component analysis to determine the boundary of the entire hazmat sign in the binarized channel images. We remove small connected components containing less than $T_{CC} = 200$ pixels, which is less than the minimum number of pixels on a hazmat sign in our image datasets. Finally, we obtain closed contours by tracing the exterior boundaries of the connected components [124, 125] in each binarized channel image separately. Table 3.1 lists all the thresholds and parameters we used including empirically obtained ones.

Table 3.1
Thresholds and parameters used in our proposed method. Automatically determined ones are denoted by *.

Symbol	Description	Value
N_i^{MED}	Median of the pixel counts of all bins	*
T_i^L	Low index threshold to clip the histogram	*
T_i^H	High index threshold to clip the histogram	*
T_i^{BW}	Adaptive threshold to binarize channel images	*
SE_D	Size of the diamond shaped structuring element	*
F_B	Factor to determine index thresholds T_i^L and T_i^H	0.05
F_{SE}	Factor to determine the size of the structuring element SE_D	0.0025%
T_{CC}	Threshold to remove small connected components	200
T_e	Threshold for correlation-based matching cost e	1.751

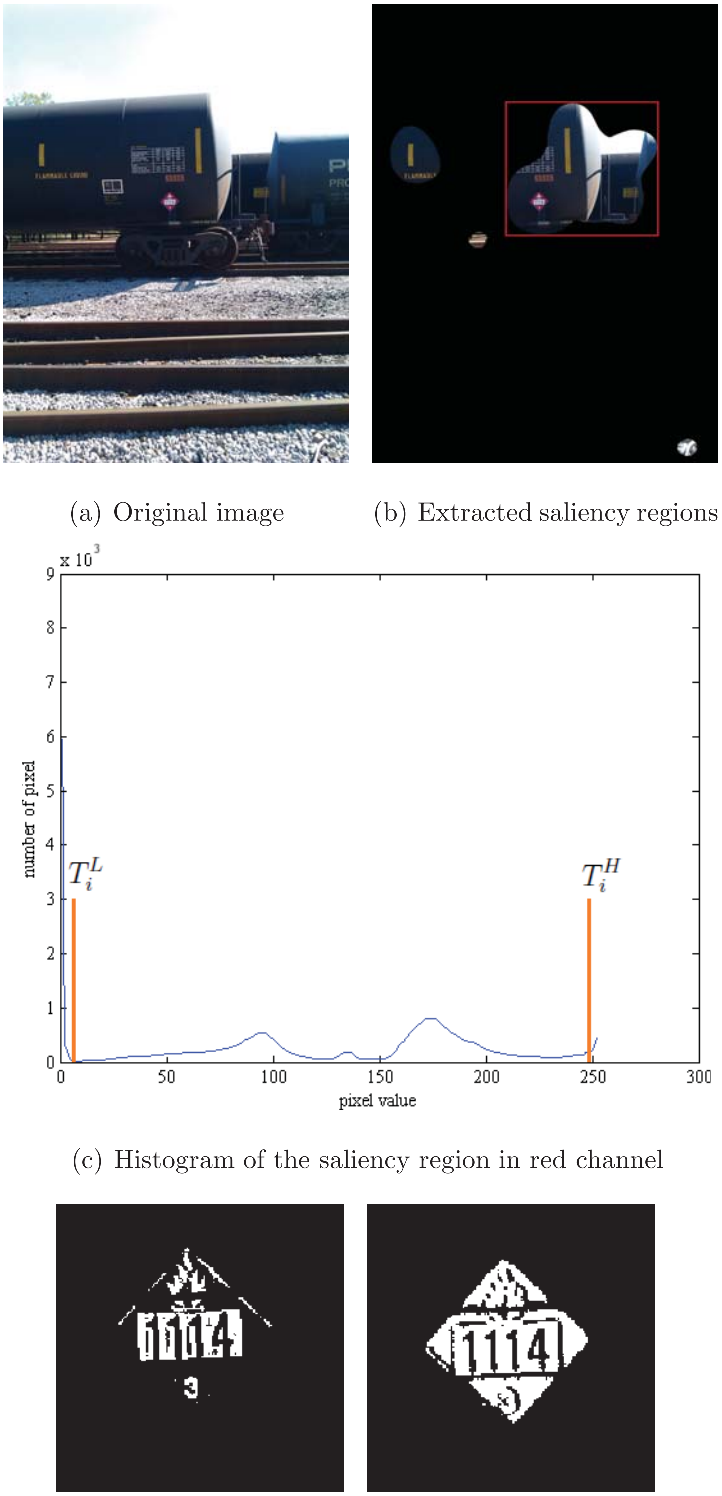

(a) Original image (b) Extracted saliency regions

(c) Histogram of the saliency region in red channel

(d) Otsu's method (e) Proposed method

Fig. 3.9. Example of image binarization using the proposed adaptive thresholding method comparing with using Ostu's method.

3.5.4 Fourier Descriptor Generation

The Fourier Descriptor (FD) describes the shape of an object using a set of the Fourier transform coefficients of the object's contour [104, 105]. Given the extracted contour $c(k)$ has N pixels, numbered from 0 to $N-1$, a set of pixel coordinates describing the contour $c(k)$ can be defined as follows.

$$c(k) = (x(k), y(k)) = x(k) + iy(k), \tag{3.8}$$

where $k = 0, 1, 2, \ldots, N-1$. The Fourier transform of the contour points $c(k)$ generates a set of complex numbers $C(v)$ which are the Fourier descriptors of the contour.

$$C(v) = \mathcal{F}(c(k)) = \frac{1}{N}\sum_{k=0}^{N-1} c(k)exp\left(-\frac{i2\pi vk}{N}\right), \tag{3.9}$$

where $v = 0, 1, 2, \ldots, N-1$. In order to describe the shape of a closed contour generally, the Fourier descriptor have to be modified to make it invariant to translation and scaling [74,109–111]. To achieve translation invariance, the DC Fourier coefficient $C(0)$ is set to zero $C(0) = 0$. All points on the contour are then shifted from its original coordinate to $(0, 0)$. The closed contour represented by the remaining Alternating Current (AC) Fourier coefficients is invariant against translation, but it's still affected by scaling due to the magnitude of each AC coefficient. To achieve scaling invariance, the remaining AC Fourier coefficients $C(v)$ are normalized by $\sqrt{\sum_{v=1}^{N-1}|C(v)|^2}$. The modified Fourier descriptor $C'(v)$ of the extracted contour $c(k)$ are obtained as follows.

$$C'(v) = \begin{cases} 0, & \text{if } v = 0, \\ \frac{C(v)}{\sqrt{\sum_{v=1}^{N-1}|C(v)|^2}}, & \text{if } v \neq 0, \end{cases} \tag{3.10}$$

where $C(v)$ is the original Fourier coefficients. The low frequency components of Fourier descriptors $C'(v)$ contain information about the general shape of the contour while the high frequency components contain finer details. Therefore, the first P

modified AC Fourier descriptors can be used to create an approximate reconstruction $\widehat{b}(k)$ of the original contour points $c(k)$ for contour matching.

$$\widehat{c}(k) = \frac{1}{P} \sum_{v=0}^{P} C'(v) exp \left(\frac{i2\pi vk}{N} \right), \tag{3.11}$$

where $k = 0, 1, 2, \ldots, N-1$.

3.5.5 Correlation-Based Contour Matching[5]

We use the correlation-based contour matching method [74] to locate the border of hazmat signs based on a diamond shaped template. To achieve the rotation and starting point invariance, the correlation-based contour matching using both magnitude and phase information is required for hazmat sign location detection. The modified Fourier descriptors of extracted contours and the template contour can been obtained in previous steps and their magnitude and phase information is used to compute cross-correlation by employing complex conjugate multiplication $\overline{X}Y$. This correlation-based contour matching method is able to achieve translation, scaling, rotation and starting point variances. The cross-correlation $r_{TE}(l)$ between an extracted contour c_E and the template contour c_T is defined as follows.

$$\begin{aligned} r_{TE}(l) &= \int_0^K \overline{c_T(k)} c_E(l+k) \mathrm{d}k \\ &= \sum_{v=0}^{N-1} \overline{C'_T(v)} C'_E(v) exp \left(-\frac{i2\pi vl}{K} \right) \qquad (3.12) \\ &= \mathcal{F}^{-1}\{\overline{C'_T} C'_E\}(v). \qquad (3.13) \end{aligned}$$

By using the first P modified Alternating Current (AC) Fourier descriptors with both magnitude and phase information, this simplified contour matching method is

[5] The work in this section was developed by the author jointly with my colleague Kharittha Thongkor.

able to approximately achieve translation, scaling, rotation and starting point variances. We say “approximately” because we are only using the first few modified Fourier descriptors to describe the shape of the closed contour. In order to determine the appropriate number P of modified AC Fourier descriptors needed for contour matching, we examined the shape variations from a group of reconstructed contours of the template diamond-shaped contour by varying the number of modified AC Fourier descriptors we used. Figure 3.10 illustrates the shape variations of using the first 4, 8, 16, 32, 50 and 100 modified AC Fourier descriptors to reconstruct the template contour of diamond shape. It is shown that using the first 8 modified AC Fourier descriptors is a good approximation of the contour of the diamond shaped template. Using more Fourier descriptors than necessary leads to increasing computational cost with limited additional benefit [106]. Because using more modified AC Fourier descriptors does not significantly improve the matching performance, we only use the first 8 AC Fourier descriptors in our experiments.

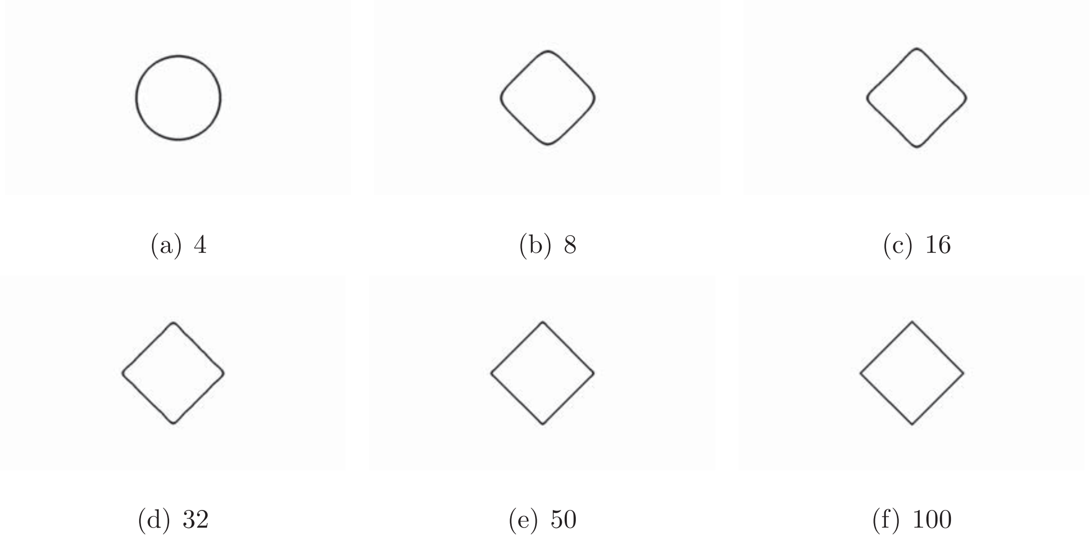

(a) 4

(b) 8

(c) 16

(d) 32

(e) 50

(f) 100

Fig. 3.10. The the shape variations of using the first 4, 8, 16, 32, 50 and 100 AC Fourier coefficients.

The modified Fourier descriptors of all the contours are used to match against the ones of the template contour of hazmat signs in Figure 3.7. To decide if an extracted contour c_E is a good match of a hazmat sign, we check the results of a correlation-based matching cost function. The matching cost e is based on the cross-correlation $r_{TE}(l)$ of two modified Fourier descriptors between an extracted contour c_E and the template contour c_T.

$$e = 2 - 2 \max_{l} |r_{TE}(l)|, \tag{3.14}$$

where $r_{TE}(l)$ is the cross-correlation between an extracted contour c_E and the template contour c_T. If the matching cost e is lower than an empirically obtained threshold T_e, we accept the extracted contour c_E as the border of a hazmat sign that represents the location of that sign in the input image. If the matching cost e is higher than the threshold T_e, we reject the extracted contour c_E and do nothing in the following. In order to determine the threshold T_e, we calculate the correlation-based matching cost e between the contours of some shapes shown in Figure 3.11 and the contour of the diamond shaped template in Figure 3.7. Because the cost of matching a general diamond shape (including the rotation as a square shape) against the diamond shaped template is not greater than 1.750, we then set $T_e = 1.751$. Note that the contours of other shapes in Figure 3.11 are only used to determine the threshold T_e. We keep updating a list of borders representing the sign locations till all the extracted contours in all saliency regions are matched against the template contour. We then obtain the cropped hazmat sign images using the accepted contours in the border list to crop the pixels of hazmat signs from the original image.

3.5.6 Duplicate Sign Removal

To remove duplicate sign candidates from different channel images, we first check all candidates passed the contour matching and estimate their minimal bounding boxes. Any disqualified candidate with the aspect ratio of its bounding box greater than 1.25 will be discarded. We then remove the duplicate sign candidates that correspond to the same sign. This can be done by first dividing all candidates that

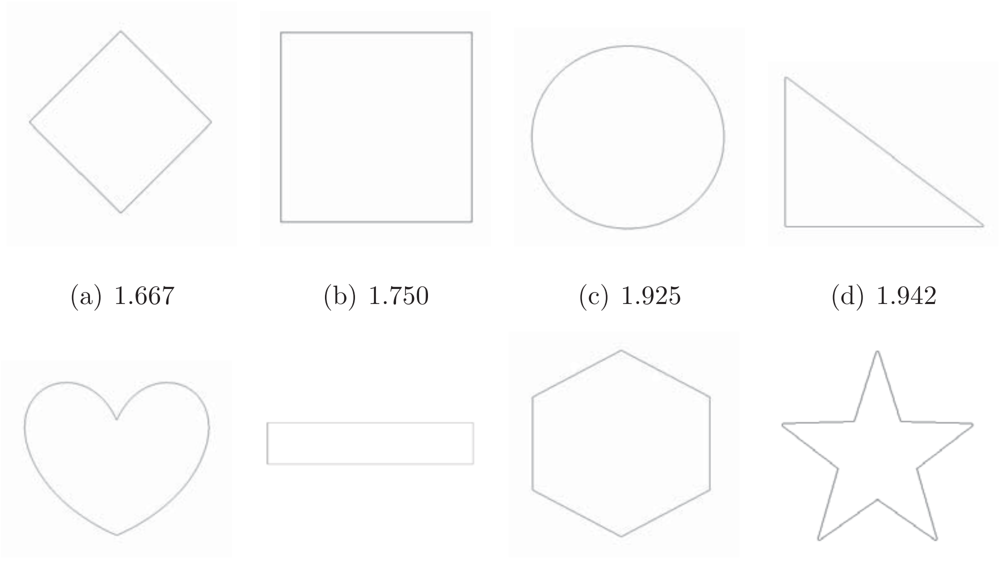

(a) 1.667 (b) 1.750 (c) 1.925 (d) 1.942

(e) 1.953 (f) 1.961 (g) 1.973 (h) 1.974

Fig. 3.11. Comparison of the contours of some shapes and their matching costs *e*.

are overlapped more than 75% into multiple groups and then finding the optimal diamond-shaped box for each group, whose four nodes are closest to the centroid of its group. Each optimal diamond-shaped box is considered to be the location of a detected hazmat sign.

3.5.7 Color Recognition

The HSV color space (Hue, Saturation, Value) is often used for recognizing colors in the Hue (H) channel similar to a color wheel. As Hue (H) varies from 0 to 1, the corresponding colors vary from red through yellow, green, cyan, blue, magenta, and back to red (there are actually red colors both at 0 and 1). As Saturation (S) varies from 0 to 1, the corresponding colors (hues) vary from unsaturated (shades of gray) to fully saturated (no white component). Saturation can be considered as the purity of a color. As Value (V), roughly equivalent to brightness, varies from 0 to 1, the corresponding colors become increasingly brighter. The brightest areas of the value channel correspond to the brightest colors in the original image. Figure 3.12 illustrates the Hue, Saturation, Value of the HSV color space.

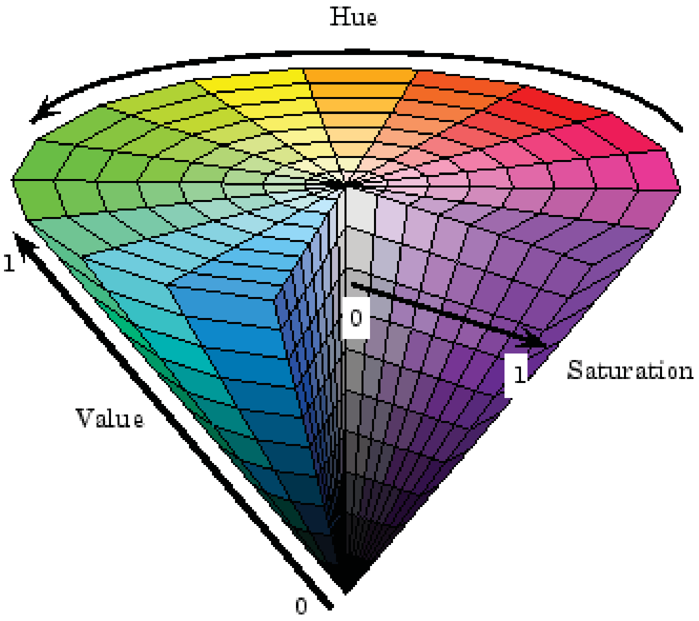

Fig. 3.12. Hazmat sign detection and recognition system.

The color of a hazmat sign can be recognized in HSV color space. We convert a cropped hazmat sign image from RGB to HSV color space and extract the three channel images separately. The white hazmat sign can be first determined from the Saturation (S) and Value (V) channel images of the cropped image. Then other

Table 3.2
The color look-up table based on the 32 uniform distributed hue segments.

Recognized Colors	Red(1)	Orange	Yellow	Green	Blue	Red(2)
Hue Segment Range	0∼0.03125	0.03125∼0.09375	0.09375∼0.25	0.25∼0.5	0.5∼0.75	0.75∼1
Hue Segment Indexes	1	2,3	4∼8	9∼16	17∼24	25∼32

colorful hazmat sign can be recognized from the masked regions of the Hue (H) channel image of the cropped image. This can be done by an image masking method using image thresholding on saturation and value channel images because white's saturation is close to 0 and its value is close to 1. We compute the histograms of the saturation and value channel images of the cropped image and then employ the Otsu's thresholding method [121] to binarize the channel images and obtain two masks of resultant regions whose saturation and value are greater than their thresholds. A combined mask is obtained by AND operations of saturation and value masks and it denotes the mask of color regions in the cropped image since the Saturation (S) and Value (V) channels are both orthogonal to the Hue (H) channel. The masked color regions is used to check if the hazmat sign is white or other color. A hazmat sign is considered as white if the size of the masked color regions is less than 0.4% of the number of pixels in the cropped image, otherwise it is considered as other color in the following.

To determine the color (except white) of the masked color regions, we first define a set of K uniform distributed hue segments by equally dividing the whole range of the hue channel (from 0 to 1). A histogram of K bins of the hue segments is used to characterize the hue distribution of the cropped hazmat sign image. We find the index B_k of the maximum number of pixel counts in the histogram and use it to determine the color (except white) of the hazmat sign by searching B_k in an empirically obtained color look-up table in Table 3.2 based on the K bins of the hue segments. The size of look-up table is determined by the number of hue segments K and we use $K = 32$ in our color recognition method. Some examples of the proposed color recognition method for white and colorful hazmat signs at 50 feet are illustrated from Figure 3.13 to Figure 3.16 respectively (The hazmat sign images with 4-digit UNID were captured by 5 MP camera on an HTC Wildfire mobile telephone (2592×1952) and the ones with warning text were captured by a 5 MP camera on a Samsung Galaxy Nexus mobile telephone (2592×1944)). The recognized color is used for queuing the mobile database for sign category identification and providing the general guide information based on the 2012 ERG guidebook.

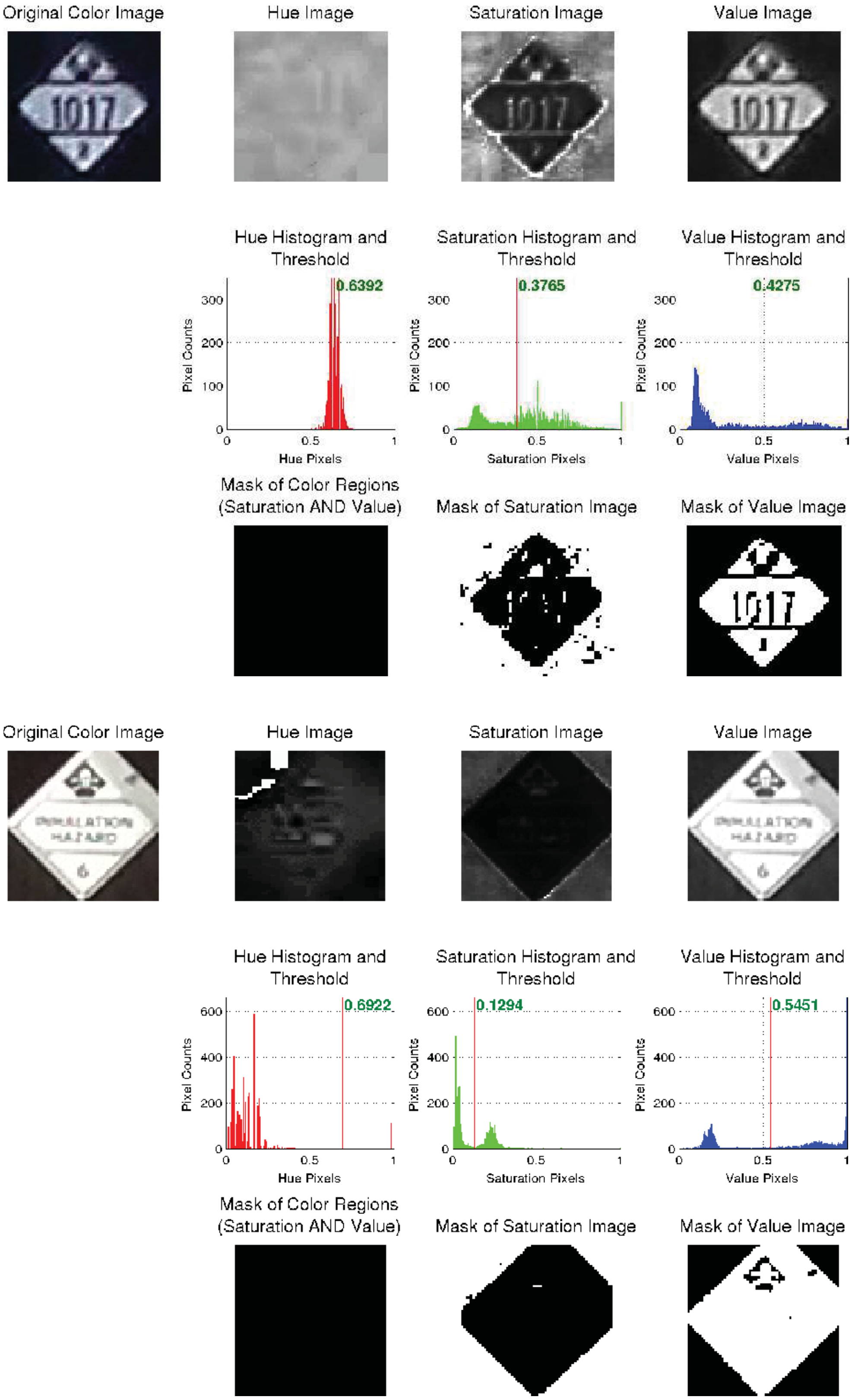

Fig. 3.13. Examples of the proposed color recognition method for two white hazmat signs at 50 feet.

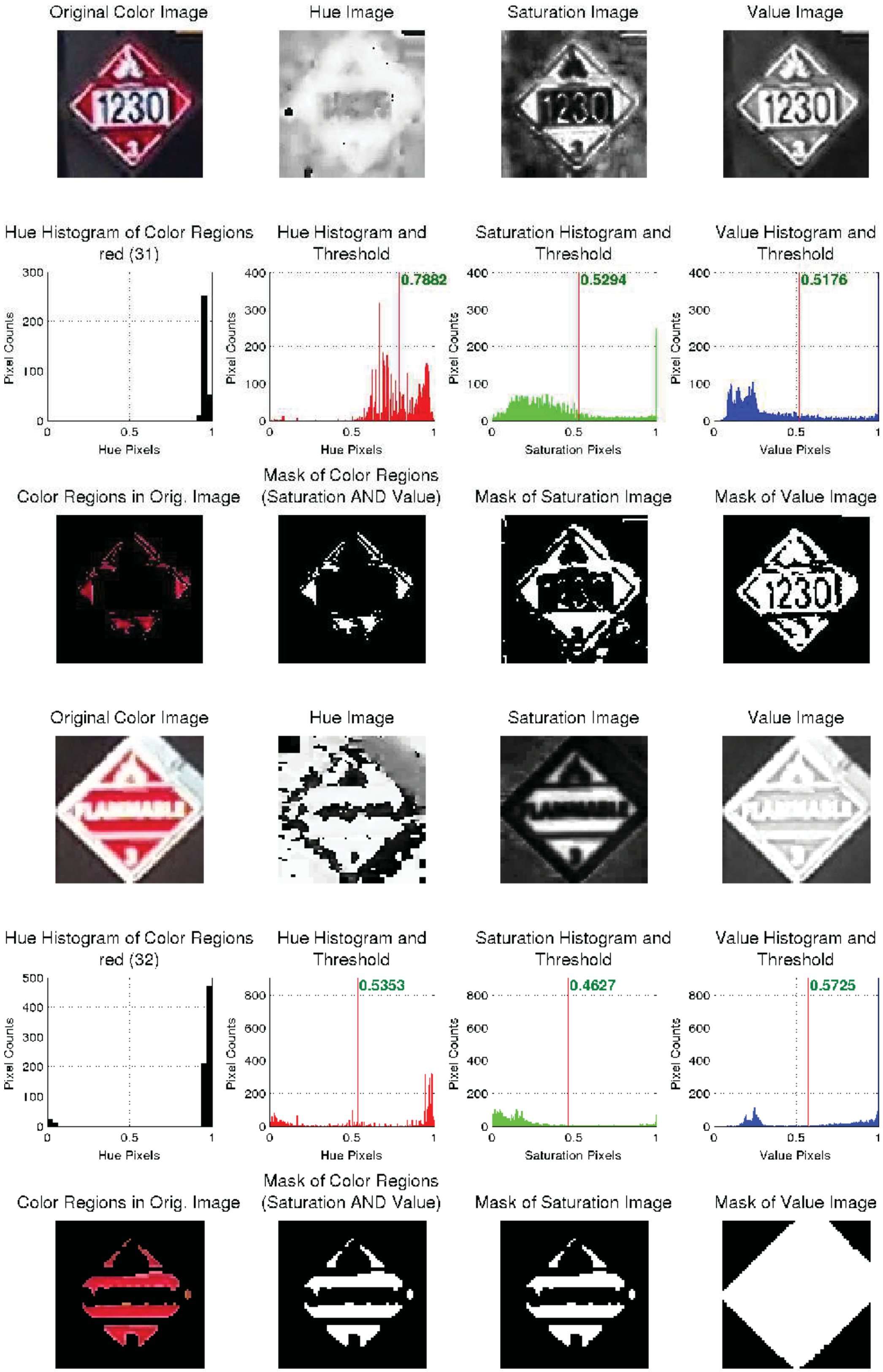

Fig. 3.14. Examples of the proposed color recognition method for two red hazmat signs at 50 feet.

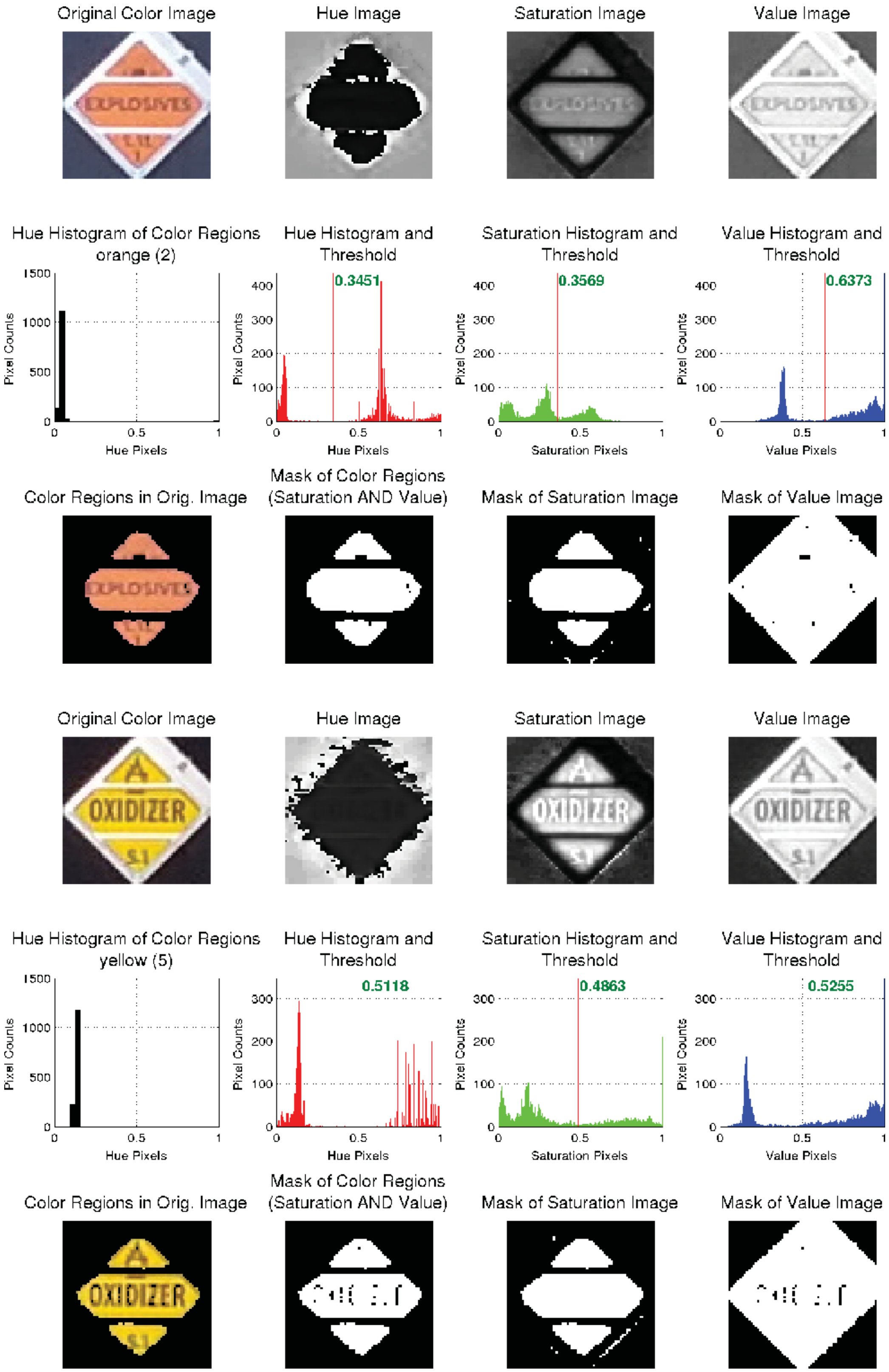

Fig. 3.15. Examples of the proposed color recognition method for orange and yellow hazmat signs at 50 feet.

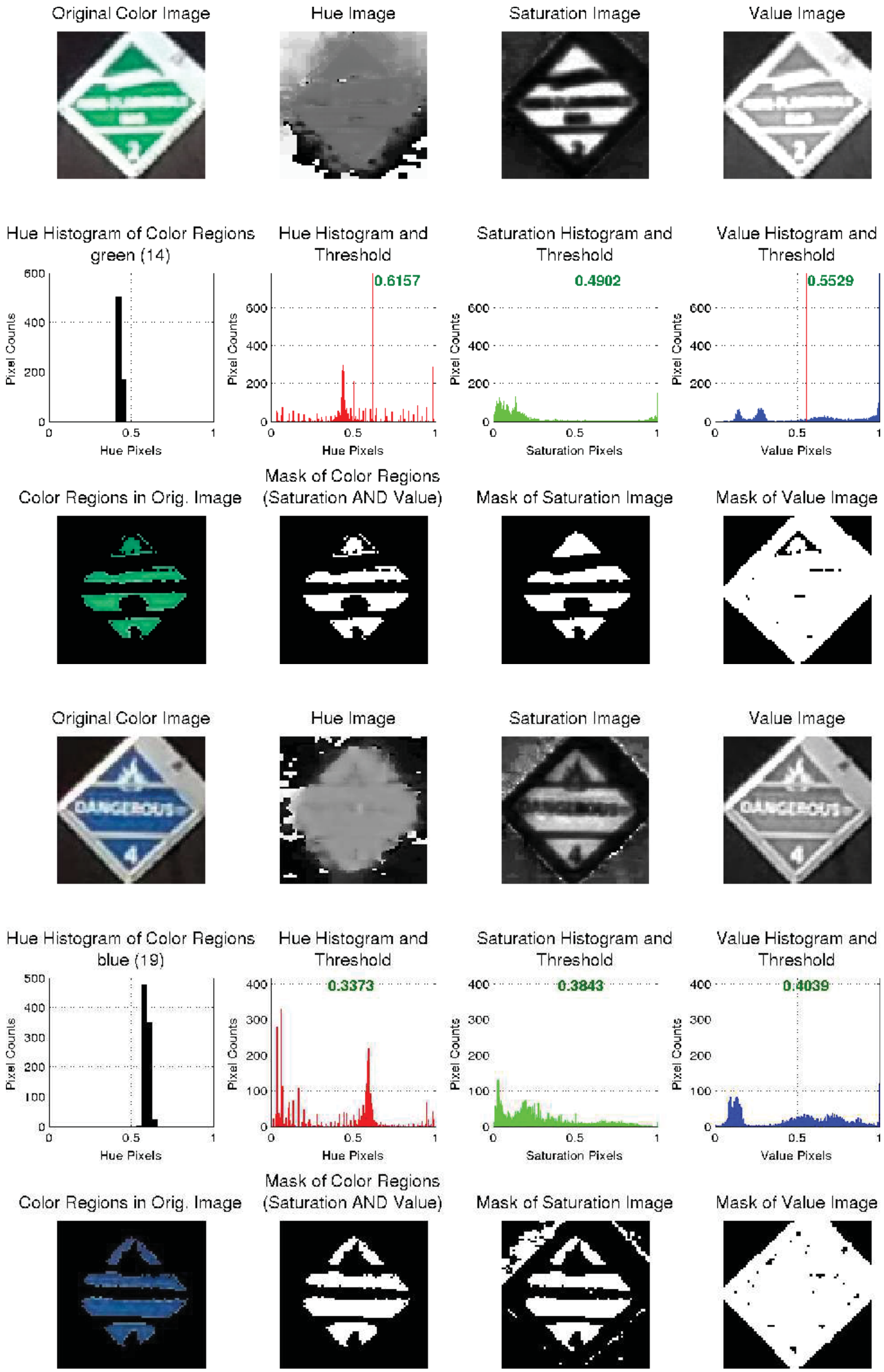

Fig. 3.16. Examples of the proposed color recognition method for green and blue hazmat signs at 50 feet.

3.6 Experimental Results

We did two experiments to investigate the performance and accuracy of our proposed hazmat sign detection and recognition method. The tests were executed on a Galaxy Nexus mobile telephone with a dual-core 1.2GHz CPU and 1GB RAM and a backend server with a quad-core 2.4GHz CPU and 4GB RAM. The first experiment consisted of generating saliency maps using different visual saliency models and evaluating their performance of locating hazmat signs based on ground-truth information. The second experiment consisted of hazmat sign detection and recognition on our image datasets and comparing the results with ground-truth information. The ground-truth information include the image resolution, the number of pixels on the sign, the distance from the camera to the sign, sign color, and sign location in the image.

3.6.1 Image Datasets

Our first image dataset (Dataset-1) consisted of 50 images, each containing one or more hazmat signs in a complex scene (62 hazmat signs in total). The hazmat sign images were captured by a third party under various lighting conditions, distances and perspectives using three different cameras: a 5 MP camera on an HTC Wildfire mobile telephone (2592×1952), an 8.2 MP Kodak Easyshare C813 digital camera (3296×2472), and a 16 MP Nikon Coolpix S800c digital camera (1600×1200) (MP stands for Mega Pixel). Among the 50 images, 23 were reported at 10-50 feet, 23 at 50-100 feet, and 4 at 100-150 feet. Among the 62 hazmat signs, 2 had low resolution, 11 had projective distortion, 8 were blurred, and 6 were shaded. This image dataset contains images of red, yellow, and white hazmat signs. Figure 3.17 illustrates some examples of the first image dataset (Dataset-1) in different conditions.

Our second image dataset (Dataset-2) consisted of 100 images, each containing one or more hazmat signs in a complex scene (111 hazmat signs in total). The hazmat sign images were captured by a third party under various lighting conditions, distances

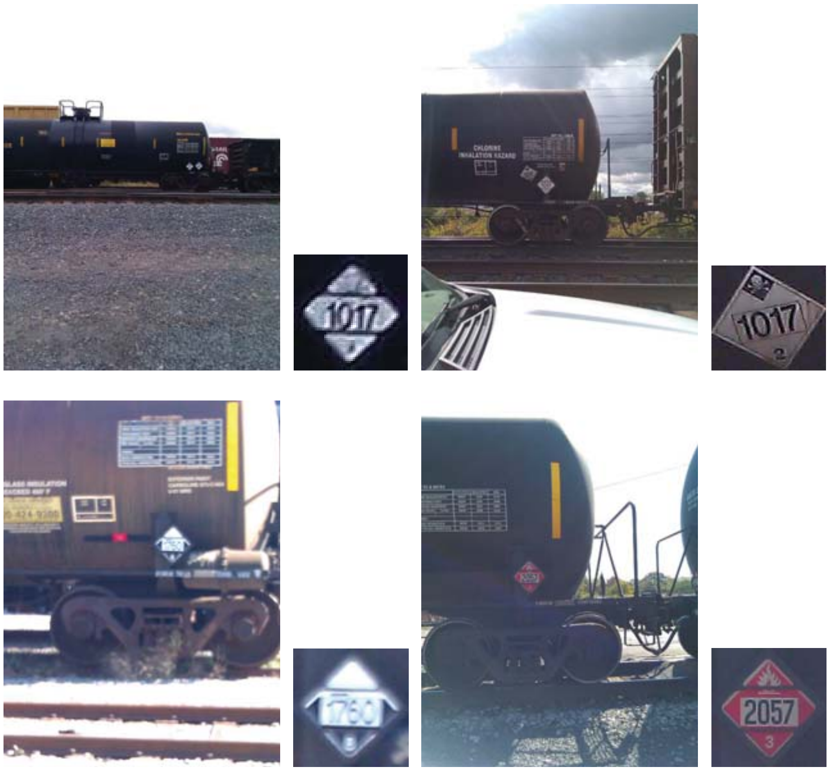

Fig. 3.17. Examples of the first image dataset (Dataset-1) in different conditions (left to right then top to bottom): low resolution, perspective distortion; blurred sign, shaded sign.

and perspectives using the 16 MP Nikon Coolpix S800c digital camera, including 36 low resolution 2 MP images (1600×1200) and 64 full resolution 16 MP images (4608×3456) from the same camera. Among the 100 images, 22 were reported at 10-50 feet, 35 at 50-100 feet, and 43 at 100-150 feet. Among the 111 hazmat signs, 46 had low resolution, 25 had projective distortion, 12 were blurred, and 17 were shaded. This image dataset contains images of red and white hazmat signs. Figure 3.18 illustrates some examples of the second image dataset (Dataset-2) in different conditions.

Our third image dataset (Dataset-3) consisted of 252 images, each containing only one hazmat sign in a complex scene (252 hazmat signs in total). We use 6 available hazmat signs in different colors for this image dataset, including red, green, blue, orange, yellow, and white. All of them have a warning text in the middle of the signs

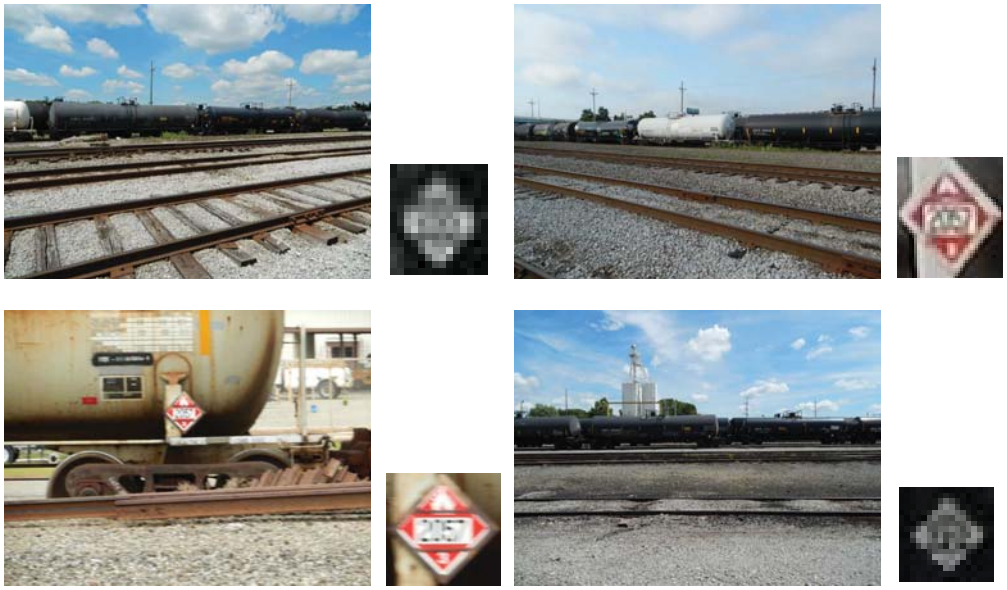

Fig. 3.18. Examples of the second image dataset (Dataset-2) in different conditions (left to right then top to bottom): low resolution, perspective distortion; blurred sign, shaded sign.

often used by truck trailer. The images were acquired by us in the outdoor field under various lighting conditions and distances. We took the images at various distances with ground-truth measurement, *i.e.* 10, 25, 50, 75, 100, 125, and 150 feet. The hazmat sign images were captured by us using 3 different cameras: a 5 MP camera on an HTC Wildfire mobile telephone (2592×1952), a 5 MP camera on a Samsung Galaxy Nexus mobile telephone (2592×1944), and a 10 MP Canon PowerShot S95 digital camera (3648×2736) (MP stands for Mega Pixel). At each distance, 36 images were taken by the 3 cameras in both portrait mode and landscape mode (12 images of the 6 hazmat signs in each scene). Among the 252 images, 36 were measured and captured in a straight view at 10 feet, 36 at 25 feet, 36 at 50 feet, 36 at 75 feet, 36 at 100 feet, 36 at 125 feet, and 36 at 150 feet. The 252 hazmat signs have clear appearances without any shape distortion in the images. This image dataset contains images of red, green, blue, orange, yellow, and white hazmat signs. Figure 3.19 and Figure 3.20 illustrate some examples of the 6 signs of the third image dataset (Dataset-

3) at 10 feet in portrait an landscape mode respectively (Images were captured by the 5 MP camera on a Samsung Galaxy Nexus mobile telephone).

The distance information of the first and second image datasets (Dataset-1 and Dataset-2) is visually estimated and thus not reliable. The images were also acquired by a third party in the working field, under various lighting and weather conditions, distances, and perspectives. The distance information of the third image dataset (Dataset-3) is reliable and obtained with ground-truth measurement. The images were acquired by us in the outdoor field under various lighting conditions and distances.

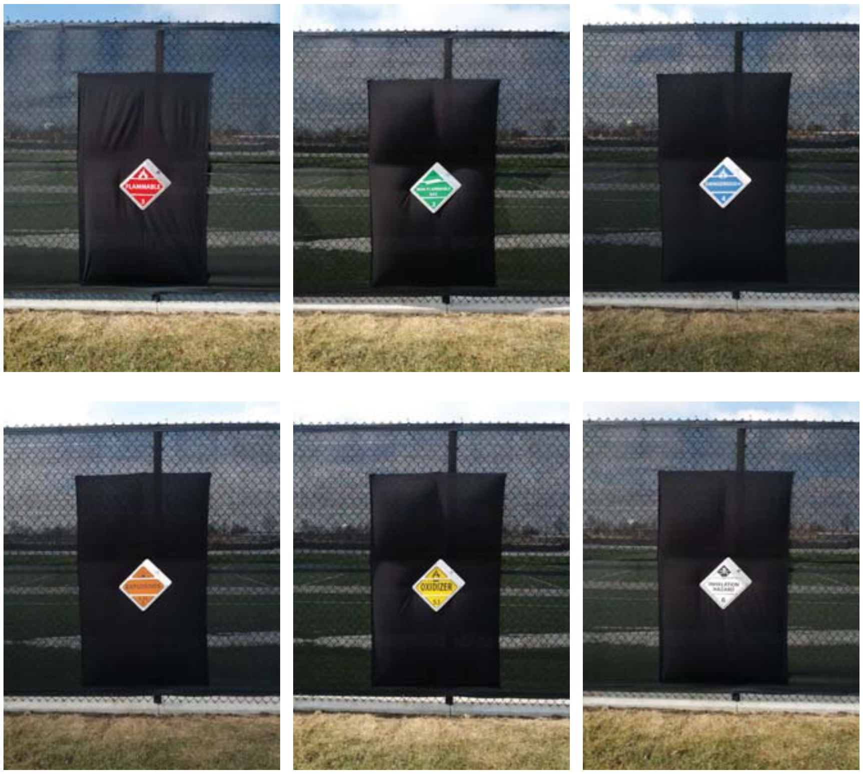

Fig. 3.19. Examples of the 6 signs of Dataset-3 at 10 feet in portrait mode (left to right then top to bottom): red sign, green sign, blue sign; orange sign, yellow sign, white sign.

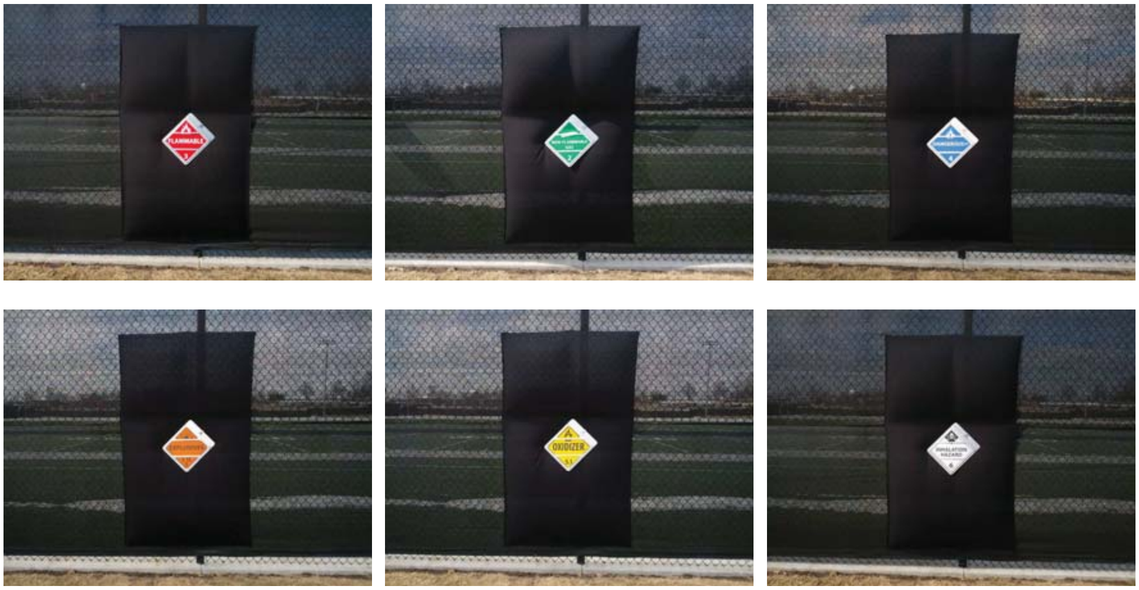

Fig. 3.20. Examples of the 6 signs of Dataset-3 at 10 feet in landscape mode (left to right then top to bottom): red sign, green sign, blue sign; orange sign, yellow sign, white sign.

Figure 3.21 illustrate some bounding box images for a typical STOP sign and a hazmat sign at the same distance 25, 50, 100, and 150 feet. Table 3.3 shows the relation among the image resolution of a certain camera, the distance from a camera to a hazmat sign, and the number of pixels on a hazmat sign. It also reports the pixel ratio of STOP and hazmat sign by comparing it to a typical STOP sign at each distance. On average, a typical STOP sign contains 5.60 times pixels than a hazmat sign at the same distance.

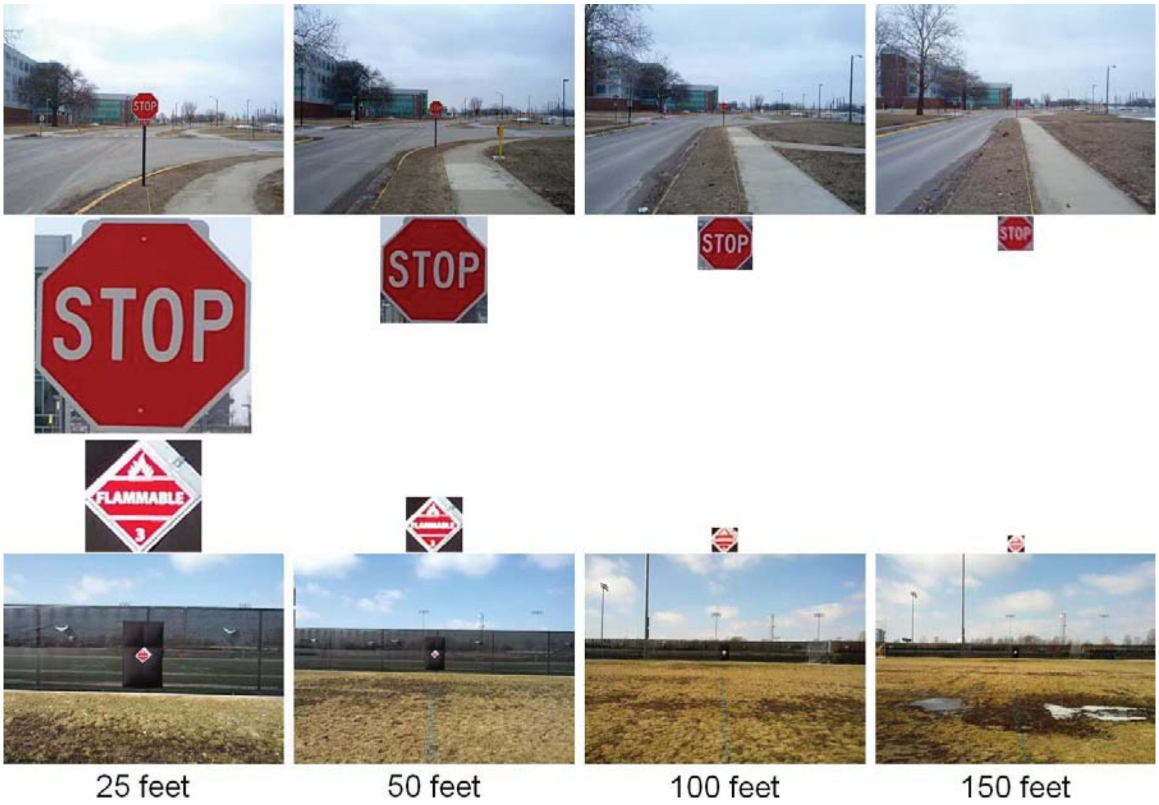

Fig. 3.21. Examples of bounding box images for a typical STOP sign and a hazmat sign at the same distance 25, 50, 100, and 150 feet.

Table 3.3
The relation among the image resolution, the distance from a camera to a hazmat sign, and the number of pixels on a hazmat sign in the third image dataset (Dataset-3) with comparison to a typical STOP sign.

Camera (Image Resolution)	10 feet	25 feet	50 feet	75 feet	100 feet	125 feet	150 feet
Canon PowerShot S95 (3648×2736)	90312	14450	3444	1458	840	512	364
Hazmat Sign Bounding Box (Pixel Ratio=0.5)	425×425	170×170	83×83	54×54	41×41	32×32	27×27
HTC Wildfire (2592×1952)	57800	9522	2312	1012	578	364	242
Hazmat Sign Bounding Box (Pixel Ratio=0.5)	340×340	138×138	68×68	45×45	34×34	27×27	22×22
Samsung Galaxy Nexus (2592×1944)	56112	9248	2244	1012	578	364	242
Hazmat Sign Bounding Box (Pixel Ratio=0.5)	335×335	136×136	67×67	45×45	34×34	27×27	22×22
Samsung Galaxy Nexus (2592×1944)	298235	50952	12738	5845	3288	1989	1393
STOP Sign Bounding Box (Pixel Ratio=0.82843)	600×600	248×248	124×124	84×84	63×63	49×49	41×41
Pixel Ratio of STOP and Hazmat Sign (Avg=5.60)	5.315	5.510	5.676	5.776	5.689	5.464	5.756

3.6.2 The First Experiment

In the first experiment, we tested our best GCS visual saliency models and 4 state-of-the-art models, including SBVA [25], GBVS [26], IS-DCT-Lab [33], SSA-HFT-IRGBY [35], by hazmat sign image dataset. This experiment consisted of evaluating their performance using a hazmat sign image dataset and scoring the resultant saliency maps in locating hazmat signs based on ground-truth information. We use the first hazmat sign image dataset (Dataset-1) for evaluation and it consists of 50 images and 62 hazmat signs in total.

The saliency models are evaluated in the experiment are: SBVA [25], GBVS [26], IS [33], SSA [35]. We classified the resulting saliency maps into four categories: good, fair, bad, and lost. For each sign, we assigned 3 points for a good saliency map (sign was mostly contained in high salient regions SR_{high}), 2 points for a fair saliency map (sign was mostly contained in middle salient regions SR_{middle}), 1 point for a bad saliency map (sign was mostly contained in low salient regions SR_{low}), and 0 points for a lost saliency map (sign was mostly contained in non-salient regions SR_{non}). The type of salient regions are distinguished by a set of predefined thresholds (The multiples of the average saliency value of a given saliency map based on the Equation 3.2).

$$
\begin{aligned}
SR_{high} &= \{\bigcup_{(x,y)} S(x,y) | T_{high} \leqslant S(x,y) \leqslant 1\}, && (3.15)\\
SR_{middle} &= \{\bigcup_{(x,y)} S(x,y) | T_{middle} \leqslant S(x,y) < T_{high}\}, && (3.16)\\
SR_{low} &= \{\bigcup_{(x,y)} S(x,y) | T_{low} \leqslant S(x,y) < T_{middle}\}, && (3.17)\\
SR_{non} &= \{\bigcup_{(x,y)} S(x,y) | 0 \leqslant S(x,y) < T_{low}\}, && (3.18)\\
T_{high} &= \frac{4}{W \times H} \sum_{x=1}^{W} \sum_{y=1}^{H} S(x,y), && (3.19)\\
T_{middle} &= \frac{2}{W \times H} \sum_{x=1}^{W} \sum_{y=1}^{H} S(x,y), && (3.20)\\
T_{low} &= \frac{1}{W \times H} \sum_{x=1}^{W} \sum_{y=1}^{H} S(x,y), && (3.21)
\end{aligned}
$$

where W and H are the width and height of the saliency map, $S(x, y)$ is the saliency value at position (x, y). Since saliency map is a probability map for predicting the location of eye fixations in a scene, high salient regions are defined as their saliency values are not less than the threshold T_{high}, middle salient regions are between the threshold T_{high} and T_{middle}, low salient regions are between the threshold T_{middle} and T_{low}, and non-salient regions are between the threshold T_{low} and 0. Examples of the four categories of saliency maps (good, fair, bad, lost) with our defined four types of salient regions (high, middle, low, non) are demonstrated from Figure 3.22 to Figure 3.25.

We evaluated above saliency map methods based on average execution times, the distribution of above categories and the calculated score. Table 3.4 shows the results of the visual saliency models in locating hazmat signs. The score of each saliency map method is calculated as the sum of the points assigned for all 62 hazmat signs, which ranges from 0 to 186. Note that the SBVA and the GBVS methods use one color space. Compared with the SBVA and the GBVS methods using one color space, the IS and the SSA methods using one color space have comparable scores, while the IS and

Table 3.4
Average execution time (in seconds), distribution and score of the saliency models (color spaces) in the first image dataset (Dataset-1).

Saliency Map	Time	Good	Fair	Bad	Lost	Score
SBVA(IRGBY)	2.07	28	16	12	6	128
GBVS(IRGBY)	3.36	25	15	15	7	120
IS(Lab)	0.39	27	5	20	10	111
IS(RGB)	0.36	22	7	27	6	107
SSA(Lab)	0.55	33	8	12	9	127
SSA(RGB)	0.53	38	5	8	11	132
IS+SSA(Lab+RGB)	1.83	41	6	8	7	143
GCS(Lab)	0.43	37	10	8	7	139
GCS(RGB)	0.41	28	16	12	6	128
GCS(Lab+RGB)	0.84	52	6	1	3	169

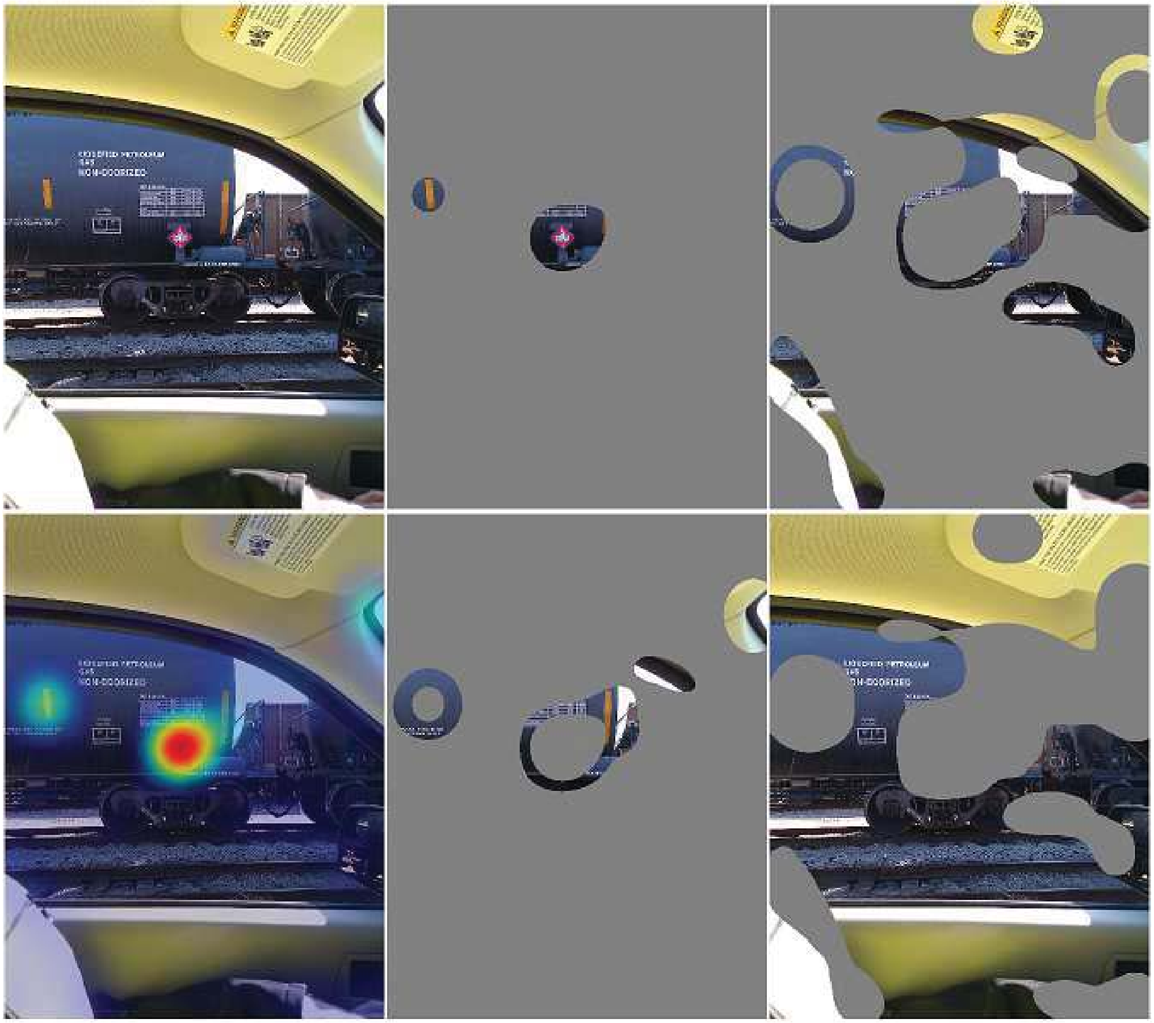

Fig. 3.22. An example of good saliency map with the four types of salient regions (top to bottom then left to right): original image, good saliency map; high salient regions, middle salient regions; low salient regions, non-salient regions.

the SSA methods using two color spaces have higher scores. The GCS(Lab+RGB) and the IS+SSA(Lab+RGB) methods using two color spaces run 2.46 and 1.13 times faster than the SBVA method and 4.0 and 1.84 times faster than the GBVS method respectively. The results verified that the proposed GCS(Lab+RGB) model, combining GCS-FT-Lab and GCS-FT-RGB models, can improve the score of generated

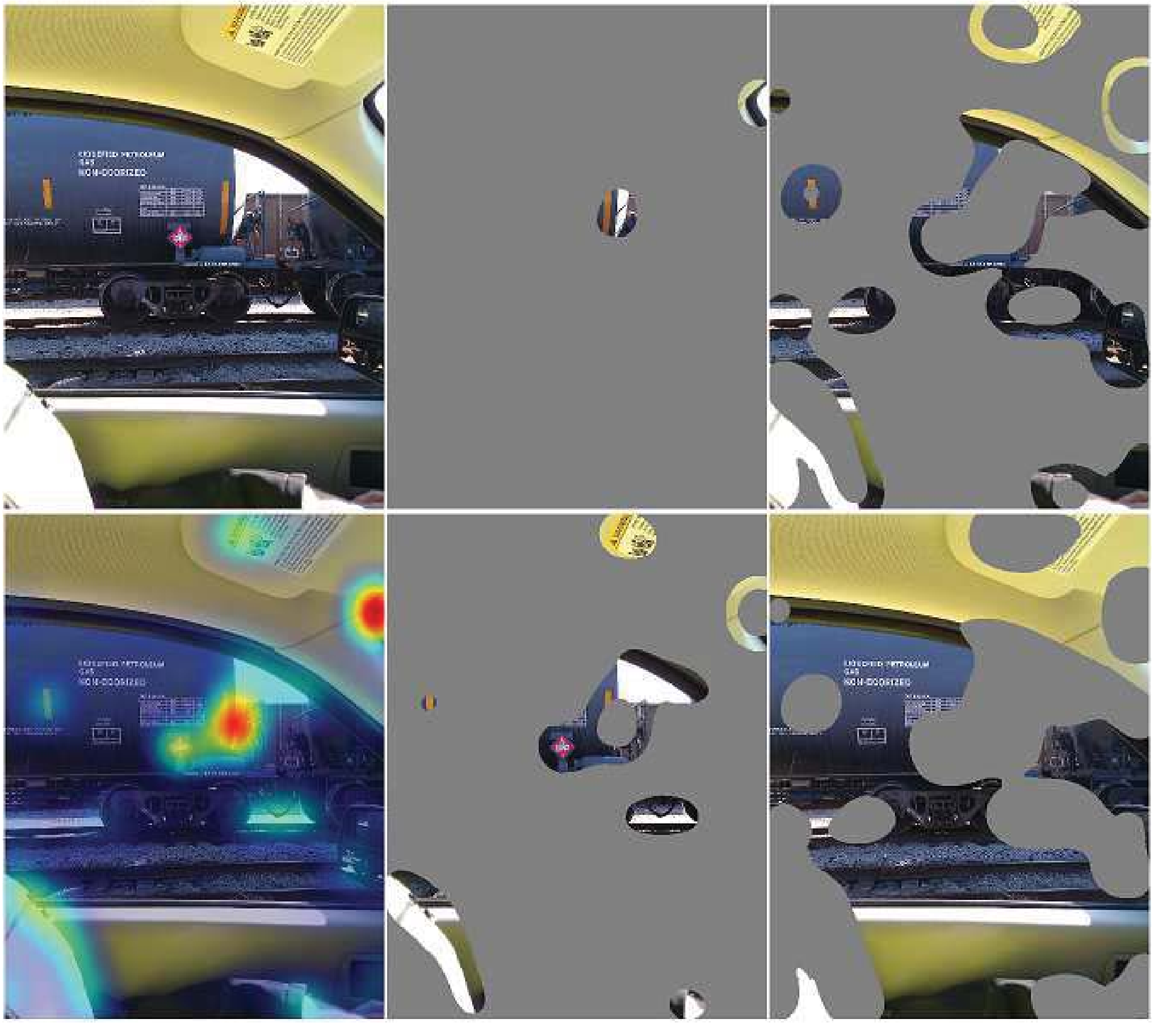

Fig. 3.23. An example of fair saliency map with the four types of salient regions (top to bottom then left to right): original image, fair saliency map; high salient regions, middle salient regions; low salient regions, non-salient regions.

saliency maps, while still running faster than SBVA and GBVS methods. Figure 3.26 and Figure 3.27 illustrate examples of saliency maps from different methods for the same hazmat sign images in portrait mode and landscape mode. Note that the table in the middle indicates the locations of the saliency maps corresponding to which methods.

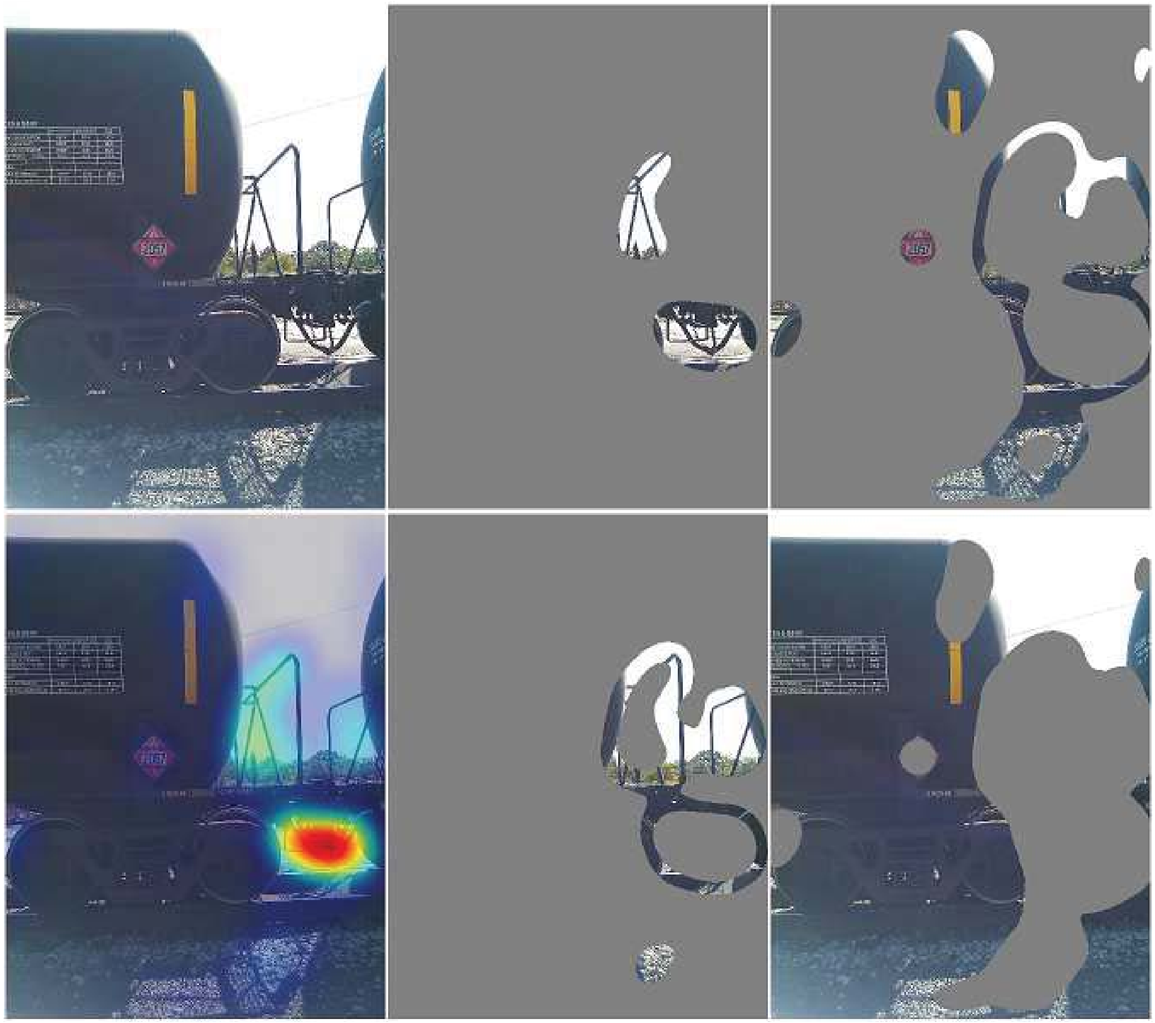

Fig. 3.24. An example of bad saliency map with the four types of salient regions (top to bottom then left to right): original image, bad saliency map; high salient regions, middle salient regions; low salient regions, non-salient regions.

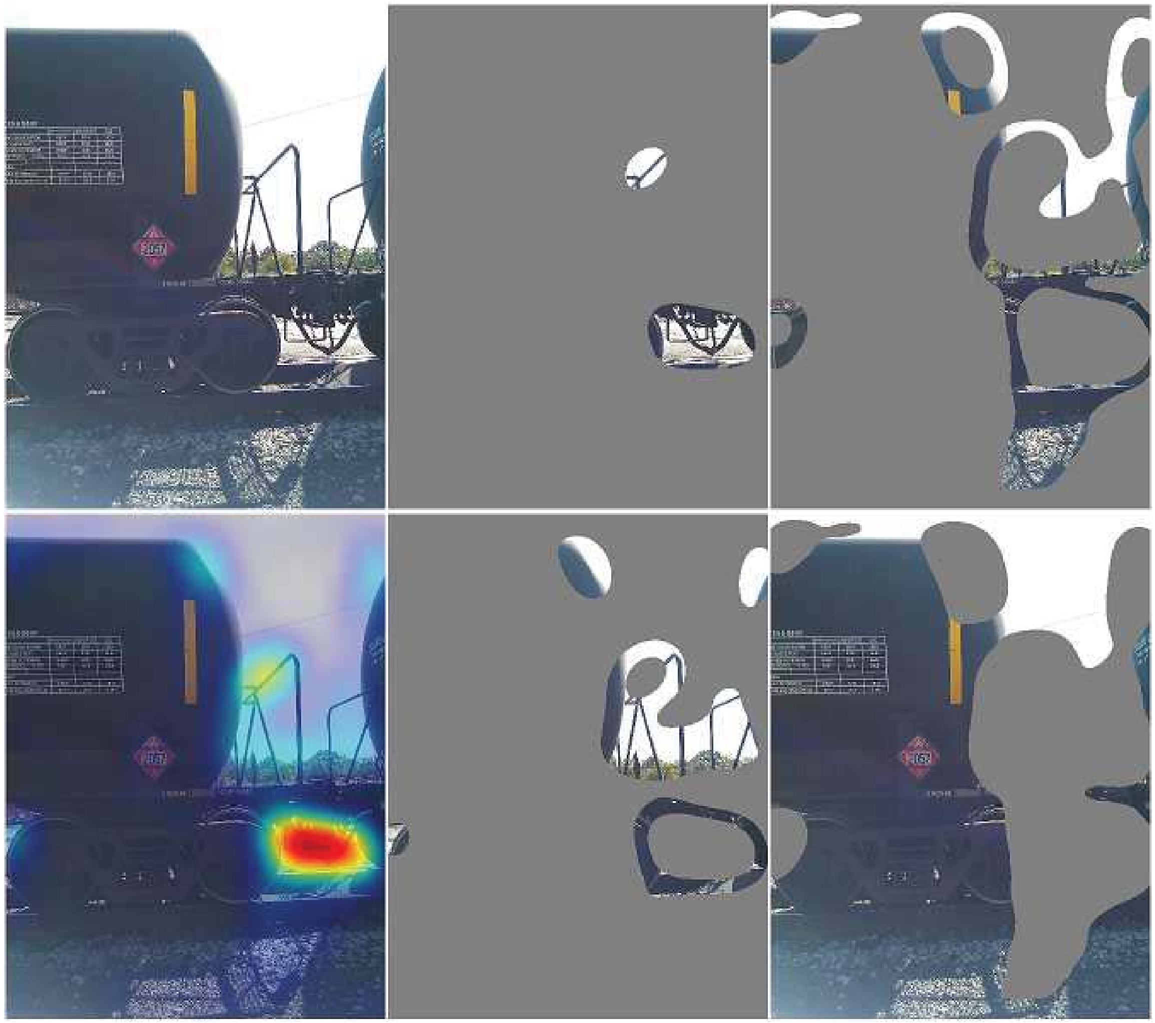

Fig. 3.25. An example of lost saliency map with the four types of salient regions (top to bottom then left to right): original image, lost saliency map; high salient regions, middle salient regions; low salient regions, non-salient regions.

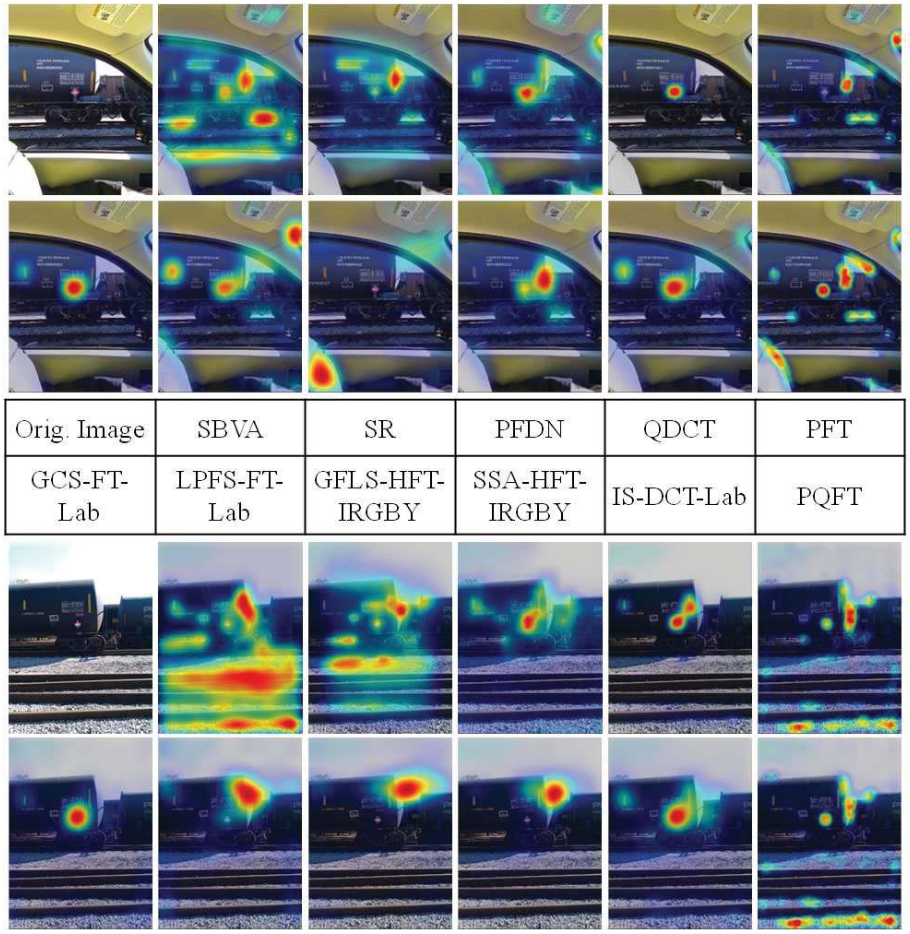

Fig. 3.26. Examples of saliency maps from different methods for two hazmat sign images in portrait mode.

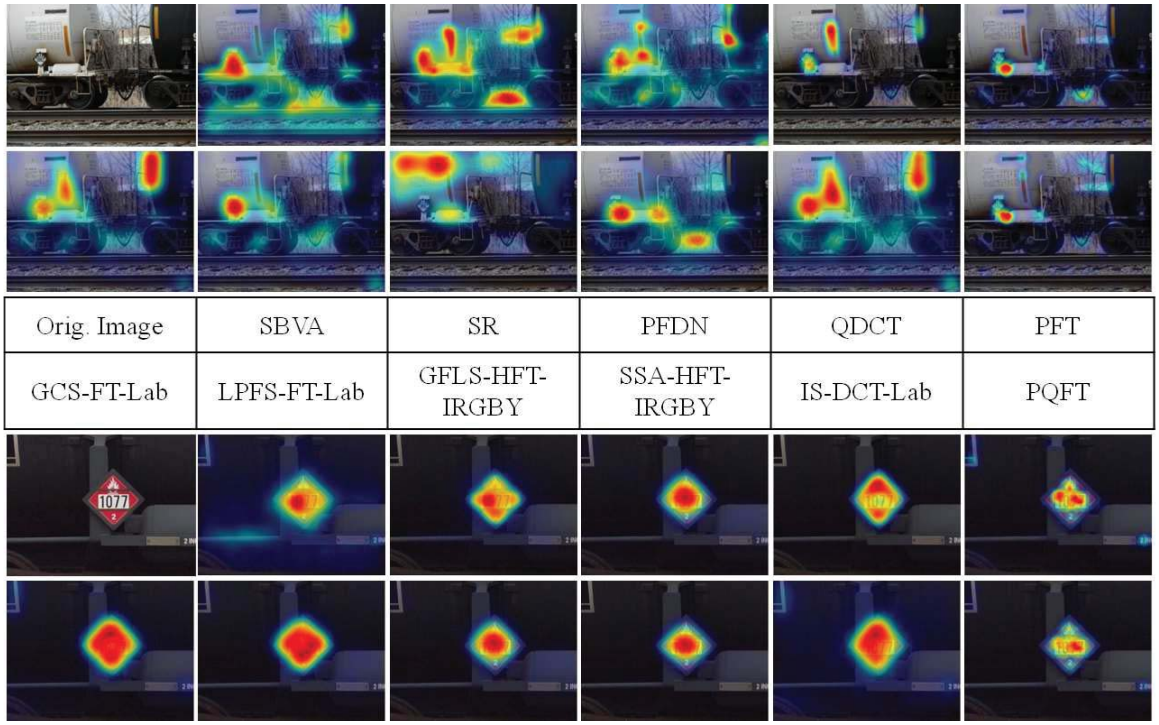

Fig. 3.27. Examples of saliency maps from different methods for two hazmat sign images in landscape mode.

3.6.3 The Second Experiment

In the second experiment, we evaluate the performance of our hazmat sign detection and recognition methods in detecting and recognizing hazmat signs in complex scenes. We employ the following quantitative measurements to evaluate the previous Method 1 and the proposed Method 2.

$$\begin{aligned}
\mathsf{Accuracy} &= \frac{\mathsf{The\ Number\ of\ Correct\ Resultant\ Signs}}{\mathsf{The\ Total\ Number\ of\ Signs}}, && (3.22)\\
\mathsf{Mistakenness} &= \frac{\mathsf{The\ Number\ of\ False\ Positive\ Objects}}{\mathsf{The\ Total\ Number\ of\ Signs}}, && (3.23)\\
\mathsf{Sign\text{-}Coverage} &= \frac{\mathsf{The\ Number\ of\ Signs\ Covered\ in\ Extracted\ Salient\ Regions}}{\mathsf{The\ Total\ Number\ of\ Signs}}, && (3.24)\\
\mathsf{Pixel\text{-}Usage} &= \frac{\mathsf{The\ Number\ of\ Pixels\ Used\ in\ Extracted\ Salient\ Regions}}{\mathsf{The\ Total\ Number\ of\ Pixels\ in\ The\ Image}}. && (3.25)
\end{aligned}$$

Table 3.5 illustrates the performance of the generated saliency maps and salient region extraction methods in terms of the pixel usage and sign coverage in the extracted salient regions of complex scenes. For the three image datasets, the previous Method 1 using four saliency maps obtains the average pixel usage 13.81% and the average sign coverage 96.24%, while the proposed Method 2 using two saliency maps achieves the average pixel usage 10.98% and the average sign coverage 97.41%. Hazmat sign image analysis focusing on the extracted salient regions can achieve good sign coverage and further speed up the overall image analysis process by using only a small portion of pixels, instead of using the entire pixels in an image.

Table 3.5
The pixel usage and sign coverage in the extracted salient regions for the three image datasets.

	Dataset-1	Dataset-1	Dataset-2	Dataset-2	Dataset-3	Dataset-3	Average	Average
Proposed Method	Pixel Usage	Sign Coverage	Pixel Usage	Sign Coverage	Pixel Usage	Sign Coverage	Pixel Usage	Sign Coverage
IS+SSA(Lab+RGB) Sal. Maps	15.29%	98.39%(61/62)	14.63%	95.50%(106/111)	11.52%	96.03%(242/252)	13.81%	96.24%(409/425)
GCS(Lab+RGB) Sal. Maps	12.52%	98.39%(61/62)	11.73%	96.40%(107/111)	8.70%	97.62%(246/252)	10.98%	97.41%(414/425)

The accuracy of sign location detection is significantly related to the image resolution of a certain camera, the distance from a camera to a hazmat sign, and the number of pixels on a hazmat sign. We then determine the color recognition accuracy based on how many signs were correctly color recognized after a successful sign location detection. Note that we used the recognized color inside the sign, not text or UN identifier numbers, queuing the mobile database for sign category identification and providing the general guide information. Therefore the overall accuracy is equivalent to the color recognition accuracy in our experiments.

Table 3.6 illustrates the image analysis results of the proposed methods for the first image dataset (Dataset-1). The previous Method 1 using the IS+SSA(Lab+RGB) model has the location detection accuracy 64.52% and the color recognition accuracy 45.16% for all 62 hazmat signs. The proposed Method 2 using our GCS(Lab+RGB) model obtains the location detection accuracy 67.74% and the color recognition accuracy 61.29%, while the same method without using saliency maps yields 56.45% and 50.00% respectively. Table 3.7 demonstrates the image analysis results of the proposed methods for the second image dataset (Dataset-2). The previous Method 1 using the IS+SSA(Lab+RGB) model has the location detection accuracy 40.54% and the color recognition accuracy 29.73% for all 111 hazmat signs. The proposed Method 2 using our GCS(Lab+RGB) model obtain the location detection accuracy 54.05% and the color recognition accuracy 53.15%, while the same method without using saliency maps yields 43.24% and 42.34% respectively. Compared with our previous Method 1 using the IS+SSA(Lab+RGB) model with four saliency maps, our proposed Method 2 using our GCS(Lab+RGB) model with two saliency maps has higher accuracy of sign location detection in general. Our experimental results confirmed that the proposed visual saliency based image analysis methods can increase the accuracy of sign location detection and reduce the false positive (FP) objects.

For our third image dataset (Dataset-3), Table 3.8, Table 3.9 and Table 3.10 show more image analysis results of the proposed methods at variant distances for the third image dataset (Dataset-3), including the mistakenness of false positive (FP) objects,

Table 3.6
Image analysis results for the first image dataset (Dataset-1).

Proposed Method	Total Signs	FP Object Extracted	FP Object Mistakenness	Location Detected	Location Accuracy	Color Recognized	Color Accuracy	Overall Accuracy
Method 1 IS+SSA(Lab+RGB) Sal. Maps	62	10	16.13%	40	64.52%	28	45.16%	45.16%
Method 2 without Sal. Maps	62	32	51.61%	35	56.45%	31	50.00%	50.00%
Method 2 GCS(Lab+RGB) Sal. Maps	62	21	33.87%	42	67.74%	38	61.29%	61.29%

Table 3.7
Image analysis results for the second image dataset (Dataset-2).

Proposed Method	Total Signs	FP Object Extracted	FP Object Mistakenness	Location Detected	Location Accuracy	Color Recognized	Color Accuracy	Overall Accuracy
Method 1 IS+SSA(Lab+RGB) Sal. Maps	111	24	21.62%	45	40.54%	33	29.73%	29.73%
Method 2 without Sal. Maps	111	81	72.97%	48	43.24%	47	42.34%	42.34%
Method 2 GCS(Lab+RGB) Sal. Maps	111	45	40.54%	60	54.05%	59	53.15%	53.15%

the location detection accuracy, the color recognition accuracy, and the overall process accuracy. The previous Method 1 using the IS+SSA(Lab+RGB) model has the average location detection accuracy 56.75% and the average color recognition accuracy 19.05% for all 252 hazmat signs. The proposed Method 2 using our GCS(Lab+RGB) model achieves the average location detection accuracy 96.83% and the average color recognition accuracy 90.87%, while the same method using saliency maps obtains 87.70% and 82.54% respectively. The previous Method 1 has high location accuracy at short distances but decreases after 50 feet and fails to detect sign location after 125 feet. The proposed Method 2 achieve relatively consistent location accuracy at all distances from 10 feet to 150 feet, because we used the adaptive contour extraction method within more accurate saliency regions and the robust contour matching method based on Fourier descriptors.

For the overall process of our hazmat sign image analysis system, the average execution time of the previous Method 1 and the one of the proposed Method 2 are 5.88 and 5.28 seconds respectively for the first image dataset (Dataset-1), 18.95 and 16.45 seconds respectively for the second image dataset (Dataset-2), while 10.24 and 8.98 seconds respectively for the third image dataset (Dataset-3). The average execution time of the proposed Method 2 without using saliency maps are 8.49, 26.52, and 14.36 seconds for the three image datasets respectively. Our experimental results verified that the proposed visual saliency based methods can speed up the overall image analysis process. With better location detection accuracy and color recognition accuracy, the proposed Method 2 using the GCS(Lab+RGB) model is faster than the previous Method 1 using the IS+SSA(Lab+RGB) model and more suitable for practical applications and uses.

Table 3.8
Image analysis results of Method 1 using four saliency maps for the third image dataset (Dataset-3).

Method 1 IS+SSA(Lab+RGB) Sal. Maps	Total Signs	FP Object Extracted	FP Object Mistakenness	Location Detected	Location Accuracy	Color Recognized	Color Accuracy	Overall Accuracy
10 feet	36	8	22.22%	36	100.00%	10	27.78%	27.78%
25 feet	36	4	11.11%	36	100.00%	16	44.44%	44.44%
50 feet	36	2	5.56%	34	94.44%	10	27.78%	27.78%
75 feet	36	1	2.78%	23	63.89%	7	19.44%	19.44%
100 feet	36	1	2.78%	11	30.56%	3	8.33%	8.33%
125 feet	36	4	11.11%	3	8.33%	2	5.56%	5.56%
150 feet	36	4	11.11%	0	0.00%	0	0.00%	0.00%
Average	252	24	9.52%	143	56.75%	48	19.05%	19.05%

Table 3.9
Image analysis results of Method 2 without using saliency maps for the third image dataset (Dataset-3).

Method 2 without using Sal. Maps	Total Signs	FP Object Extracted	FP Object Mistakenness	Location Detected	Location Accuracy	Color Recognized	Color Accuracy	Overall Accuracy
10 feet	36	4	11.11%	33	91.67%	29	80.56%	80.56%
25 feet	36	50	138.89%	26	72.22%	26	72.22%	72.22%
50 feet	36	3	8.33%	34	94.44%	33	91.67%	91.67%
75 feet	36	5	13.89%	32	88.89%	30	83.33%	83.33%
100 feet	36	3	8.33%	34	94.44%	32	88.89%	88.89%
125 feet	36	9	25.00%	30	83.33%	28	77.78%	77.78%
150 feet	36	3	8.33%	32	88.89%	30	83.33%	83.33%
Average	252	77	30.56%	221	87.70%	208	82.54%	82.54%

Table 3.10
Image analysis results of Method 2 using two saliency maps for the third image dataset (Dataset-3).

Method 2 GCS(Lab+RGB) Sal. Maps	Total Signs	FP Object Extracted	FP Object Mistakenness	Location Detected	Location Accuracy	Color Recognized	Color Accuracy	Overall Accuracy
10 feet	36	0	0.00%	36	100.00%	32	88.89%	88.89%
25 feet	36	1	2.78%	36	100.00%	36	100.00%	100.00%
50 feet	36	0	0.00%	36	100.00%	35	97.22%	97.22%
75 feet	36	1	2.78%	36	100.00%	34	94.44%	94.44%
100 feet	36	7	19.44%	33	91.67%	31	86.11%	86.11%
125 feet	36	20	55.56%	33	91.67%	30	83.33%	83.33%
150 feet	36	19	52.78%	34	94.44%	31	86.11%	86.11%
Average	252	48	19.05%	244	96.83%	229	90.87%	90.87%

Discussion

¿From the experiments our accuracy ranged from approximately 90% for images taken is a controlled test environment to approximately 60% for image acquired in a more “typical” operating scenario. The accuracy we obtained in a more typical operating scenario would not be acceptable for many situations. The overall accuracy of our hazmat sign image analysis system is affected by the location and color recognition accuracy. The accuracy of sign location detection is significantly related to the image resolution of the camera, the distance from the camera to a hazmat sign, and the number of pixels forming the hazmat sign. As mentioned above, we show the relation between these factors in Table 3.3. The location detection accuracy of the first Dataset-1 67.74% and the second Dataset-2 54.05% were lower than the average one of the third Dataset-3 96.83%, because there are a large number of blurred, low resolution, and perspective distorted hazmat signs contained in the first Dataset-1 and the second Dataset-2. Note that hazmat signs in the third Dataset-3 were acquired in a controlled test environment without any shape distortion in the images. The location detection accuracy deteriorates due to the loss of boundary contours for blurred and low resolution hazmat signs and poor correlation in contour matching for perspective distorted hazmat signs.

The color recognition accuracy is based on how many signs were correctly color recognized after a successful sign location detection. The color recognition accuracy of the first Dataset-1 61.29% and the second Dataset-2 53.15% were also lower than the average one of the third Dataset-3 90.87%, because the color recognition accuracy will not exceed the previous location detection accuracy. The color recognition accuracy is also degraded by the absence of color calibration for hazmat sign images, especially for shaded signs, which cause our color recognition method to misidentify the sign color.

The location detection accuracy could be improved by using supper-resolution image reconstruction methods [126, 127] to refine hazmat sign images at the step of image preprocessing. The color recognition accuracy could be increased by employing proper color calibration methods [51] at the step of image acquisition. Therefore we could further improve the overall accuracy of our hazmat sign image analysis system.

4. ERROR CONCEALMENT FOR SCALABLE VIDEO CODING

A Scalable video coding (SVC) decoder typically requires that the base layer frames be delivered almost error-free and uses them to decode the enhancement layer frames. Due to the nature of dynamic and lossy channels used for video delivery (particularly wireless channels), video bitstreams transmitted over packet networks usually experience isolated and burst packet losses [17]. An accurate distortion model for the effect of different packet loss patterns on the encoded video was proposed in [128]. It confirmed that a burst packet loss produces a larger distortion than an equal number of isolated packet losses. Moreover, once errors occur in video bitstreams, they are prone to propagate from one frame to another due to motion-compensated prediction used in SVC codec. These effects can result in severe visual quality degradation of the decoded frames.

Error concealment (EC) is an effective scheme for error recovery, which imposes small complexity on the decoder and provides a flexible solution to the above problems [129, 130]. By the use of error concealment methods, damaged regions can be reconstructed from the correctly received neighboring regions. Due to the layered structure of SVC, it is advantageous to recover the damaged frames in one layer using the available frames in other layers. It has been shown that one can exploit the spatial and temporal correlations of video frames between different layers to improve the performance of single layer error concealment [18].

Slice structuring [130] is a useful strategy to reduce error propagation from a damaged slice/packet to subsequent slices/packets from burst packet losses. Slice interleaving (SI) [131] and flexible macroblock ordering (FMO) [132] are two common slice structuring schemes. Interleaving approach has been exploited for slice structuring and packetization. A near-optimal packet interleaving method was proposed in [133] based on an optimization criteria in terms of temporal neighbor packet distance. Another packetization method was introduced in [134] based on optimal packetization masks, which aims to simultaneously maximize the intra-partition distance and distribute neighboring coefficients equally among different packets. The FMO technique has been employed to independently assign each macroblock (MB) of a frame to a certain slice group (SG) by a macroblock allocation map (MBAmap). The H.264/AVC video coding standard specifies seven types of FMO to support error resilience [132]. FMO Type 1 is also known as scattered or dispersed slices. The effect of error propagation between frames has been investigated in [135] and a more suitable MBAmap with a reduced effect of error propagation can be generated based on the evaluation of each macroblock's importance. In [136], an adaptive MBAmap updating scheme is proposed to reduce the computational cost of FMO and a slice matching error concealment method is also introduced. In [137], a new FMO method was proposed by solving an optimization problem of optimal MB labeling for burst packet loss resilience.

In this chapter, a two-layer spatial-temporal SVC system is developed for inter-layer error concealment. The enhancement layer has high spatial resolution at high frame rate (e.g. 30 fps) and the base layer has low resolution at low frame rate (e.g. 15 fps). It is assumed that the packet delivery of the base layer is loss-prone the same way as the enhancement layer. In this scenario, three inter-layer error concealment methods are proposed using two new approaches. (1) Motion vector averaging using adaptively averaging over multiple types of motion vectors in different layers for the recovery of lost motion vectors. (2) Slice interleaving utilizing an optimum ordering technique to make the average distance between two contiguous slices as far as possible. The proposed error concealment method is capable of decoding the SVC bitstreams under burst packet losses and reconstructing the damaged frames with enhanced visual quality. The effect of burst packet losses and error propagation on video frames in both layers is investigated regarding two existing and three proposed error concealment methods.

4.1 Error Concealment Methods

4.1.1 Conventional Error Concealment Methods

The SVC reference codec, Joint Scalable Video Model (JSVM), introduced four non-normative error concealment (EC) methods [138] to address the problem of error recovery. (1) Picture copy (PC): Each pixel value of the concealed frame is copied from the corresponding pixel of the first frame in the reference frame list 0. (2) Temporal direct motion vector generation (TD): This predicts a missing frame using two reference frame lists and generates the desired missing motion vectors by scaling the motion vectors inferred from its neighboring reference frames. (3) Motion and residual upsampling or base layer skip (BLSkip): This conceals a lost enhancement layer frame from the predicted P- or B-frames. The residuals and motion vectors of the base layer will be up-sampled to higher resolution for the enhancement layer. (4) Reconstruction base layer upsampling (RU): The base layer frame is reconstructed and up-sampled using a 6-tap H.264/AVC filter for the lost enhancement layer frame. In addition, a new intra-layer method was introduced in [18]. (5) Motion copy (MC): The reconstruction of the last key frame is re-used as the reference. Motion vectors are re-generated by copying the motion field of the last key frame. Single-layer EC methods include FC, TD and MC, while inter-layer EC methods include BLSkip and RU. The experimental results in [18] concluded that the BLSkip-based method is a desirable SVC EC tool.

4.1.2 Related Work

Motion vector error concealment has been an active research area for many years. A block-based motion vector extrapolation (MVE) method was proposed in [139].

Some MVs of correlated MBs in the previous frame are first extrapolated to the current damaged frame and then the lost MV of the damaged MB is replaced by the best MV of the motion extrapolated MB with the largest overlapped area. A pixel-based MVE (PMVE) method was introduced [140] by extending the block-based MVE method [139] to the pixel level. A hybrid MVE (HMVE) scheme was proposed in [141] based on the pixel-based and block-based MVE, which is able to discard the wrongly extrapolated MVs in order to obtain more accurate MV. In [142], a block-based motion projection (MP) approach was proposed to reconstruct the lost MV of the damaged block based on its qualified temporal blocks' MVs and spatial neighbors' MVs. In general, block-based MVE and MP methods are similar in terms of that they all used MVs from the projected blocks in previous frame and select the best MV of the block with the largest overlapped area. But MP employs a post-processing stage and median filtering is capable of refining the reconstructed MV field.

The visual quality of the error concealed regions can be further improved with the help of slice interleaving. It is aimed at spreading contiguous slices over different packets against packet losses, so that damaged regions can be surrounded by some correctly received regions. A simple slice interleaving approach was used in [131], where each slice consists of disjoint single lines of macroblocks in a frame. In [128], a packet interleaver was presented to interleave the packets before transmission and cope with burst packet losses, where packets are first loaded into the block interleaver in rows and are transmitted by columns. A distance-based slice interleaving method [143] was proposed to rearrange independently decodable slices of consecutive frames into packets according to an optimal interleaving structure for packetization. Each slice is interleaved by achieving the maximum minimal distance between contiguous slices.

4.1.3 Proposed Error Concealment Methods

In burst packet loss environments three inter-layer error concealment methods are proposed using two new approaches: (1) adaptively averaging over multiple types of motion vectors in different layers and (2) slice interleaving by an optimum ordering technique.

Motion Vector Averaging

We propose a new inter-layer motion vector averaging approach to reconstruct lost motion vectors. It uses a 4x4 block for the base layer and an 8x8 block for the enhancement layer as the basic concealment units. As shown in Figure 4.1, this inter-layer motion vector averaging approach exploits the spatial and temporal correlations of motion vectors between the two layers (co-located motion vectors MV_e^{BL} and $MV_{o/e}^{EL}$, where MV_o and MV_e denote motion vectors for a specific odd and even frame number respectively) and also uses a predictive motion vector MV_{Pred}^{EL} and a median motion vector $MV_{Med}^{EL/BL}$. MV_{Pred}^{EL} is a weighted average of the motion vectors of four projection-overlapped blocks in a reference frame f_r^{EL} and each weight $w(i)$ is the ratio of the size of each overlapped portion to the projection block size. $MV_{Med}^{EL/BL}$ is obtained based on the MVE [139] estimated ($MV_{MVE}^{EL/BL}$) and its neighbors' ($MV_{Nb}^{EL/BL}$) motion vectors in the same EL/BL frame $f_c^{EL/BL}$ respectively. Our method recovers a lost motion vector in one layer by adaptively averaging over multiple types of motion vectors in two layers using a multi-hypothesis parameter $\alpha \in [0, 1]$. Note that $\lfloor * \rceil$ represents the rounding function of $*$ to the nearest integer, s denotes the s-neighborhood adjoining blocks $s \in \{4, 8\}$, and $MV_{Med} = Median\{MV(k)\} = (Median\{MV^x(k)\}, Median\{MV^y(k)\}) = (MV_{Med}^x, MV_{Med}^y)$ for $k \in \{1, 2, \cdots, s\}$.

Base Layer (BL): The lost motion vector MV_e^{BL} in the BL current frame f_c^{BL} can be recovered in two cases. In case 1, if MV_e^{BL} is lost but MV_e^{EL} is correctly received, MV_e^{BL} can be reconstructed by adaptively averaging over two synthetic motion vectors. One is an aggregative motion vector by combining an approximate

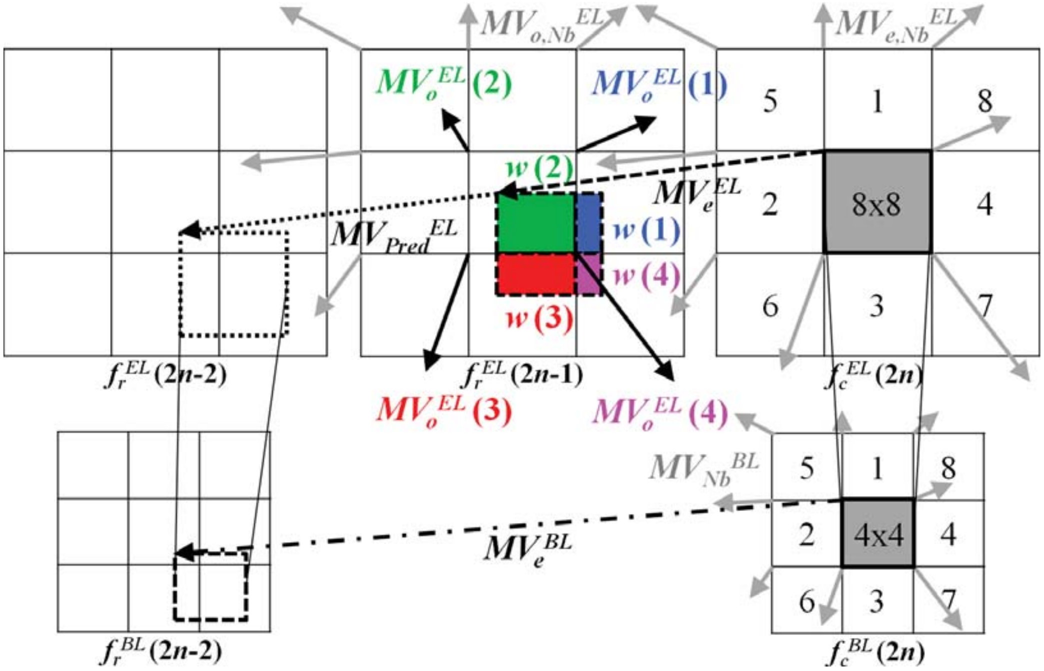

Fig. 4.1. The proposed inter-layer motion vector averaging approach using adaptively averaging over multiple types of motion vectors in two layers.

motion vector $\frac{1}{2}MV_e^{EL}$ in the EL corresponding frame f_c^{EL} and a predictive motion vector $\frac{1}{2}MV_{Pred}^{EL}$ in the EL reference frame f_r^{EL}. The other is a median motion vector MV_{Med}^{BL} based on the MVE estimated and s neighbors' motion vectors in the same BL frame. In case 2, if MV_e^{EL} and MV_e^{BL} are both lost, MV_e^{BL} can be reconstructed using the median median motion vector MV_{Med}^{BL} in the same BL frame.

BL Case 1: If MV_e^{BL} is lost but MV_e^{EL} is correctly received,

$$MV_e^{BL} = \lfloor \alpha(\frac{1}{2}MV_e^{EL} + \frac{1}{2}MV_{Pred}^{EL}) + (1-\alpha)MV_{Med}^{BL} \rceil, \tag{4.1}$$

$$MV_{Pred}^{EL} = \sum_i w(i) * MV_o^{EL}(i) / \sum_i w(i), \tag{4.2}$$

$$MV_{Med}^{BL} = Median\{MV_{MVE}^{BL} \bigcup MV_{Nb}^{BL}(k)\}. \tag{4.3}$$

BL Case 2: If MV_e^{BL} and MV_e^{EL} are both lost,

$$MV_e^{BL} = MV_{Med}^{BL}. \tag{4.4}$$

Enhancement Layer (EL): The lost motion vector $MV_{o/e}^{EL}$ in the EL current frame f_c^{EL} can be reconstructed in two cases, where $MV_{o/e}^{EL}$ denotes either MV_o^{EL} or MV_e^{EL} for a specific odd or even frame number. In case 1, if $MV_{o/e}^{EL}$ is lost but MV_e^{BL} is correctly received, $MV_{o/e}^{EL}$ can be recovered by adaptively averaging over two synthetic motion vectors. One is an approximate motion vector $2 * \frac{1}{2} MV_e^{BL} = MV_e^{BL}$ in BL corresponding frame f_c^{BL}. The other is a median motion vector $MV_{o/e,Med}^{EL}$ based on the MVE estimated and s neighbors' motion vectors in the same EL odd/even frame. In case 2, if MV_e^{BL} and $MV_{o/e}^{EL}$ are both lost, $MV_{o/e}^{EL}$ can be recovered using the median motion vector $MV_{o/e,Med}^{EL}$ in the same EL odd/even frame.

EL Case 1: If $MV_{o/e}^{EL}$ is lost but MV_e^{BL} is correctly received,

$$MV_{o/e}^{EL} = \lfloor \alpha MV_e^{BL} + (1-\alpha) MV_{o/e,Med}^{EL} \rceil, \tag{4.5}$$

$$MV_{o/e,Med}^{EL} = Median\{MV_{MVE}^{EL} \bigcup MV_{o/e,Nb}^{EL}(k)\}. \tag{4.6}$$

EL Case 2: If $MV_{o/e}^{EL}$ and MV_e^{BL} are both lost,

$$MV_{o/e}^{EL} = MV_{o/e,Med}^{EL}. \tag{4.7}$$

Slice Interleaving

In order to improve the performance against burst packet losses and reduce error propagation across multiple frames, a new slice interleaving approach is developed to make the average distance between two contiguous slices as far as possible. The slice tool can be used at the encoder to generate independently decodable slices with the cost of some loss in coding efficiency. The main idea of this approach is to rearrange the slices according to a predefined interleaving structure, which would be designed in such a way that the contiguous slices are distributed as far as possible. In [144], an optimum ordering technique was developed for dispersed-dot ordered dithering for halftone image processing. The method was used for obtaining the optimum index for adding dots to lattices. The optimum index matrix is a square matrix and devised with a simple rule: First, fill each cell of the matrix with a successive integer (e.g.

starting from 1 in raster scanning order). Second, reorder them such that the average distance between two successive numbers is as far as possible in the matrix. It can be rotated or mirrored without affecting the property of maximizing average distance. The optimum index matrix can be defined recursively and three concrete examples are illustrated in Figure 4.2.

$$A_2 = \begin{bmatrix} 1 & 4 \\ 3 & 2 \end{bmatrix}, A_{2n} = \begin{bmatrix} 4 \times A_n - 3 & 4 \times A_n \\ 4 \times A_n - 1 & 4 \times A_n - 2 \end{bmatrix}. \tag{4.8}$$

$$\begin{bmatrix} 1 & 4 \\ 3 & 2 \end{bmatrix}$$

(a)

$$\begin{bmatrix} 1 & 13 & 4 & 16 \\ 9 & 5 & 12 & 8 \\ 3 & 15 & 2 & 14 \\ 11 & 7 & 10 & 6 \end{bmatrix}$$

(b)

$$\begin{bmatrix} 1 & 49 & 13 & 61 & 4 & 52 & 16 & 64 \\ 33 & 17 & 45 & 29 & 36 & 20 & 48 & 32 \\ 9 & 57 & 5 & 53 & 12 & 60 & 8 & 56 \\ 41 & 25 & 37 & 21 & 44 & 28 & 40 & 24 \\ 3 & 51 & 15 & 63 & 2 & 50 & 14 & 62 \\ 35 & 19 & 47 & 31 & 34 & 18 & 46 & 30 \\ 11 & 59 & 7 & 55 & 10 & 58 & 6 & 54 \\ 43 & 27 & 39 & 23 & 42 & 26 & 38 & 22 \end{bmatrix}$$

(c)

Fig. 4.2. Optimum index matrixes of different size.

We propose a new slice interleaving approach for a set of contiguous slices in a group of pictures (GOP) using the optimum ordering technique described above. The number of contiguous slices in one frame is designed to be equal to the number of consecutive frames in a GOP, hence a set of contiguous slices in a GOP can be represented by a square matrix. Figure 4.3 illustrates an example of slice interleaving with an 8x8 optimum index matrix for a set of 64 contiguous slices among 8 consecutive frames in a GOP. The frame numbers of a group of consecutive frames are denoted in a temporally ascending order along the horizontal axis. The slice numbers of a set of contiguous slices, which are labeled by successive integers, are denoted in a spatially ascending order along the vertical axis. Contiguous slices in one frame are rearranged into disjoint positions by maximizing the average distance between each other. Each frame consists of a few independently decodable slices and each slice is encapsuled in a network abstraction layer unit (NALU). Slice interleaving is performed by a square interleaver on a set of NALUs containing contiguous slices after initial placement. Each NALU containing a single slice is interleaved according to the optimum index matrix and then packetized in raster scan order.

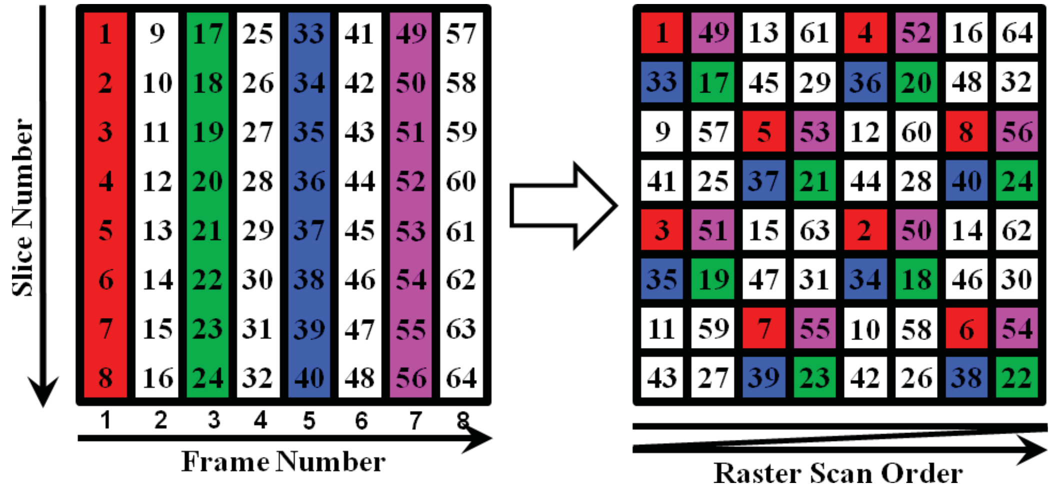

1	9	17	25	33	41	49	57
2	10	18	26	34	42	50	58
3	11	19	27	35	43	51	59
4	12	20	28	36	44	52	60
5	13	21	29	37	45	53	61
6	14	22	30	38	46	54	62
7	15	23	31	39	47	55	63
8	16	24	32	40	48	56	64

1	49	13	61	4	52	16	64
33	17	45	29	36	20	48	32
9	57	5	53	12	60	8	56
41	25	37	21	44	28	40	24
3	51	15	63	2	50	14	62
35	19	47	31	34	18	46	30
11	59	7	55	10	58	6	54
43	27	39	23	42	26	38	22

Fig. 4.3. The proposed slice interleaving scheme in a GOP (8 frames).

Similarly, flexible macroblock ordering (FMO) is capable of distributing adjoining macroblock errors to the entire frame as equally as possible to avoid error accumulation in a certain region. The FMO tool can be used at the encoder to assign each macroblock of a frame to a certain slice group by a macroblock allocation map (MBAmap), which requires additional computation and causes some loss in coding efficiency. For further comparison, FMO Type 1 [132] is used to generate two slice groups and each one contains four independently dispersed slices (totally 8 slices per frame), which is complied with our proposed slice interleaving approach.

4.2 System Implementation

A two-layer spatial-temporal scalable video coding (SVC) system was developed based on JSVM 9.8 [145], which was the last version officially supporting error concealment tools. Sixty-four independently decodable slices in a GOP (8 frames in BL and EL separately) are interleaved using the 8x8 optimum index matrix in Figure 4.3 at the encoder and correspondingly de-interleaved at the decoder. Each interleaved slice was encapsulated into a single NALU during packetization. The parameters and syntax elements of the 8x8 optimum index matrix and FMO Type 1 are independently encoded into a picture parameter set (PPS) and transmitted to the decoder. The extra bits used for encoding these information were counted in the total bitrates. We modified the JSVM reference decoder to deal with lost NALUs and conceal damaged frames. It is able to manage the order of the NALUs received at decoder and identify the decoding information of the layer and slice in the received NALUs. Similar to [146], a block-based status map is developed for each layer to inform the decoder to decode available blocks and conceal lost blocks. The status map is reinitialized at the beginning of decoding each slice.

Burst packet losses were simulated by removing NALUs from the encoded SVC bitstreams based on random burst packet losses at different rates. Gilbert's two-state Markov model [147, 148] was used to independently generate random burst packet loss patterns. This model can reasonably approximate Internet transmission [17]. In the good state G, all packets are correctly received, while in the bad state B, all packets are lost. Two transition probabilities, p_{GB} for going from G to B and p_{BG} for going from B to G, are sufficient to define the model. Moreover, other two quantities are preferred to use: average burst packet loss probability $P_B = Pr(B) = p_{GB}/(p_{GB} + p_{BG})$, the same as the well-defined burst packet loss rate (BPLR), and average burst packet loss length $L_B = 1/p_{BG}$. The network simulation parameters are defined using a pair (P_B, L_B). In our experiments, SVC video transmission over burst packet loss channels are simulated in two scenarios: first corresponding to

$(P_B, L_B) = (10\%, 5)$ and second corresponding to $(P_B, L_B) = (20\%, 4)$. Damaged frame are recovered by different error concealment methods, including three proposed inter-layer methods using the two new approaches and FMO described above, i.e. (1) motion vector averaging (MVAvg), (2) motion vector averaging and slice interleaving (MVAvg+SliceIntlv) and (3) motion vector averaging, slice interleaving and FMO (MVAvg+SliceIntlv+FMO), and two existing methods, i.e. (4) motion copy (MC) [18] and (5) motion projection (MP) [142]. Because the original MC and MP methods are developed for single-layer error concealment, the BLSkip-based extensions [18] of the two methods are developed for inter-layer EC.

4.3 Experimental Results

Three video sequences with 300 frames, i.e. *Bus*, *Football* and *Foreman*, were used to test our SVC system. The *Bus* sequence contains slow and homogenous motion while the *Football* sequence has fast and chaotic motion. The *Foreman* sequence involves normal motion and scene changes. Our experiments used the same quantization parameter (QP) for encoding BL and EL frames (QP=28, 32, 36 and 40) to evaluate different error concealment methods, running on a Linux desktop with a 2.8 GHz Quad-core CPU and 4 GB RAM. The frame coding structure was "IPP$\cdots$" with I-frame refresh after 2 successive P-frame GOPs in BL and 4 successive P-frame GOPs in EL. For low complexity, we constantly set the parameter $\alpha = 0.5$ and employed the 4-neighborhood of adjoining blocks $s = 4$. The average PSNR value of the Y component (Y-PSNR) of damaged frames was used as an objective visual quality measurement. The Y-PSNR was obtained by averaging the results of 50 random burst packet loss patterns at each BPLR to ensure statistical significance of the results. Each burst packet loss pattern has 20 temporally circular shifts across the entire frames, in total 20×50=1000 realizations of burst packet losses at a BPLR.

Table 4.1 demonstrates the average decoding time per frame of the existing and proposed error concealment methods. The results show that the computational time of the proposed MVAvg method is slightly longer than the MP and MC method. It can be observed that the decoding delay (time difference between MVAvg-based methods) caused by slice de-interleaving is relatively shorter than that introduced by FMO.

The Y-PSNR of the first 60 frames of BL and EL *Football* sequence are illustrated in Figure 4.4 and 4.5 with two concrete burst packet loss patterns at BPLR 10% and 20%, where the vertical dash lines indicate the damaged frames where burst packet losses occurred. The visual quality in the enhancement layer is recovered slightly faster than that in the base layer and the Y-PSNR drop in the enhancement layer is comparatively smaller than that in the base layer. Visual distortion due to poorly

Table 4.1
Average Decoding Time per Frame of the Existing and Proposed Error Concealment Methods (in Milliseconds)

	Bus	*Football*	*Foreman*
Motion Copy (MC)	16.36	16.59	16.25
Motion Projection (MP)	17.33	17.82	17.14
MVAvg	17.94	18.53	17.68
MVAvg+SliceIntlv	19.95	20.60	19.72
MVAvg+SliceIntlv+FMO	24.08	24.76	23.87

concealed motion vectors is barely observed in the proposed three methods, except for fast moving objects.

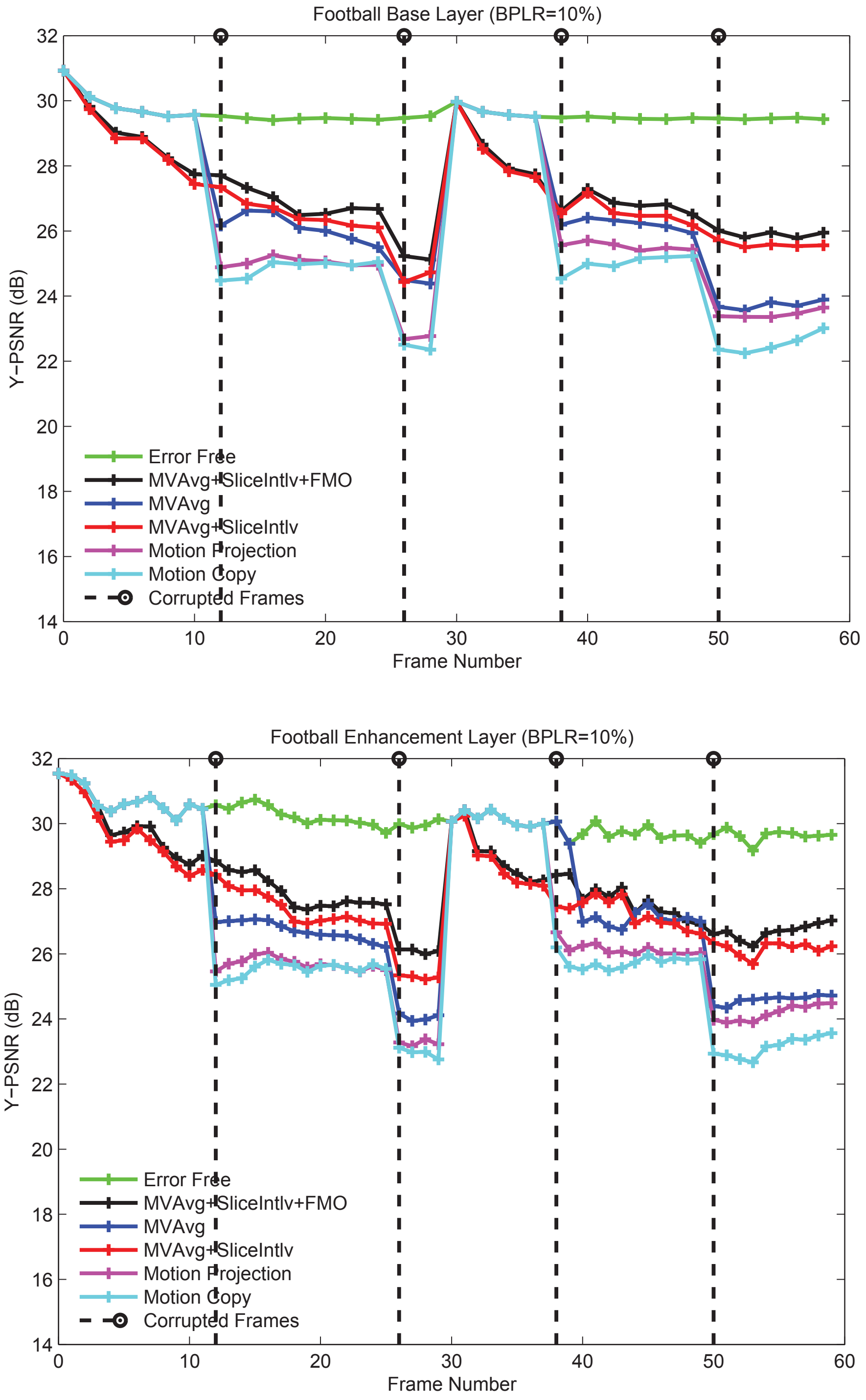

Fig. 4.4. Y-PSNR of the *Football* BL & EL frames (BPLR=10%).

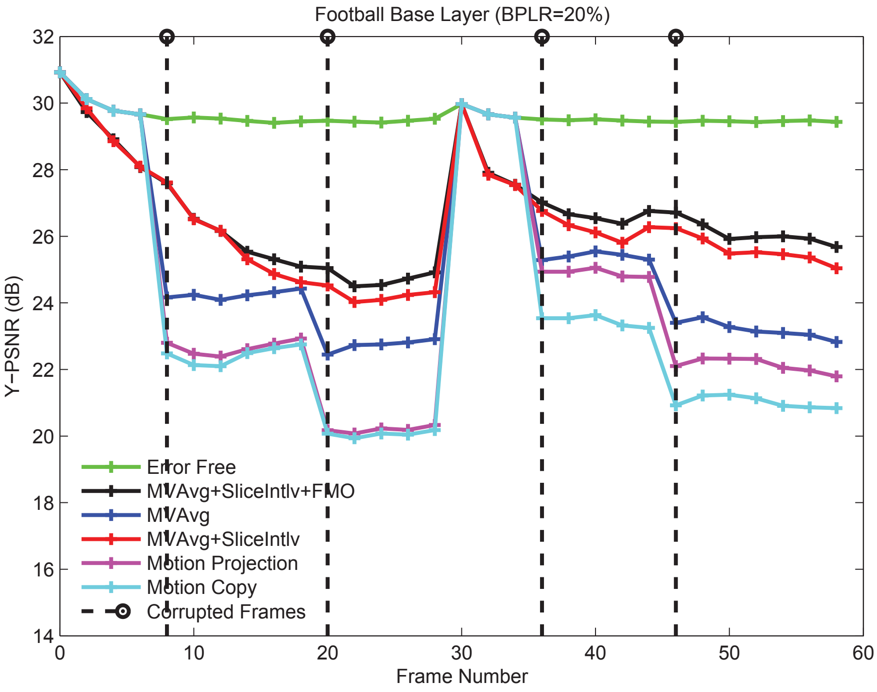

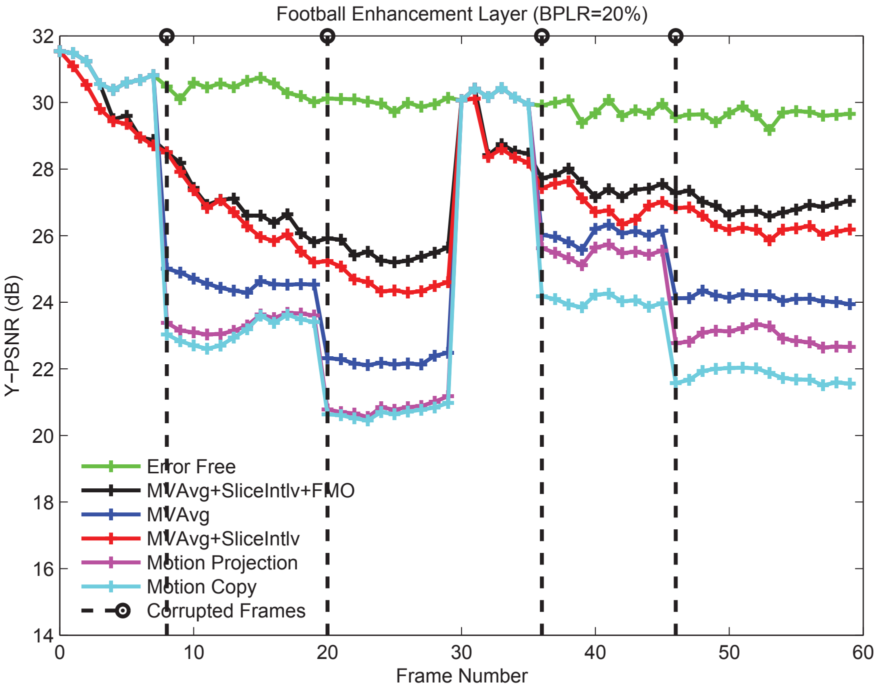

Fig. 4.5. Y-PSNR of the *Football* BL & EL frames (BPLR=20%).

Compared with the perfect reconstruction from the error-free channel, the operational rate-distortion (RD) plots for various error concealment methods are shown in Figure 4.6, 4.7 and 4.8. The proposed MVAvg method based on motion vector averaging is more effective than two existing methods in reducing the visual quality degradation caused by burst packet losses and error propagation. The RD plots illustrate that the Y-PSNR of the proposed MVAvg method is 0.9dB-3.2dB higher than the existing MC method and is 0.3dB-2.1dB higher than the existing MP method. The proposed MVAvg+SliceIntlv+FMO and MVAvg+SliceIntlv methods outperform the other methods in significantly improving the visual quality. In fact, the RD plots of the two methods are very close at low bitrate and low BPLR. The MVAvg+SliceIntlv+FMO method is superior to the MVAvg+SliceIntlv method only at high bitrate and high BPLR, because additional bit overhead for encoding FMO information undermines the coding efficiency at low bitrate. Therefore, considering the tradeoff between complexity and performance, The the proposed MVAvg+SliceIntlv method is more suitable for low burst packet loss channel.

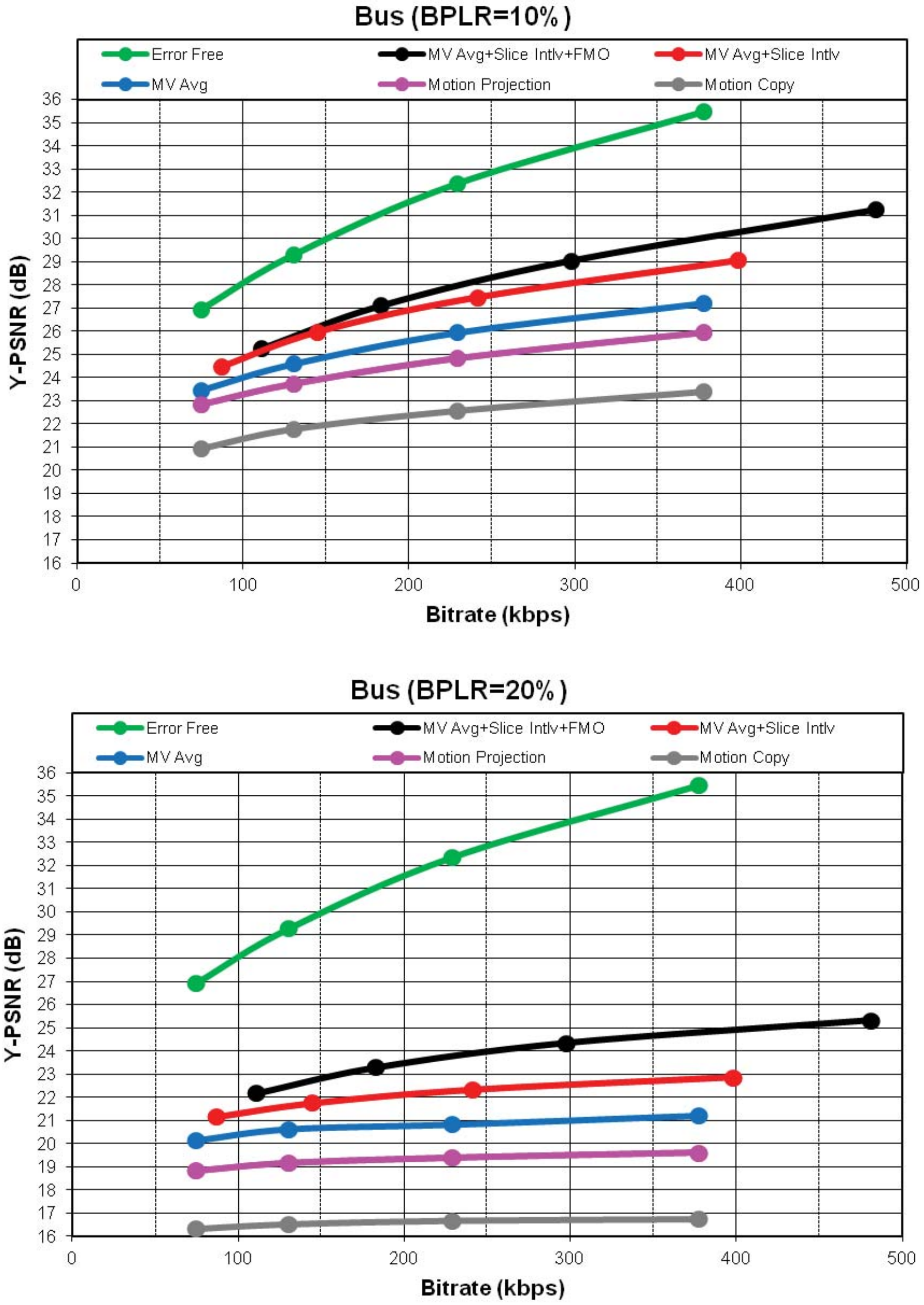

Fig. 4.6. Rate-Distortion of the *Bus* sequence (BPLR=10%, 20%).

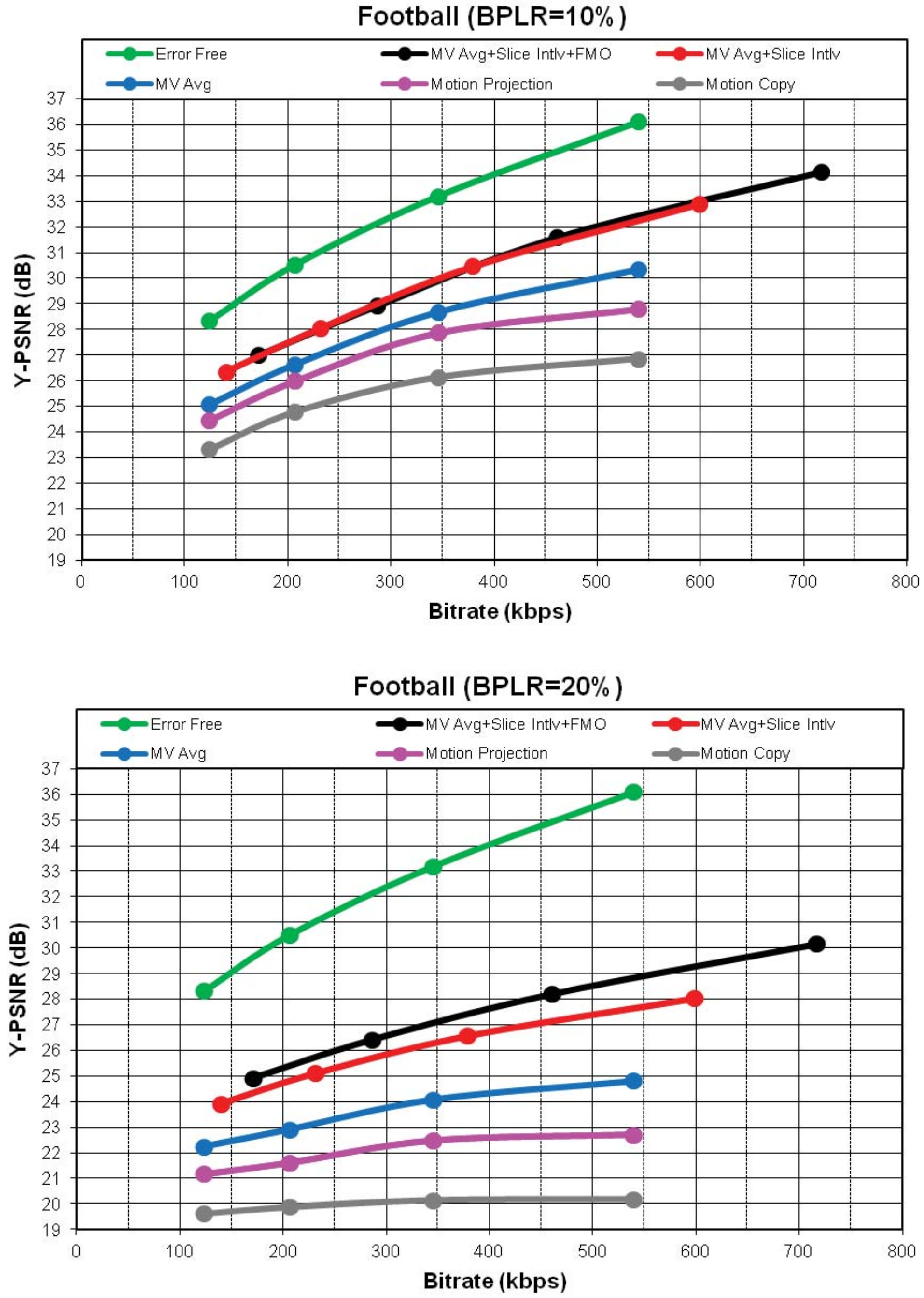

Fig. 4.7. Rate-Distortion of the *Football* sequence (BPLR=10%, 20%).

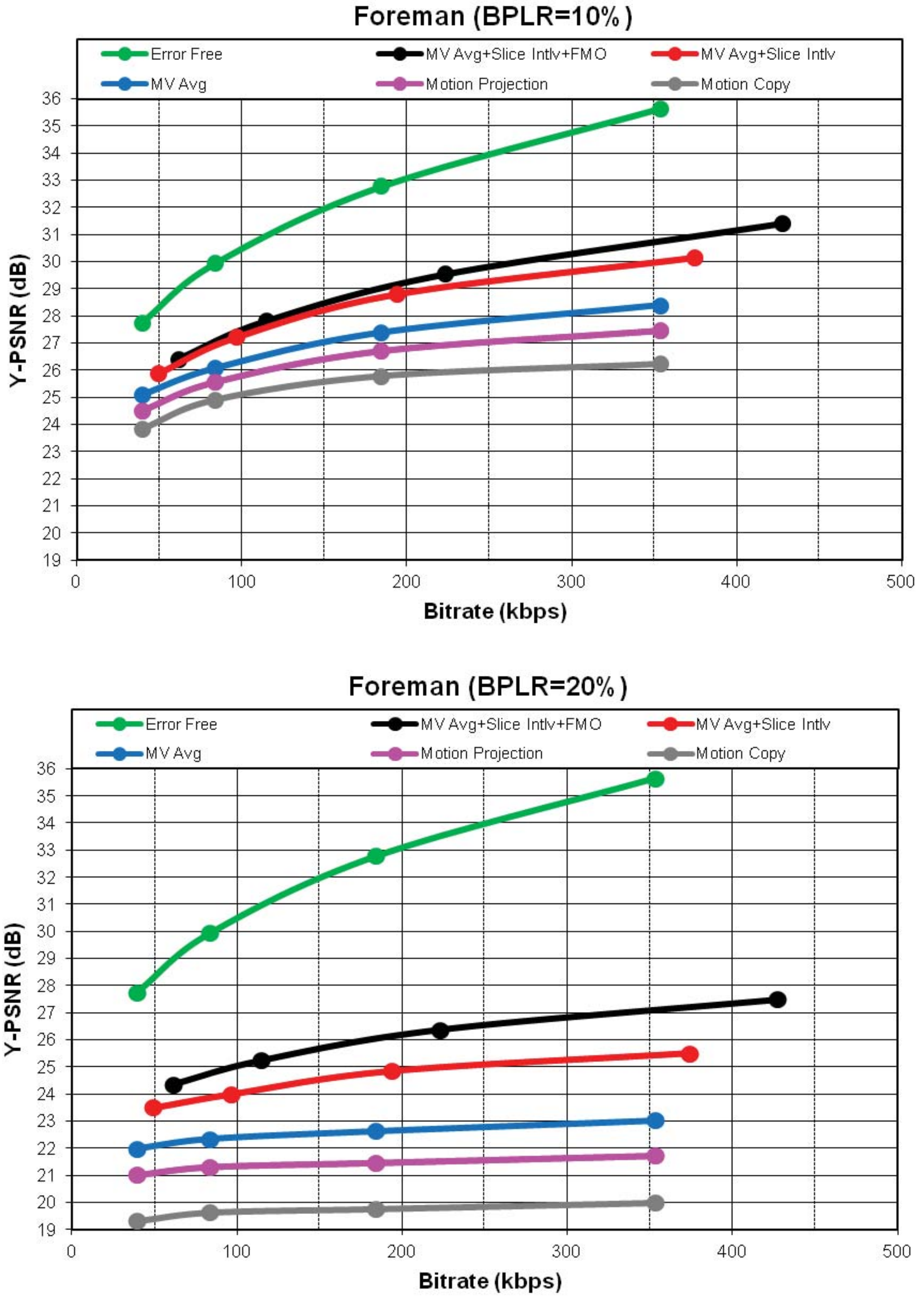

Fig. 4.8. Rate-Distortion of the *Foreman* sequence (BPLR=10%, 20%).

5. CONCLUSIONS AND FUTURE WORK

5.1 Conclusions

In this thesis we describe several visual saliency models in the frequency domain in Chapter 2, a hazmat sign image analysis system (MERGE) using visual saliency for location detection and content recognition in Chapter 3, and several error concealment methods for scalable video coding (SVC) in chapter 4.

For visual saliency models in the frequency domain, we develop separate and composite visual saliency model families for frequency domain visual saliency models. We propose six visual saliency models based on new spectrum processing methods and an entropy-based saliency map selection approach. We propose an entropy-based saliency map selection approach to select a "good" final saliency map among the set of map candidates. A group of extended saliency models that extends each proposed visual saliency models are also developed by incorporating both separate and composite model families and using variant color spaces. Experimental results show that the six best extended models are more accurate and efficient than most state-of-the-art models in predicting eye fixation on standard image datasets.

For hazmat sign image analysis system (MERGE), we develop hazmat sign location detection and content recognition methods based on visual saliency. We use the one of our proposed frequency domain models to extract salient regions that are likely to contain hazmat sign candidates and then use a Fourier descriptor based contour matching method to locate the border of hazmat signs in these regions. This visual saliency based approach is able to increase the accuracy of sign location detection, significantly reduce the number of false positives, and speed up the image analysis process. This approach improves the accuracy of existing methods presented in [14, 15]. We also propose a color recognition method to interpret the color inside the detected hazmat signs. Our three image datasets consists of images taken in the working field and outdoor field under variant lighting and weather conditions, distances, and perspectives.

For error concealment for scalable video coding (SVC), we develop two error concealment approaches robust to burst packet losses, i.e. inter-layer motion vector averaging and slice interleaving using optimum ordering. A two-layer spatial-temporal scalable video coding system are decribed to evaluate the existing and proposed error concealment methods. Experimental results confirmed that the proposed error concealment methods outperform two existing methods in reducing the impact of burst packet losses and error propagation.

The main contributions of visual saliency models in the frequency domain are:

- We investigate bottom-up visual saliency using spectral analysis approaches.
- We develop separate and composite visual saliency model families for frequency domain models.
- We propose six visual saliency models based on different spectrum processing.
- We propose an entropy-based saliency map selection approach.
- We develop an evaluation tool for benchmarking visual saliency models.

The main contributions of image analysis system for hazmat sign detection and recognition are:

- We develop a hazmat sign location detection and content recognition system using visual saliency.
- We used one of our proposed frequency domain models to extract salient regions.
- We developed a Fourier descriptor based contour matching method to locate the border of hazmat signs.

- We proposed a color recognition method to interpret the color inside the detected hazmat signs.
- We collected three hazmat sign image datasets.

The main contributions of error concealment methods for SVC are:

- We investigated the impact of burst packet loss and error propagation in base and enhancement layers.
- We explored inter-layer spatial and temporal correlations for error concealment against burst packet loss.
- We proposed two error concealment methods to enhance error recovery and visual quality:
- (1) Inter-layer motion vector averaging
- (2) Slice interleaving using optimum ordering
- We developed a two-layer spatial-temporal scalable video coding system for evaluation.

5.2 Future Work

Our long term goal for MERGE is to develop a hazmat sign image analysis system capable of automatically recognizing hazmat signs from images acquired up to 300 feet and providing real-time guide information to first responders to identify the hazardous materials and determine what specialty equipment, procedures and precautions should be taken in the event of an emergency.

One problem is the overall accuracy of our hazmat sign image analysis methods. The accuracy needs to be improved. This can be done by improving our current sign location detection approach and developing more robust color recognition techniques. We may be able to use supper-resolution image reconstruction methods [126, 127] to refine the hazmat sign images. It can improve the location detection accuracy at even longer distances and it is more useful for blurred and low resolution hazmat signs. We can also employ proper color calibration [51]. This can help the color recognition technique to recognize colored hazmat signs more accurately. One could also use character recognition methods to interpret the text inside the detected hazmat signs when the image resolution is relatively high.

For visual saliency models in the frequency domain, one direction of future work is testing our proposed visual saliency models using more eye fixation image datasets. One could also study the tradeoff between accuracy and speed of the proposed frequency domain saliency models for practical applications. Another direction is combining several saliency models to achieve better accuracy of predicting eye fixation and hazmat sign image analysis.

For error concealment for scalable video coding (SVC), one direction of future work is testing our proposed error concealment models on high resolution video sequences.

5.3 Publications Resulting from This Work

Conference Papers

1. **Bin Zhao** and Edward J. Delp, "Visual Saliency Models Based on Spectrum Processing," *Proceedings of the IEEE Winter Conference on Applications of Computer Vision*, Waikoloa Beach, HI, USA, January 2015. (Accepted)

2. **Bin Zhao**, Albert Parra, and Edward J. Delp, "Mobile-Based Hazmat Sign Detection and Recognition," *Proceedings of the IEEE Global Conference on Signal and Information Processing*, no. 6736996, pp. 735-738, Austin, TX, USA, December 2013. (Invited Paper)

3. **Bin Zhao** and Edward J. Delp, "Inter-layer Error Concealment for Scalable Video Coding," *Proceedings of the IEEE International Conference on Multimedia and Expo*, no. 6607539, pp. 1-6, San Jose, CA, USA, July 2013.

4. **Bin Zhao**, "Interleaving-Based Error Concealment for Scalable Video Coding System," *Proceedings of the IEEE Visual Communications and Image Processing Conference*, no. 6115965, pp. 1-4, Tainan City, Taiwan, November 2011.

5. Albert Parra, **Bin Zhao**, Joonsoo Kim, and Edward J. Delp, "Recognition, Segmentation and Retrieval of Gang Graffiti Images on a Mobile Device," *Proceedings of the IEEE International Conference on Technologies for Homeland Security*, no. 6698996, pp. 178-183, Waltham, MA, USA, November 2013.

6. Albert Parra, **Bin Zhao**, Andrew Haddad, Mireille Boutin, and Edward J. Delp, "Hazardous Material Sign Detection and Recognition," *Proceedings of the IEEE International Conference on Image Processing*, no. 6738544, pp. 2640-2644, Melbourne, Australia, September 2013.

Journal Papers

1. **Bin Zhao** and Edward J. Delp, "Biologically-Inspired Visual Saliency Models Using Spectrum Processing," in preparation.

2. **Bin Zhao**, Albert Parra, and Edward J. Delp, "Hazmat Sign Detection and Recognition Using Visual Saliency," in preparation.

LIST OF REFERENCES

LIST OF REFERENCES

[1] ERG, available: http://www.phmsa.dot.gov/hazmat/library/erg.

[2] L. Itti, “Models of bottom-up and top-down visual attention,” Ph.D. dissertation, California Institute of Technology, 2000.

[3] C. Koch and S. Ullman, “Shifts in selective visual attention: Towards the underlying neural circuitry,” *Human Neurobiology*, vol. 4, no. 4, pp. 219–227, April 1985.

[4] A. M. Treisman and G. Gelade, “A feature-integration theory of attention,” *Cognitive Psychology*, vol. 12, no. 1, pp. 97–136, January 1980.

[5] J. M. Wolfe, “Guided search 2.0 A revised model of visual search,” *Psychonomic Bulletin & Review*, vol. 1, no. 2, pp. 202–238, 1994.

[6] J. M. Wolfe and T. S. Horowitz, “What attributes guide the deployment of visual attention and how do they do it?” *Nature Reviews Neuroscience*, vol. 5, no. 6, pp. 495–501, June 2004.

[7] S. Frintrop, E. Rome, and H. I. Christensen, “Computational visual attention systems and their cognitive foundations: A survey,” *ACM Transactions on Applied Perception*, vol. 7, no. 1, pp. 6:1–6:39, January 2010.

[8] A. Toet, “Computational versus psychophysical bottom-up image saliency: A comparative evaluation study,” *IEEE Transactions on Pattern Analysis and Machine Intelligence*, vol. 33, no. 11, pp. 2131–2146, November 2011.

[9] A. Borji and L. Itti, “State-of-the-art in visual attention modeling,” *IEEE Transactions on Pattern Analysis and Machine Intelligence*, vol. 35, no. 1, pp. 185–207, January 2013.

[10] A. Borji, D. N. Sihite, and L. Itti, “Quantitative analysis of human-model agreement in visual saliency modeling: A comparative study,” *IEEE Transactions on Image Processing*, vol. 22, no. 1, pp. 55–69, January 2013.

[11] United States Department of Transportation, *Code of Federal Regulations, Title 49 - Transportation*, 2012nd ed., October 2012.

[12] WISER, available: http://wiser.nlm.nih.gov.

[13] MERGE, available: http://www.hazmat-signs.org.

[14] B. Zhao, A. Parra, and E. J. Delp, “Mobile-based hazmat sign detection system,” *Proceedings of the IEEE Global Conference on Signal and Information Processing*, pp. 735–738, December 2013, Austin, TX, USA.

[15] A. Parra, B. Zhao, A. Haddad, M. Boutin, and E. J. Delp, “Hazardous material sign detection and recognition,” *Proceedings of the IEEE International Conference on Image Processing*, pp. 2640–2644, September 2013, Melbourne, Australia.

[16] H. Schwarz, D. Marpe, and T. Wiegand, “Overview of the scalable video coding extension of the H.264/AVC standard,” *IEEE Transactions on Circuits and Systems for Video Technology*, vol. 17, no. 9, pp. 1103–1120, September 2007.

[17] K. Stuhlmüller, N. Farber, M. Link, and B. Girod, “Analysis of video transmission over lossy channels,” *IEEE Journal on Selected Areas in Communications*, vol. 18, no. 6, pp. 1012–1032, June 2000.

[18] Y. Guo, Y. Chen, Y.-K. Wang, H. Li, M. M. Hannuksela, and M. Gabbouj, “Error resilient coding and error concealment in scalable video coding,” *IEEE Transactions on Circuits and Systems for Video Technology*, vol. 19, no. 6, pp. 781–795, June 2009.

[19] C. Christopoulos, A. Skodras, and T. Ebrahimi, “The JPEG2000 still image coding system: An overview,” *IEEE Transactions on Consumer Electronics*, vol. 46, no. 4, pp. 1103–1127, November 2000.

[20] L. Itti, “Automatic foveation for video compression using a neurobiological model of visual attention,” *IEEE Transactions on Image Processing*, vol. 13, no. 10, pp. 1304–1318, October 2004.

[21] S. Avidan and A. Shamir, “Seam carving for content-aware image resizing,” *ACM Transactions on Graphics*, vol. 26, no. 3, pp. 1–9, July 2007.

[22] J. Han, K. N. Ngan, M. Li, and H. Zhang, “Unsupervised extraction of visual attention objects in color images,” *IEEE Transactions on Circuits and Systems for Video Technology*, vol. 16, no. 1, pp. 141–145, January 2006.

[23] D. Walther and C. Koch, “Modeling attention to salient proto-objects,” *Neural Networks*, vol. 19, no. 9, pp. 1395–1407, November 2006.

[24] A. Mogelmose, M. M. Trivedi, and T. B. Moeslund, “Vision-based traffic sign detection and analysis for intelligent driver assistance systems: Perspectives and survey,” *IEEE Transactions on Intelligent Transportation Systems*, vol. 13, no. 4, pp. 1484–1497, December 2012.

[25] L. Itti, C. Koch, and E. Niebur, “A model of saliency-based visual attention for rapid scene analysis,” *IEEE Transactions on Pattern Analysis and Machine Intelligence*, vol. 20, no. 11, pp. 1254–1259, November 1998.

[26] J. Harel, C. Koch, and P. Perona, “Graph-based visual saliency,” *Proceedings of the Annual Conference on Neural Information Processing Systems*, pp. 545–552, December 2006, Vancouver, BC, Canada.

[27] N. D. B. Bruce and J. K. Tsotsos, “Saliency, attention, and visual search: An information theoretic approach,” *Journal of Vision*, vol. 9, no. 3, pp. 1–24, March 2009.

[28] X. Hou and L. Zhang, “Dynamic visual attention: Searching for coding length increments,” *Proceedings of the Annual Conference on Neural Information Processing Systems*, pp. 681–688, December 2008, Vancouver, BC, Canada.

[29] R. Achanta, S. Hemami, F. Estrada, and S. Susstrunk, "Frequency-tuned salient region detection," *Proceedings of the IEEE Conference on Computer Vision and Pattern Recognition*, pp. 1597–1604, June 2009, Miami, FL, USA.

[30] C. Guo, Q. Ma, and L. Zhang, "Spatio-temporal saliency detection using phase spectrum of quaternion Fourier transform," *Proceedings of the IEEE Conference on Computer Vision and Pattern Recognition*, pp. 1–8, June 2008, Anchorage, AK, USA.

[31] C. Guo and L. Zhang, "A novel multiresolution spatiotemporal saliency detection model and its applications in image and video compression," *IEEE Transactions on Image Processing*, vol. 19, no. 1, pp. 185–198, January 2010.

[32] P. Bian and L. Zhang, "Visual saliency: A biologically plausible contourlet-like frequency domain approach," *Cognitive Neurodynamics*, vol. 4, no. 3, pp. 189–198, September 2010.

[33] X. Hou, J. Harel, and C. Koch, "Image signature: Highlighting sparse salient regions," *IEEE Transactions on Pattern Analysis and Machine Intelligence*, vol. 34, no. 1, pp. 194–201, January 2012.

[34] B. Schauerte and R. Stiefelhagen, "Predicting human gaze using quaternion DCT image signature saliency and face detection," *Proceedings of the IEEE Workshop on Applications of Computer Vision*, pp. 137–144, January 2012, Breckenridge, CO, USA.

[35] J. Li, M. D. Levine, X. An, X. Xu, and H. He, "Visual saliency based on scale-space analysis in the frequency domain," *IEEE Transactions on Pattern Analysis and Machine Intelligence*, vol. 35, no. 4, pp. 996–1010, April 2013.

[36] T. A. Ell, "Quaternion-Fourier transforms for analysis of two-dimensional linear time-invariant partial differential systems," *Proceedings of the IEEE Conference on Decision and Control*, vol. 2, pp. 1830–1841, December 1993, San Antonio, TX, USA.

[37] T. A. Ell and S. J. Sangwine, "Hypercomplex Fourier transforms of color images," *IEEE Transactions on Image Processing*, vol. 16, no. 1, pp. 22–35, January 2007.

[38] L. Zhang, M. H. Tong, T. K. Marks, H. Shan, and G. W. Cottrell, "SUN: A bayesian framework for saliency using natural statistics," *Journal of Vision*, vol. 8, no. 7, pp. 1–20, December 2008.

[39] Y. Fang, W. Lin, B.-S. Lee, C.-T. Lau, Z. Chen, and C.-W. Lin, "Bottom-up saliency detection model based on human visual sensitivity and amplitude spectrum," *IEEE Transactions on Multimedia*, vol. 14, no. 1, pp. 187–198, February 2012.

[40] Z. Li, "A saliency map in primary visual cortex," *Trends in Cognitive Sciences*, vol. 6, no. 1, pp. 9–16, January 2002.

[41] Z. Li and P. Dayan, "Pre-attentive visual selection," *Neural Networks*, vol. 19, no. 9, pp. 1437–1439, November 2006.

[42] C. A. Curcio, K. R. Sloan, R. E. Kalina, and A. E. Hendrickson, "Human photoreceptor topography," *The Journal of Comparative Neurology*, vol. 292, no. 4, pp. 497–523, February 1990.

[43] E. D. Montag, *Rods and Cones*, available: http://www.cis.rit.edu/people/faculty/montag/vandplite/pages/chap_9/ch9p1.html.

[44] C. Blakemore and F. W. Campbell, "On the existence of neurones in the human visual system selectively sensitive to the orientation and size of retinal images," *The Journal of Physiology*, vol. 203, no. 1, pp. 237–260, July 1969.

[45] D. Casasent and D. Psaltis, "New optical transforms for pattern recognition," *Proceedings of the IEEE*, vol. 65, no. 1, pp. 77–84, January 1977.

[46] P. Cavanagh, "Size and position invariance in the visual system," *Perception*, vol. 7, no. 2, pp. 167–177, 1978.

[47] ——, "Size invariance: Reply to Schwartz," *Perception*, vol. 10, no. 4, pp. 469–474, 1981.

[48] L. O. Harvey and V. V. Doan, "Visual masking at different polar angles in the two-dimensional Fourier plane," *Journal of the Optical Society of America A*, vol. 7, no. 1, pp. 116–127, January 1990.

[49] E. L. Schwartz, "Spatial mapping in the primate sensory projection: Analytic structure and relevance to perception," *Biological Cybernetics*, vol. 25, no. 4, pp. 181–194, 1977.

[50] ——, "Computational anatomy and functional architecture of striate cortex: A spatial mapping approach to perceptual coding," *Vision Research*, vol. 20, no. 8, pp. 645–669, 1980.

[51] H.-C. Lee, *Color Imaging Science*. Cambridge, UK: Cambridge University Press, 2005.

[52] M. D. Fairchild, *Color Appearance Models*. Chichester, UK: Wiley-IS&T, 2013.

[53] S. Süsstrunk, R. Buckley, and S. Swen, "Standard RGB color spaces," *Proceedings of the Color Imaging Conference: Color Science, Systems, and Applications*, pp. 127–134, November 1999, Scottsdale, AZ, USA.

[54] S. Engel, X. Zhang, and B. Wandell, "Colour tuning in human visual cortex measured with functional magnetic resonance imaging," *Nature*, vol. 388, no. 6637, pp. 68–71, July 1997.

[55] W. R. Hamilton, *Elements of Quaternions*. Dublin, Ireland: The University of Dublin Press, 1866.

[56] P. Bian and L. Zhang, "Biological plausibility of spectral domain approach for spatiotemporal visual saliency," *Proceedings of the International Conference Neuro-Information Processing*, vol. 5506, pp. 251–258, November 2008, Auckland, New Zealand.

[57] B. Schauerte and R. Stiefelhagen, "Quaternion-based spectral saliency detection for eye fixation prediction," *Proceedings of the European Conference on Computer Vision*, pp. 116–129, October 2012, Florence, Italy.

[58] W. Feng and B. Hu, "Quaternion discrete cosine transform and its application in color template matching," *Proceedings of the International Congress on Image and Signal Processing*, vol. 2, pp. 252–256, May 2008, Sanya, China.

[59] K. Castleman, *Digital Image Processing.* New York, USA: Prentice-Hall, 1996.

[60] A. V. Oppenheim and J. S. Lim, "The importance of phase in signals," *Proceedings of the IEEE*, vol. 69, no. 5, pp. 529–541, May 1981.

[61] M. H. Hayes, J. S. Lim, and A. V. Oppenheim, "Signal reconstruction from phase or magnitude," *IEEE Transactions on Acoustics, Speech and Signal Processing*, vol. 28, no. 6, pp. 672–680, December 1980.

[62] J. W. Cooley and J. W. Tukey, "An algorithm for the machine calculation of complex Fourier series," *Mathematics of Computation*, vol. 19, no. 90, pp. 297–301, April 1965.

[63] B. A. Olshausen and D. J. Field, "Emergence of simple-cell receptive field properties by learning a sparse code for natural images," *Nature*, vol. 381, no. 6583, pp. 607–609, June 1996.

[64] D. J. Graham and D. J. Field, "Natural images: Coding efficiency," *Encyclopedia of Neuroscience*, pp. 19–27, 2009.

[65] X. Hou and L. Zhang, "Saliency detection: A spectral residual approach," *Proceedings of the IEEE Conference on Computer Vision and Pattern Recognition*, pp. 1–8, June 2007, Minneapolis, MN, USA.

[66] C. A. Poynton, "Rehabilitation of gamma," *Proceedings of the SPIE Conference on Human Vision and Electronic Imaging III*, vol. 3299, pp. 232–249, January 1998, San Jose, CA, USA.

[67] S. S. Stevens, "On the psychophysical law," *Psychological Review*, vol. 64, no. 3, pp. 153–181, May 1957.

[68] R. J. Peters, A. Iyer, L. Itti, and C. Koch, "Components of bottom-up gaze allocation in natural images," *Vision Research*, vol. 45, no. 18, pp. 2397–2416, August 2005.

[69] S. Kullback, *Information Theory and Statistics.* New York, USA: Wiley, 1959.

[70] L. Itti and P. Baldi, "A principled approach to detecting surprising events in video," *Proceedings of the IEEE Conference on Computer Vision and Pattern Recognition*, vol. 1, pp. 631–637, June 2005, San Diego, CA, USA.

[71] T. Jost, N. Ouerhani, R. von Wartburg, R. Mri, and H. Hgli, "Assessing the contribution of color in visual attention," *Computer Vision and Image Understanding*, vol. 100, no. 1-2, pp. 107–123, Oct.-Nov. 2005.

[72] D. M. Green and J. A. Swets, *Signal Detection Theory and Psychophysics.* New York, USA: Wiley, 1966.

[73] B. W. Tatler, R. J. Baddeley, and I. D. Gilchrist, "Visual correlates of fixation selection: Effects of scale and time," *Vision Research*, vol. 45, no. 5, pp. 643–659, March 2005.

[74] F. Larsson, M. Felsberg, and P.-E. Forssén, “Correlating fourier descriptors of local patches for road sign recognition,” *IET Computer Vision*, vol. 5, no. 4, pp. 244–254, July 2011.

[75] T. Gevers and A. W. M. Smeulders, “Color-based object recognition,” *Pattern Recognition*, vol. 32, no. 3, pp. 453–464, March 1999.

[76] C. Grigorescu and N. Petkov, “Distance sets for shape filters and shape recognition,” *IEEE Transactions on Image Processing*, vol. 12, no. 10, pp. 1274–1286, October 2003.

[77] D. Gossow, J. Pellenz, and D. Paulus, “Danger sign detection using color histograms and SURF matching,” *Proceedings of the IEEE International Workshop on Safety, Security and Rescue Robotics*, pp. 13–18, October 2008, Sendai, Japan.

[78] A. Broggi, P. Cerri, P. Medici, P. Porta, and G. Ghisio, “Real time road signs recognition,” *Proceedings of the IEEE Intelligent Vehicles Symposium*, pp. 981–986, June 2007, Istambul, Turkey.

[79] K. L. Bouman, G. Abdollahian, M. Boutin, and E. J. Delp, “A low complexity sign detection and text localization method for mobile applications,” *IEEE Transactions on Multimedia*, vol. 13, no. 5, pp. 922–934, October 2011.

[80] L. Song and Z. Liu, “Color-based traffic sign detection,” *Proceedings of the International Conference on Quality, Reliability, Risk, Maintenance, and Safety Engineering*, pp. 353–357, June 2012, Chengdu, China.

[81] G. Loy and N. Barnes, “Fast shape-based road sign detection for a driver assistance system,” *Proceedings of the IEEE/RSJ International Conference on Intelligent Robots and Systems*, vol. 1, pp. 70–75, September 2004, Stockholm, Sweden.

[82] S. Maldonado-Bascon, S. Lafuente-Arroyo, P. Gil-Jimenez, H. Gomez-Moreno, and F. Lopez-Ferreras, “Road-sign detection and recognition based on support vector machines,” *IEEE Transactions on Intelligent Transportation Systems*, vol. 8, no. 2, pp. 264–278, June 2007.

[83] R. Malik, J. Khurshid, and S. N. Ahmad, “Road sign detection and recognition using colour segmentation, shape analysis and template matching,” *Proceedings of the International Conference on Machine Learning and Cybernetics*, vol. 6, pp. 3556–3560, August 2007, Hong Kong, China.

[84] J. Greenhalgh and M. Mirmehdi, “Real-time detection and recognition of road traffic signs,” *IEEE Transactions on Intelligent Transportation Systems*, vol. 13, no. 4, pp. 1498–1506, December 2012.

[85] W.-J. Won, M. Lee, and J.-W. Son, “Implementation of road traffic signs detection based on saliency map model,” *Proceedings of the IEEE Intelligent Vehicles Symposium*, pp. 542–547, June 2008, Eindhoven, Netherlands.

[86] R. Kastner, T. Michalke, T. Burbach, J. Fritsch, and C. Goerick, “Attention-based traffic sign recognition with an array of weak classifiers,” *Proceedings of the IEEE Intelligent Vehicles Symposium*, pp. 333–339, June 2010, San Diego, CA, USA.

[87] R. Belaroussi, P. Foucher, J.-P. Tarel, B. Soheilian, P. Charbonnier, and N. Paparoditis, "Road sign detection in images: A case study," *Proceedings of the International Conference on Pattern Recognition*, pp. 484–488, August 2010, Istambul, Turkey.

[88] D. C. W. Pao, H. F. Li, and R. Jayakumar, "Shapes recognition using the straight line Hough transform: Theory and generalization," *IEEE Transactions on Pattern Analysis and Machine Intelligence*, vol. 14, no. 11, pp. 1076–1089, November 1992.

[89] S. Houben, "A single target voting scheme for traffic sign detection," *Proceedings of the IEEE Intelligent Vehicles Symposium*, pp. 124–129, June 2011, Baden-Baden, Germany.

[90] H. Fleyeh and P. Zhao, "A contour-based separation of vertically attached traffic signs," *Proceedings of the Annual Conference of the IEEE Industrial Electronics Society*, pp. 1811–1816, November 2008, Orlando, FL, USA.

[91] L.-W. Tsai, J.-W. Hsieh, C.-H. Chuang, Y.-J. Tseng, K.-C. Fan, and C.-C. Lee, "Road sign detection using eigen colour," *IET Computer Vision*, vol. 2, no. 3, pp. 164–177, September 2008.

[92] G. Loy and A. Zelinsky, "Fast radial symmetry for detecting points of interest," *IEEE Transactions on Pattern Analysis and Machine Intelligence*, vol. 25, no. 8, pp. 959–973, August 2003.

[93] N. Barnes, A. Zelinsky, and L. Fletcher, "Real-time speed sign detection using the radial symmetry detector," *IEEE Transactions on Intelligent Transportation Systems*, vol. 9, no. 2, pp. 322–332, June 2008.

[94] P. Viola and M. J. Jones, "Robust real-time face detection," *International Journal of Computer Vision*, vol. 57, no. 2, pp. 137–154, May 2004.

[95] C. G. Keller, C. Sprunk, C. Bahlmann, J. Giebel, and G. Baratoff, "Real-time recognition of U.S. speed signs," *Proceedings of the IEEE Intelligent Vehicles Symposium*, pp. 518–523, June 2008, Eindhoven, Netherlands.

[96] X. Baro, S. Escalera, J. Vitria, O. Pujol, and P. Radeva, "Traffic sign recognition using evolutionary Adaboost detection and Forest-ECOC classification," *IEEE Transactions on Intelligent Transportation Systems*, vol. 10, no. 1, pp. 113–126, March 2009.

[97] A. R. Rostampour and P. R. Madhvapathy, "Shape recognition using simple measures of projections," *Proceedings of the Annual International Phoenix Conference on Computers and Communications*, pp. 474–479, March 1988, Scottsdale, AZ, USA.

[98] P. Gil-Jimenez, S. Lafuente-Arroyo, H. Gomez-Moreno, F. Lopez-Ferreras, and S. Maldonado-Bascon, "Traffic sign shape classification evaluation. Part II. FFT applied to the signature of blobs," *Proceedings of the IEEE Intelligent Vehicles Symposium*, pp. 607–612, June 2005, Las Vegas, NV, USA.

[99] A. W. Haddad, S. Huang, M. Boutin, and E. J. Delp, "Detection of symmetric shapes on a mobile device with applications to automatic sign interpretation," *Proceedings of the IS&T/SPIE Electronic Imaging - Multimedia on Mobile Devices*, no. 8304, pp. 1–8, January 2012, San Francisco, CA, USA.

[100] T. Pavlidis, “A review of algorithms for shape analysis,” *Computer Graphics and Image Processing*, vol. 7, no. 2, pp. 243–258, April 1978.

[101] ——, “Algorithms for shape analysis of contours and waveforms,” *IEEE Transactions on Pattern Analysis and Machine Intelligence*, vol. PAMI-2, no. 4, pp. 301–312, July 1980.

[102] S. Belongie, J. Malik, and J. Puzicha, “Shape matching and object recognition using shape contexts,” *IEEE Transactions on Pattern Analysis and Machine Intelligence*, vol. 24, no. 4, pp. 509–522, April 2002.

[103] O. R. Mitchell and T. A. Grogan, “Global and partial shape discrimination for computer vision,” *Optical Engineering*, vol. 23, no. 5, pp. 484–491, October 1984.

[104] C. T. Zahn and R. Z. Roskies, “Fourier descriptors for plane closed curves,” *IEEE Transactions on Computers*, vol. C-21, no. 3, pp. 269–281, March 1972.

[105] E. Persoon and K.-S. Fu, “Shape discrimination using Fourier descriptors,” *IEEE Transactions on Systems, Man and Cybernetics*, vol. SMC-7, no. 3, pp. 170–179, March 1977.

[106] D. Zhang and G. Lu, “Evaluation of MPEG-7 shape descriptors against other shape descriptors,” *Multimedia Systems*, vol. 9, no. 1, pp. 15–30, July 2003.

[107] R. Chellappa and R. Bagdazian, “Fourier coding of image boundaries,” *IEEE Transactions onPattern Analysis and Machine Intelligence*, vol. PAMI-6, no. 1, pp. 102–105, January 1984.

[108] C. Singh and P. Sharma, “Performance analysis of various local and global shape descriptors for image retrieval,” *Multimedia Systems*, vol. 19, no. 4, pp. 339–357, July 2013.

[109] I. Kunttu, L. Lepisto, J. Rauhamaa, and A. Visa, “Multiscale Fourier descriptor for shape-based image retrieval,” *Proceedings of the IEEE International Conference on Pattern Recognition*, vol. 2, pp. 765–768, August 2004, Cambridge, UK.

[110] M. N. Tahir, A. Hussain, and M. M. Mustafa, “Fourier descriptor for pedestrian shape recognition using support vector machine,” *Proceedings of the IEEE International Symposium on Signal Processing and Information Technology*, pp. 636–641, December 2007, Cairo, Egypt.

[111] J. Ma, Z. Zhang, H. Tang, and Q. Zhao, “Fast Fourier descriptor method of the shape feature in low resolution images,” *Proceedings of the IEEE International Conference on Wireless Communications Networking and Mobile Computing*, pp. 1–4, September 2010, Chengdu, China.

[112] J. Meyer, P. Schnitzspan, S. Kohlbrecher, K. Petersen, M. Andriluka, O. Schwahn, U. Klingauf, S. Roth, B. Schiele, and O. Stryk, “A semantic world model for urban search and rescue based on heterogeneous sensors,” *Proceedings of the Annual RoboCup International Symposium*, vol. 6556, pp. 180–193, June 2010, Singapore, Singapore.

[113] H. Bay, A. Ess, T. Tuytelaars, and L. V. Gool, "Speeded-up robust features (SURF)," *Journal of Computer Vision and Image Understanding*, vol. 110, no. 3, pp. 346–359, June 2008.

[114] N. Dalal and B. Triggs, "Histograms of oriented gradients for human detection," *Proceedings of the IEEE Conference on Computer Vision and Pattern Recognition*, vol. 1, pp. 886–893, June 2005, San Diego, CA, USA.

[115] S. Suzuki and K. Abe, "Topological structural analysis of digitized binary images by border following," *Computer Vision, Graphics, and Image Processing*, vol. 30, no. 1, pp. 32–46, April 1985.

[116] R. O. Duda and P. E. Hart, "Use of the Hough transformation to detect lines and curves in pictures," *Communications of the ACM*, vol. 15, no. 1, pp. 11–15, January 1972.

[117] J. Sklansky, "Finding the convex hull of a simple polygon," *Pattern Recognition Letters*, vol. 1, no. 2, pp. 79–83, December 1982.

[118] S. Pereira and T. Pun, "Robust template matching for affine resistant image watermarks," *IEEE Transactions on Image Processing*, vol. 9, no. 6, pp. 1123–1129, Jun. 2000.

[119] F. Essannouni and D. Aboutajdine, "Fast frequency template matching using higher order statistics," *IEEE Transactions on Image Processing*, vol. 19, no. 3, pp. 826–830, March 2010.

[120] I. Bartolini, P. Ciaccia, and M. Patella, "WARP: Accurate retrieval of shapes using phase of Fourier descriptors and time warping distance," *IEEE Transactions on Pattern Analysis and Machine Intelligence*, vol. 27, no. 1, pp. 142–147, January 2005.

[121] N. Otsu, "A threshold selection method from gray-level histograms," *IEEE Transactions on Systems, Man and Cybernetics*, vol. SMC-9, no. 1, pp. 62–66, January 1979.

[122] L.-S. Jin, L. Tian, R.-B. Wang, L. Guo, and J.-W. Chu, "An improved Otsu image segmentation algorithm for path mark detection under variable illumination," *Proceedings of the IEEE Intelligent Vehicles Symposium*, pp. 840–844, June 2005, Las Vegas, NV, USA.

[123] P. Soille, *Morphological Image Analysis: Principles and Applications.* New York/Heidelberg: Springer-Verlag, 2003.

[124] H. Park and R. Chin, "Decomposition of arbitrarily shaped morphological structuring elements," *IEEE Transactions on Pattern Analysis and Machine Intelligence*, vol. 17, no. 1, pp. 2–15, January 1995.

[125] R. C. Gonzalez, *Digital Image Processing.* New Jersey, USA: Prentice Hall, 2000.

[126] S. C. Park, M. K. Park, and M. G. Kang, "Super-resolution image reconstruction: A technical overview," *IEEE Signal Processing Magazine*, vol. 20, no. 3, pp. 21–36, May 2003.

[127] W.-C. Siu and K.-W. Hung, "Review of image interpolation and super-resolution," *Proceedings of the Asia-Pacific Signal Information Processing Association Annual Summit and Conference*, no. 6411957, pp. 1–10, December 2012, hollywood, CA, USA.

[128] Y. J. Liang, J. G. Apostolopoulos, and B. Girod, "Analysis of packet loss for compressed video: Effect of burst losses and correlation between error frames," *IEEE Transactions on Circuits and Systems for Video Technology*, vol. 18, no. 7, pp. 861–874, July 2008.

[129] Y. Wang and Q.-F. Zhu, "Error control and concealment for video communication: A review," *Proceedings of the IEEE*, vol. 86, no. 5, pp. 974–997, May 1998.

[130] S. Kumar, L. Xu, M. K. Mandal, and S. Panchanathan, "Error resiliency schemes in H.264/AVC standard," *Journal of Visual Communication and Image Representation*, vol. 17, no. 2, pp. 425–450, April 2006.

[131] S. Wenger, "H.264/AVC over IP," *IEEE Transactions on Circuits and Systems for Video Technology*, vol. 13, no. 7, pp. 645–656, July 2003.

[132] P. Lambert, W. D. Neve, Y. Dhondt, and R. V. de Walle, "Flexible macroblock ordering in H.264/AVC," *Journal of Visual Communication and Image Representation*, vol. 17, no. 2, pp. 358–375, April 2006.

[133] Y. Zhao, S. C. Ahalt, and J. Dong, "Optimal interleaving for 3-D zerotree wavelet video packets over burst lossy channels," *Proceedings of the IEEE International Conference on Acoustics, Speech, and Signal Processing*, vol. 2, pp. 333–336, March 2005.

[134] J. Rombaut, A. Pižurica, and W. Philips, "Optimization of packetization masks for image coding based on an objective cost function for desired packet spreading," *IEEE Transactions on Image Processing*, vol. 17, no. 10, pp. 1849–1863, October 2008.

[135] T. H. Vu and S. Aramvith, "An error resilience technique based on FMO and error propagation for H.264 video coding in error-prone channels," *Proceedings of the IEEE International Conference on Multimedia and Expo*, pp. 205–208, June 2009.

[136] K. Tan and A. Pearmain, "A new error resilience scheme based on FMO and error concealment in H.264/AVC," *Proceedings of the IEEE International Conference on Acoustics, Speech and Signal Processing*, pp. 1057–1060, May 2011.

[137] H. Hadizadeh and I. V. Bajić, "Burst-loss-resilient packetization of video," *IEEE Transactions on Image Processing*, vol. 20, no. 11, pp. 3195–3206, November 2011.

[138] C. Ying, J. Boyce, and X. Kai, "Frame loss error concealment for SVC," *JVT of ISO/IEC MPEG & ITU-T VCEG, Doc. JVT-Q046*, October 2005.

[139] Q. Peng, T. Yang, and C. Zhu, "Block-based temporal error concealment for video packet using motion vector extrapolation," *Proceedings of the IEEE International Conference on Communications, Circuits and Systems and West Sino Expositions*, vol. 1, pp. 10–14, June 2002.

[140] Y. Chen, K. Yu, J. Li, and S. Li, "An error concealment algorithm for entire frame loss in video transmission," *Proceedings of the IEEE Picture Coding Symposium*, pp. 1–4, December 2004.

[141] B. Yan and H. Gharavi, "Efficient error concealment for the whole-frame loss based on H.264/AVC," *Proceedings of the IEEE International Conference on Image Processing*, pp. 3064–3067, October 2008.

[142] Z. Wu and J. M. Boyce, "An error concealment scheme for entire frame losses based on H.264/AVC," *Proceedings of the IEEE International Symposium on Circuits and Systems*, pp. 4463–4466, May 2006.

[143] Y. Wang, J. Y. Tham, K. H. Goh, W. S. Lee, and W. Yang, "A distance-based slice interleaving scheme for robust video transmission over error-prone networks," *Proceedings of the IEEE International Conference on Acoustics, Speech and Signal Processing*, pp. 1509–1512, May 2011.

[144] B. E. Bayer, "An optimum method for two-level rendition of continuous-tone pictures," *Proceedings of the IEEE International Conference on Communications*, vol. 1, pp. 2611–2615, June 1973.

[145] Joint Video Team (JVT) of ISO/IEC MPEG & ITU-T VCEG, *SVC reference software JSVM 9.8*, available: http://ip.hhi.de/imagecom_G1/savce/downloads/SVC-Reference-Software.htm.

[146] V. Varsa, M. M. Hannuksela, A. Hourunranta, and Y.-K. Wang, "Non-normative error concealment algorithms," *ITU-T VCEG, Doc. VCEG-N62*, September 2001.

[147] E. N. Gilbert, "Capacity of a burst-noise channel," *Bell System Technical Journal*, vol. 39, pp. 1253–1266, September 1960.

[148] L. N. Kanal and A. R. K. Sastry, "Models for channels with memory and their applications to error control," *Proceedings of the IEEE*, vol. 66, no. 7, pp. 724–744, July 1978.

APPENDIX

A. MERGE IMAGE ACQUISITION PROTOCOL

This Appendix describes the protocol used for acquiring test images for the MERGE project. The images are used for testing various functions of the MERGE image analysis system.

- Persons involved
  - 1 MERGE staff member
- Equipment/Materials needed
  - Pens or pencils
  - 1 Mobile Telephone with Android OS
    - Built-in camera (1MPx and above)
    - 3G/4G/WiFi data connection
    - GPS
  - 1 Digital Camera with Android OS
    - 3G/4G/WiFi data connection
    - GPS
  - Image Recording Forms
  - External Hard Drive

1) Preliminaries (Internet connection required)
   a) Check Date and Time settings on the Android mobile telephone and the digital camera, and ensure date, time, and time zone are set to automatic (network-provided).
   b) Make sure the Android mobile telephone and the digital camera's batteries are fully charged.

   c) Make sure the GPS is enabled on the Android mobile telephone and the digital camera.

   d) Verify all equipments/materials above are available.

   e) Turn flash feature off on the Android mobile telephone and the digital camera.

   f) Note: The Image Taker will need to fill out an Image Recording Form for each hazmat sign.

2) Set up environment

   a) Stand in front of the hazmat sign, far enough so that the camera can capture all the content, up to 200 feet from the sign for the Android mobile phone, and up to 500 feet from the sign for the digital camera. Stand preferably perpendicular to the surface containing the sign. Limited angles are permitted (45 degrees), as shown in Figure A.1.

   b) Make sure weather conditions do not obstruct the view of the hazmat sign.

   c) Make sure there are no objects between the camera and the hazmat sign that partially or completely obstruct the view of the hazmat sign.

3) Taking Images of Hazmat Signs

   a) Launch the MERGE application on the Android mobile telephone and the digital camera, and login using the Image Taker's ID and password. If this is the first time that the Image Taker is logging into the application, an Internet connection will be required to connect with the MERGE database on the server. From then on, the Image Taker's credential will be stored on the Android device for future use without an Internet connection.

   b) Select the "Capture Image" option from the MERGE main screen. The camera activity is then initialized. Note that a new directory with the name MERGE will be created on the Android device's image gallery, where all the images taken using the MERGE application will be stored. Please refer to this directory when copying the images to the external hard drive (Section 5a).

c) Prepare for taking the image (position the camera as desired, within the recommended distance and angle from the hazmat sign). Make sure all the contents of the hazmat sign can be seen on the device screen.

d) Take an image of the hazmat sign, trying to hold the device as much as stable. The image can be retaken as many times as needed by tapping on the retake option on the camera activity.

e) Tap on the OK button on the camera activity to save the current image. The image will be automatically uploaded to the server and analyzed. The Image Taker should see a notification dialog with the text "Uploading image..." followed by another notification dialog with the text "Analyzing image...". If no Internet connection is available at the time, a warning dialog with the text "No Internet connection available" will be shown to the Image Taker. However, the image is stored in the Android device, and it can be uploaded and analyzed in the future using the "Browse Image" option from the MERGE main screen. If the image has not been uploaded to the server, check the box "Not Successfully Uploaded" on the Image Recording Form.

f) If no Internet connection is available at the time, a warning dialog with the text "No Internet connection available" will be shown to the Image Taker. In this case, the captured image is stored in the device, and it can be uploaded and analyzed in the future using the "Browse Image" option from the MERGE main screen.

g) Please take different images for the same sign, at different distances (10-150 ft) and angles of view (0-45°), and then write down an Image ID shown on the top bar / pop-up window on the result screen, an approximate Angle of View between your viewpoint and the perpendicular plane of the hazmat sign's surface, and an approximate Distance from your viewpoint to the hazmat sign on the Image Recording Form (e.g., 123456, 15°, and 125 ft).

h) Please take at least one image with No Zoom when using the digital camera, and then check the box “No Zoom” on the Image Recording Form. Also take some images using the Optical Zoom when using the digital camera (NO Digital Zoom), and then check the box “Zoom” and mark on an approximate Zoom Value in a box on the Image Recording Form (e.g., 3/4 of the entire optical zoom range).

4) Completing the Image Recording Form (Figure A.2)

   a) Record Date (MM/DD/YYYY), Starting Time (HH:MM:SS), the Make and Model of the device used to capture the images (e.g., HTC Desire) and the Image Taker’s Name and Affiliation on the Image Recording Form.

   b) Complete the “Ground Truth Information” section on the Image Recording Form with ground-truth information associated with each hazmat sign in the captured image. This includes:

      - The Total number of existing hazmat signs in the captured image
      - For each existing hazmat sign
        - Hazmat sign number of an existing hazmat sign in the captured image
        - Color(s): color(s) found in the hazmat sign (NOT including hazmat sign frame)
        - UN Identification number (UNID) (Figure A.3(a))
        - Symbol (Figure A.3(b))
        - Class (Figure A.3(c))
        - Text (Figure A.3(d))
        - Comments: Additional information of the hazmat sign that does not fit in the previous fields.

   c) Complete the “Image Analysis Results” section on the Image Recording Form with information retrieved from the server after a captured or browsed image has been analyzed. This includes:

      - The Image ID of the captured image

- The Total number of highlighted hazmat signs from image analysis
- For each returned hazmat sign
  - Hazmat sign number of a highlighted hazmat sign shown in the result screen
  - Color(s): color(s) shown in the result screen
  - Text: text shown in the result screen
  - No hazmat signs found: Check this box if a dialog containing “No hazmat signs found” is shown to the Image Taker after uploading an image to the server, meaning that no hazmat signs have been found in the current image.

There are two cases of image analysis results, hazmat sign found (left) and not found (right), shown in Figure A.4. Figures A.5 and A.6 show two examples of completed Image Recording Forms for the two different cases.

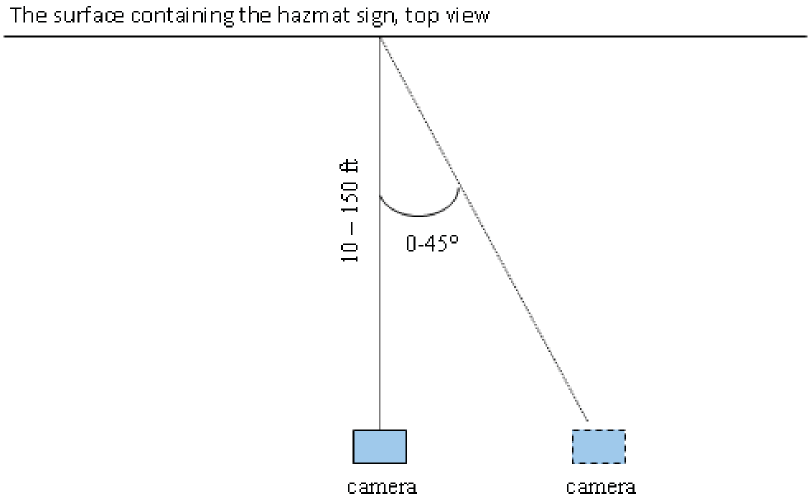

Fig. A.1. Top view of the setup environment.

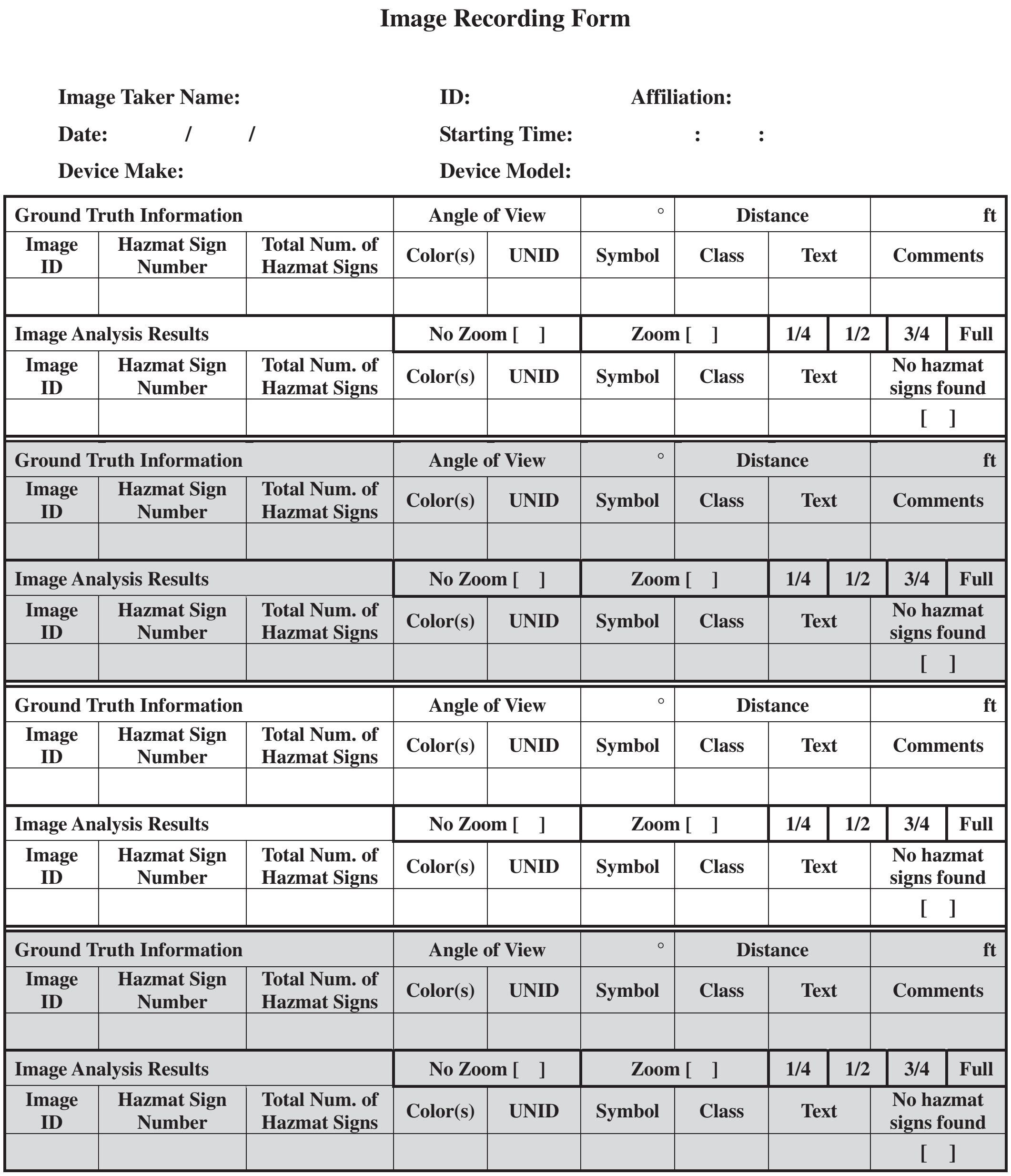

Image Recording Form

Image Taker Name: **ID:** **Affiliation:**

Date: / / **Starting Time: : :**

Device Make: **Device Model:**

Ground Truth Information			**Angle of View**		°	**Distance**			ft	
Image ID	**Hazmat Sign Number**	**Total Num. of Hazmat Signs**	**Color(s)**	**UNID**	**Symbol**	**Class**	**Text**		**Comments**	
Image Analysis Results			**No Zoom [ ]**		**Zoom [ ]**		**1/4**	**1/2**	**3/4**	**Full**
Image ID	**Hazmat Sign Number**	**Total Num. of Hazmat Signs**	**Color(s)**	**UNID**	**Symbol**	**Class**	**Text**		**No hazmat signs found**	
									[ ]	
Ground Truth Information			**Angle of View**		°	**Distance**			ft	
Image ID	**Hazmat Sign Number**	**Total Num. of Hazmat Signs**	**Color(s)**	**UNID**	**Symbol**	**Class**	**Text**		**Comments**	
Image Analysis Results			**No Zoom [ ]**		**Zoom [ ]**		**1/4**	**1/2**	**3/4**	**Full**
Image ID	**Hazmat Sign Number**	**Total Num. of Hazmat Signs**	**Color(s)**	**UNID**	**Symbol**	**Class**	**Text**		**No hazmat signs found**	
									[ ]	
Ground Truth Information			**Angle of View**		°	**Distance**			ft	
Image ID	**Hazmat Sign Number**	**Total Num. of Hazmat Signs**	**Color(s)**	**UNID**	**Symbol**	**Class**	**Text**		**Comments**	
Image Analysis Results			**No Zoom [ ]**		**Zoom [ ]**		**1/4**	**1/2**	**3/4**	**Full**
Image ID	**Hazmat Sign Number**	**Total Num. of Hazmat Signs**	**Color(s)**	**UNID**	**Symbol**	**Class**	**Text**		**No hazmat signs found**	
									[ ]	
Ground Truth Information			**Angle of View**		°	**Distance**			ft	
Image ID	**Hazmat Sign Number**	**Total Num. of Hazmat Signs**	**Color(s)**	**UNID**	**Symbol**	**Class**	**Text**		**Comments**	
Image Analysis Results			**No Zoom [ ]**		**Zoom [ ]**		**1/4**	**1/2**	**3/4**	**Full**
Image ID	**Hazmat Sign Number**	**Total Num. of Hazmat Signs**	**Color(s)**	**UNID**	**Symbol**	**Class**	**Text**		**No hazmat signs found**	
									[ ]	

Fig. A.2. Image recording form for the MERGE project.

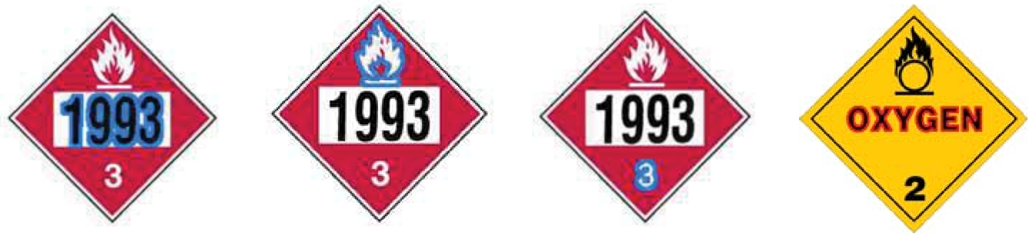

(a) UNID (b) Symbol (c) Class (d) Text

Fig. A.3. Hazmat sign identifiers.

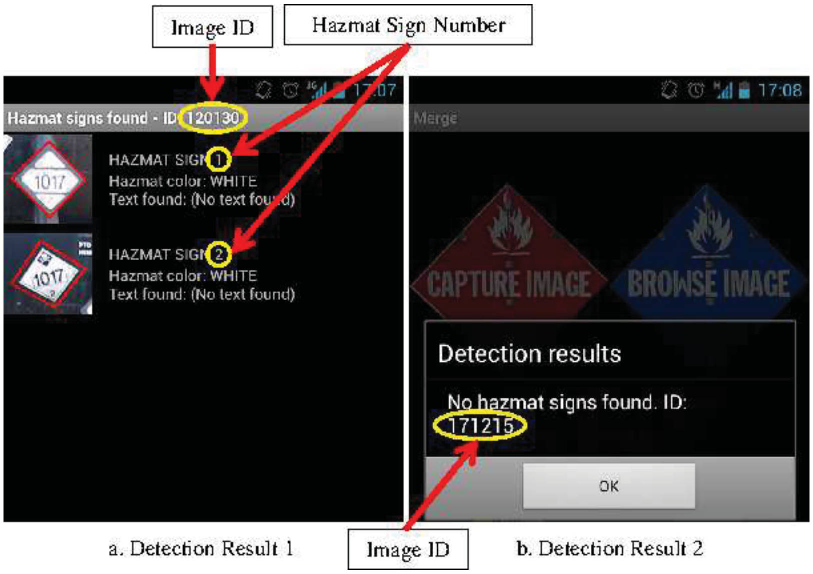

Hazmat signs found - ID 120130

HAZMAT SIGN 1
Hazmat color: WHITE
Text found: (No text found)

HAZMAT SIGN 2
Hazmat color: WHITE
Text found: (No text found)

Detection results

No hazmat signs found. ID: 171215

Fig. A.4. Examples and screenshots of the two cases of image analysis results, hazmat sign found (left) and not found (right).

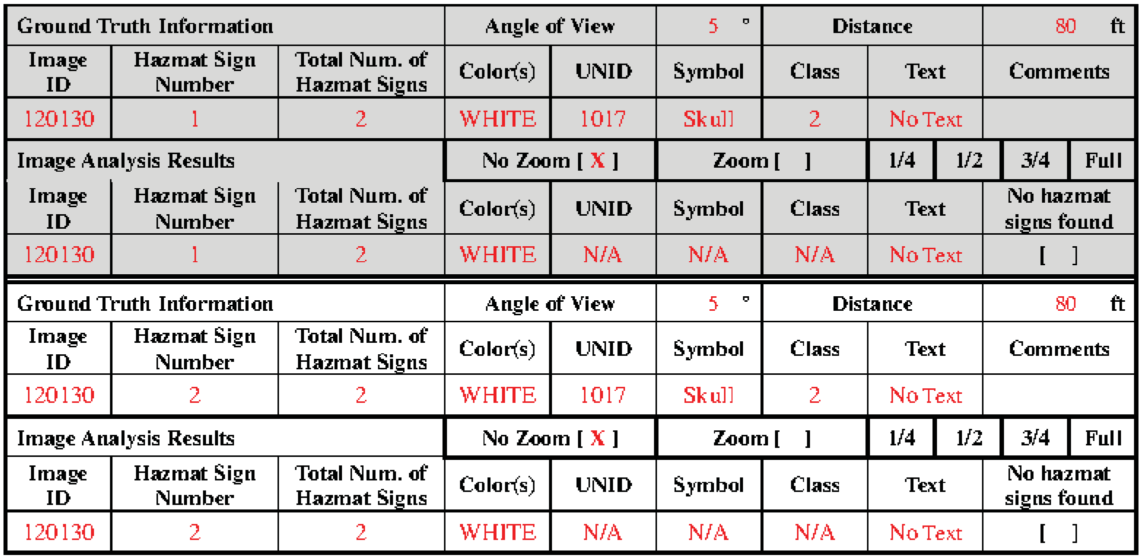

Ground Truth Information			Angle of View		5 °	Distance			80 ft	
Image ID	Hazmat Sign Number	Total Num. of Hazmat Signs	Color(s)	UNID	Symbol	Class	Text		Comments	
120130	1	2	WHITE	1017	Skull	2	No Text			
Image Analysis Results			No Zoom [X]		Zoom [ ]		1/4	1/2	3/4	Full
Image ID	Hazmat Sign Number	Total Num. of Hazmat Signs	Color(s)	UNID	Symbol	Class	Text		No hazmat signs found	
120130	1	2	WHITE	N/A	N/A	N/A	No Text		[ ]	
Ground Truth Information			Angle of View		5 °	Distance			80 ft	
Image ID	Hazmat Sign Number	Total Num. of Hazmat Signs	Color(s)	UNID	Symbol	Class	Text		Comments	
120130	2	2	WHITE	1017	Skull	2	No Text			
Image Analysis Results			No Zoom [X]		Zoom [ ]		1/4	1/2	3/4	Full
Image ID	Hazmat Sign Number	Total Num. of Hazmat Signs	Color(s)	UNID	Symbol	Class	Text		No hazmat signs found	
120130	2	2	WHITE	N/A	N/A	N/A	No Text		[ ]	

Fig. A.5. Examples of completed image recording form for hazmat sign found in Figure A.4 (left).

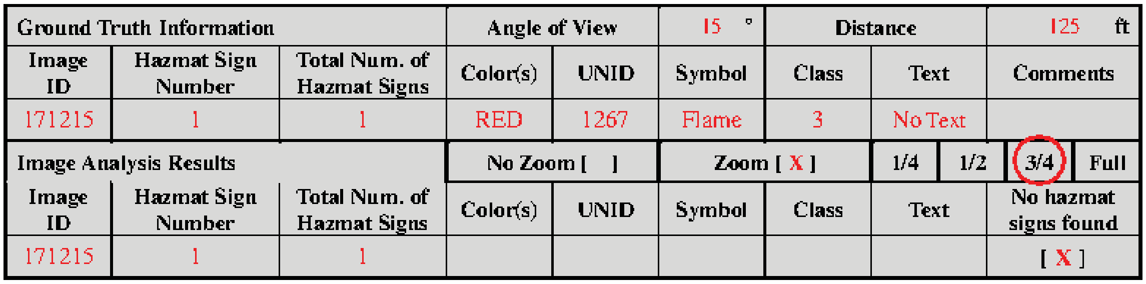

Ground Truth Information			Angle of View		15 °	Distance			125 ft	
Image ID	Hazmat Sign Number	Total Num. of Hazmat Signs	Color(s)	UNID	Symbol	Class	Text		Comments	
171215	1	1	RED	1267	Flame	3	No Text			
Image Analysis Results			No Zoom [ ]		Zoom [X]		1/4	1/2	[✓ 3/4]	Full
Image ID	Hazmat Sign Number	Total Num. of Hazmat Signs	Color(s)	UNID	Symbol	Class	Text		No hazmat signs found	
171215	1	1							[X]	

Fig. A.6. Examples of completed image recording form for hazmat sign not found in Figure A.4 (right).

VITA

VITA

Bin Zhao obtained the B.S. degree in Telecommunication Engineering and the M.S. degree in Information and Telecommunication Engineering (both with Highest Distinction) from Xidian University, Xi'an, China. He was a Graduate Fellow and Research Assistant of the National Key Laboratory of Integrated Service Networks (ISN), Xi'an, China. He is pursuing the Ph.D. degree in Electrical and Computer Engineering in Purdue University, West Lafayette, Indiana, USA. He was working as a Graduate Teaching Assistant in the School of Electrical and Computer Engineering in Purdue University from 2009 to 2010. He is working as a Graduate Research Assistant in the Video and Image Processing Laboratory (VIPER) under the supervision of Professor Edward J. Delp since 2010. He is a student member of the IEEE, the IEEE Communications Society, and the IEEE Signal Processing Society. His research interests include image analysis, image and video processing, computer vision, object recognition, and machine learning.